Modeling of flow and sediment transport in the vicinity of immersed structures : application to aquaculture cages

Thi Hai Yen Nguyen

Normandie Université

THESE

Pour obtenir le diplôme de doctorat

Spécialité : mécanique des fluides, énergétique, thermique, combustion, acoustique

Préparée au sein de l'Université de Caen Normandie

Modélisation des écoulements et du transport de sédiments au voisinage de structures immergées : application aux cages d'aquaculture.

Présentée et soutenue par

Thi Hai Yen NGUYEN

Thèse soutenue publiquement le 31 janvier 2018 devant le jury composé de		
M. Fabien CANDELIER	Maître de Conférences, HDR, Aix-Marseille Université	Rapporteur
M. Franck NICOLLEAU	Senior lecturer, HDR, Dept of Mechanical Engineering, University of Sheffield (G.B.)	Rapporteur
M. Philippe SERGENT	Directeur de Recherche, CEREMA Compiègne	Examinateur
M. Adil RIDHA	Maître de Conférences, HDR, Université de Caen Normandie	Examinateur
M. Yann MEAR	Professeur des Universités Intechmer/LUSAC, CNAM, Tourlaville	Codirecteur de thèse
M. Jean-Régis ANGILELLA	Professeur des Universités Université de Caen Normandie	Directeur de thèse

Thèse dirigée par Jean-Régis ANGILELLA (Université de Caen Normandie)
et Yann MEAR (CNAM/Intechmer/LUSAC).

UNIVERSITÉ CAEN NORMANDIE

ED PSIME

LUSAC

Modélisation des écoulements et du transport de sédiments au voisinage de structures immergées : application aux cages d'aquaculture.

Mémoire de thèse rédigé par :

Thi Hai Yen NGUYEN, doctorante au LUSAC, Université de Caen.

Recherches menées sous la direction de

Jean-Régis Angilella (Université de Caen Normandie)

Yann Méar (CNAM/Intechmer/LUSAC),

Emmanuel Poizot (CNAM/Intechmer/LUSAC).

Ecole Doctorale PSIME, Université de Caen

Novembre 2017

Acknowledgement

This work could not have been accomplished without the help of people I was in contact with from the beginning until now. The following lines are dedicated to them, I hope no one is left unmentioned.

Firstly, I would like to express my sincere gratitude to my advisor Jean-Régis Angilella who offered me a chance to be his student, to work with him during the time in Cherbourg. To be honest, before coming to France, I was not familiar with Fluid Mechanics. If it was not him to tell me 'you are here to learn, you can do it' , I would have quitted. I do appreciate his patience, his guidance and continuous support. I've learned a lot from him, not only from his fruitful knowledge in common and specific, but also his behaviour of a gentleman. My appreciation also goes to Yann Méar and the warmth of his fatherhood's hand embracing mine when I was in the hospital for an unwanted accident. His and Emmanuel Poizot's supports and wise advices helped me a lot in completing the thesis. I wish to meet him soon, then he could give me his motorbike after leaving my country then. Sylvain Guillou was the first person to welcome me with the typical hug and kiss of the French people. I thank him and his adorable wife and daughter for the happy times we shared. Thanks to Alina, I am really happy to be invited to have lunch and dinner at her home. I've undergone unforgettable times of my life here in France with my colleagues: Van Thinh, Jérome, Christine, Cristina, Paul, Guillaume, Mikaël, Philippe... Thanks to them, break times have always been fulfilled with joy and laughters. Thanks to them, I know how to swim, to dance and even to swear in French.

Although they are far from me and what I've been doing here, I would like to thank some of my friends: my hilarious friends who never got tired of texting me and encouraging me whenever my mood went down ; my Vietnamese friends living and studying in France who were always present in time of need.

I would like to send my appreciation to the Vietnamese Ministry of Education and Training, and to my University in Vietnam for funding.

Last but not least, I would like to thank my family and my special friend for their warmth and for their spiritual support throughout my thesis and my life.

Résumé

Les travaux présentés dans ce manuscrit portent sur les courants et le transport de matière solide en suspension, au voisinage de grandes structures immergées en eau peu profonde. Nous avons focalisé notre étude sur le cas de cages d'aquaculture installées dans la rade de Cherbourg. Situées dans une zone de fort courant, elles impactent leur environnement en modifiant l'écoulement et la turbidité locale. En dépit de nombreuses études déjà disponibles sur l'impact hydrodynamique de tels obstacles, de nombreuses questions se posent encore concernant l'écoulement sous la cage, la production de turbulence, l'érosion du sol et la remise en suspension de sédiments, ainsi que le devenir des déchets produits par la cage. Nous avons choisi de développer trois approches complémentaires pour apporter des éléments de réponse à ces questions. La thèse débute par une étude purement théorique de l'hydrodynamique au voisinage d'un obstacle immergé, assimilé à un milieu poreux, et dans une géométrie simplifiée. Ce modèle bi-dimensionnel, dans le plan vertical, donne de premiers ordres de grandeurs concernant la chute de pression motrice le long du courant, l'accélération du fluide sous la cage, la production de turbulence. Cette étude est suivie d'une analyse numérique de ce même modèle, dans laquelle certaines approximations seront levées. En particulier, le modèle numérique permet de considérer des cages plus imperméables que celles analysées par le modèle théorique. Il est cependant limité en nombre de Reynolds, et a été appliqué avec des échelles réduites. Ce modèle numérique a permis d'analyser le lien direct entre le coefficient de traînée effectif de la cage et diverses quantités-clés : le débit à travers la cage, la chute de pression le long du courant, la production de turbulence et l'apparition d'une zone de recirculation à l'arrière de l'obstacle. Ce dernier effet, visible seulement pour des cages très imperméables, a un impact notable sur le transport de sédiments et d'effluents : lorsque l'arrière de la cage devient une zone morte (zone de recirculation), l'essentiel du débit passe au dessous, ce qui crée de fortes survitesses et produit de la turbulence. Celle-ci peut alors entraîner des particules indésirables dans la zone morte, ce qui augmente notablement la complexité de leurs trajectoires et retarde leur évacuation. Enfin, ces études théoriques ont été complétées par des mesures vélocimétriques et turbidimétriques à l'amont et à l'aval d'une grande cage installée dans la rade de Cherbourg. Celles-ci confirment la présence d'une survitesse en provenance du dessous de la cage, comparable à celle prédite par le modèle théorique. Dans le cas d'une cage très peu perméable, la persistence d'une forte turbidité a été mesurée à l'aval de celle-ci, en accord qualitatif avec les simulations numériques.

Abstract

This manuscript presents investigations of current and sediment transport in the vicinity of large immersed structures in shallow water flows. It focuses on aquaculture cages installed in the roadstead of Cherbourg. Being located in a high stream zone, these obstacles have a non-negligible effect on currents as well as turbidity. In spite of numerous references on this topic, many questions still arise concerning the environmental impact of such objects. Quantitative information are still needed about the flow below the cage, turbulence production, erosion of the sand bed, sediments resuspension, and evacuation of effluents. To deal with these open questions, we have chosen to develop three complementary approaches. The thesis starts with an analytical study of the flow in a simplified two-dimensional model containing a large rectangular porous structure. Only the motion in the vertical mid-plane of the obstacle is considered. This preliminary model provides estimations of various dynamic quantities, like the velocity increase below the cage, the decay of piezometric pressure along the stream, and turbulence production. Then follows a numerical analysis of the very same flow, based on less stringent approximations. Because of the high cost of computations, simulations have been done at a reduced scale. Nevertheless, they confirm most of the findings of the analytical approach for very permeable cages, and provide crucial information also about weakly permeable cages which were out of reach of the analytical model. In particular, the formation of a recirculation cell behind such cages, together with turbulence production, have been studied with the numerical model. This effect has been observed to affect sediment and effluent transport: when the flow at the rear of the cage takes the form of a cell with closed streamlines, the cage can be thought of as closed and most of the flow passes below. This creates large velocity gradients and produces turbulence which significantly increases the dispersion of sediments and effluents. These particles are then likely to be captured for some time in the cell, instead of being evacuated away. In addition to these theoretical approaches, in-situ current and turbidity measurements have been performed upstream and downstream of a large cage immersed in the roadstead of Cherbourg. They confirm the existence of a fast stream emerging from below the cage. Vertical streamwise velocity profiles have been shown to agree with theoretical ones, in the case of a very permeable cage. Also, large turbidity levels have been recorded at the rear of a weakly permeable cage, in qualitative agreement with simulations.

Communication portant sur une partie de ces travaux de thèse :

E. Poizot, R. Verjus, H. Y. N'Guyen, J. R. Angilella, Y. Méar. Self-contamination of aquaculture cages in shallow water. *Environmental Fluid Mechanics 16 (4), 793-805, 2016.*

Contents

List of symbols

Re	Reynolds number
x_a	x-coordinate of the upstream border of the cage (m)
x_b	x-coordinate of the downstream border of the cage (m)
l_x	length of the cage, $l_x = x_b - x_a$
x_t	x-coordinate of the origin of the turbulent zone
l_y	depth of the cage (m)
L_y	depth of the water column (m)
U_∞	upstream velocity $(m.s^{-1})$
ν	kinematic viscosity of sea water $(m^2.s^{-1})$
μ	dynamic viscosity of sea water $(Pa.s)$
ρ	fluid density $(kg.m^{-3})$
τ^t	turbulent stress tensor (Pa)
τ^t_{ij}	components of turbulent stress tensor (Pa)
C_D	individual drag coefficient of each elementary object within the cage
C_{net}	effective drag coefficient of the cage
C_X	total drag coefficient of the cage
F_X^{cage}	total drag exerted on the cage (N)
S	total cage surface (m^2)
A	apparent surface of the cage (m^2)
E_s	solidity of the net
$\delta(x)$	thickness of the mixing layer (m)
Δ	typical value of $\delta(x)$
N	total number of elementary obstacles within the cage
β	proportion of obstacles
u, v	instantaneous velocity in alphabetical notation
u', v'	fluctuating velocity in alphabetical notation
$\bar{u}$, $\bar{v}$	mean velocity in alphabetical notation

v_i	instantaneous velocity in index notation
v_i'	fluctuating velocity in index notation
V_i	mean velocity in index notation
$\vec{V}$	mean velocity in vector notation
$\bar{u}_n$	horizontal mean velocity of the stream inside the cage ($m.s^{-1}$)
$\bar{u}_s$	horizontal mean velocity of the stream below the cage ($m.s^{-1}$)
u_0	equal to $\bar{u}_n(x_b)$
u_1	equal to $\bar{u}_s(x_b)$
α	pressure drop ($Pa.m^{-1}$)
σ	spread rate of the mixing layer, dimensionless
κ	non-dimension constant
q_{uu}	non-dimensional constant
$I(x,y)$	turbulent intensity
$I_0(x)$	turbulent intensity along the axis of the mixing layer $y = a$
ν_T	turbulent viscosity ($m^2.s^{-1}$)
k	turbulent kinetic energy ($J.kg^{-1}$)
ε	viscous dissipation rate of k ($W.kg^{-1}$)
C_μ	non-dimensional constant ≈ 0.09
ω	specific dissipation rate (s^{-1})
$\alpha*$	non-dimensional constant
y^+	dimensionless wall distance
$\hat{P}$	piezometric pressure
τ_w	wall shear stress
$\mathcal{L}$	cell extent
Q_{net}	flow rate per unit width through the net
Q_{total}	total flow rate
f_s	ADCP's transmitting sound frequency in water (kHz)
f_D	recorded frequency of reflected wave (kHz)
θ	angle between ACDP's beam and the velocity of the scatterer
r_p	radius of simulated particles (m)
ρ_p	density of particles ($kg.m^{-3}$)
$\vec{V_p}$	particle velocity
$\vec{x_p}$	particle position
m_p	particle mass (kg)
m_f	mass of fluid displaced by particle (kg)

Re_p	particle Reynolds number
S_p	apparent surface of particle (m^2)
τ_e	eddy life time (s)
T_L	Lagrangian time scale (s)
C_L	non-dimensional constant, $C_L \approx 0.15$
τ_p	particle response time (s)
T	time lapse used in eddy lifetime model (s)
t_{cross}	time required for a particle to cross a vortex (s)
St	Stokes number
$L_p(t)$	particle path length (m)

Chapter 1

Introduction

This part of the thesis proposes general information about aquaculture activities in coastal flows. The environmental impact of these activities is discussed, and information are given about the hydrodynamics of fish cages in strong flows. The objectives of the thesis are then presented.

1.1 Context and general considerations

Nowadays, more and more industrial activities take place in coastal areas to take advantage of coastal flow potentials. Therefore, the so called *anthropic pressure* is expected to grow in the next decades. To quote but a few examples, the environmental impact of shorelines, marine works, harbor traffic, marine energy facilities, and food industry is clearly unavoidable.

Aquaculture also has an impact on environment, and is in return very sensitive to environmental conditions (see for example Holmer & Kristensen (1994) [48] ; Doglioli et al. (2004) [25] ; Naylor et al. (2005) [64]). As a matter of fact, fish cages are strongly affected by the quality of water, the concentration and type of suspended sediments, and the intensity of flows. They are generally installed in zones where streams naturally bring clean water and drive effluents away. These effluents (faeces, uneaten food, etc.) are produced in very large amounts and can also affect the environment. The transport of these materials must then be controlled not only to avoid pollution downstream of the cages, but also for the cages themselves. Indeed, in most situations the plume of effluents has a complex evolution which is difficult to predict, as it depends on the flow conditions (slow, fast ; laminar, turbulent), the strength of winds, the quality of the cage

(clean and permeable, dirty and impermeable), and many other factors. An important effort must then be made to enhance our understanding of these complex effects. For this reason, in addition to the classical experimental approaches (turbidity and flow measurements, biological analyses, etc.), some numerical techniques have been developed in the past decades to allow an accurate prediction of the transport processes near aquaculture facilities.

Most of the classical approaches to model coastal flows are based on the two-dimensional Saint-Venant equations in the horizontal plane, which provide the fluid velocity averaged over the water column. This approach is also used in the context of aquacultural activities (see for example Venayagamoorthy (2011) [81]). Though this method predicts efficiently the large scale flow/structure interaction, with a relatively low computational cost, it does not provide any information about the vertical motion of water, the short-time unsteadiness, and the vertical mixing of sediments[1]. These mechanisms however, are of fundamental importance to understand and predict efficiently the effect of the flow on any immersed structure, and the effect of the structure on flow and sediment transport.

The goal of this thesis is precisely to model these interactions in details* in the vertical plane*, and to compare results, at least qualitatively, to in-situ measurements performed along the water column in the set of cages installed in Cherbourg's roadstead.

1.2 Hydrodynamic models for aquaculture facilities in natural streams

Even though near-shore aquaculture has expanded worldwide in the last decades, the development of methods to understand hydrologic conditions within net cages enclosed in fish farms near-shore has been limited. This is mainly due to a lack of field data, and to the complexity and number of relevant hydrologic processes: tidal and wind forcing, evapotranspiration, overland flow through emergent vegetation, salinity-induced density-dependent flow, and surface-water/ground-water interactions [54]. In recent years, extensive investigations have been carried out with an ambition to gain wider knowledge about the hydrodynamic fields of net cages. A

[1] More information about the modelling of sediment transport can be found in Refs. [3][6][4][9][8].

series of tests have been carried out by Aarsnes et al. (1990) [1] to study the velocity distribution within net cage systems. Many other scientists also concentrated on physical model tests and field measurement. The nets being flexible structures (Tsukrov et al. [80]), numerical studies on flow field around net cages are rather complex due to the fluid/structure interaction. However, significant advances could be made possible by treating a net cage as a porous medium (Cheng et al. (2004) [22], Partusson et al. (2010) [65], Zhao et al. (2011) [87], Chun-Wei Bi et al. (2013) [11]). This approach will be used in the present thesis also.

Characteristics of the flow field inside and around fishnet-cages can be described through a combination of theories, CFD[2] models and measurements. Typically, a fish-net cage is composed of knots and twines and the total amount of twines in a trawl can reach values of the order of 10^6. It is therefore impractical and computationally expensive to model every single twine. Moreover, when being immersed for a long period of time in water, cages undergo bio-fouling and contamination processes which may decrease their permeability. This means that the ability of cages to restrict the flow passing through them varies with time and, as a consequence, the problem becomes more and more complicated. This is the reason why many authors suggest to model net cages as porous media. Many 2D studies using this technique were reported in the publication of Patursson et al. (2010) [65] while Vincent and Marichal (1996) [84] used a similar but different description of the flow through the net for modelling asymmetric net structures. Helsley and Kim (2005) [45] also used CFD for investigating mixing behind an aquaculture cage. Other approaches including analytical models have also been used (e.g. Loland (1991 and 1993) [59] [60] ; Li et al. (2006) [58]).

However, even if the porous medium analogy is an important simplification, finding the best porous media coefficients for the specific net under study is a difficult task (Bi et al. (2014 and 2015) [11] [12]). In the present thesis, the hydrodynamic performance of the cage will be characterized by an effective drag coefficient C_{net}, that will be defined in Chapter 2, and which will represent the additional drag due to the presence of many obstacles inside the net.

[2]CFD: computational fluid dynamics.

1.3 Hydrodynamic performances of empty nets

To quantify the interaction between aquaculture cages and the surrounding flow, one has to study the hydrodynamic performance of nets, and to determine the corresponding drag coefficient. Key physical factors to be considered are the water depth, current velocity, near field circulation and the solidity of the net. The latter is defined as [54]:

$$\text{solidity} = \frac{\text{projected area of the net}}{\text{total area enclosed by the net}},$$

and has various expressions depending on the geometry of the fish net. This quantity arises as soon as one consider the drag and lift due to the twines forming the net.

In the 1990's, Aarsens et al. [2] firstly classified the external forces acting on a supple net cage into drag force and lift force and laid a foundation for further studies of dynamic characteristics of net cages. Loland (1991) [59] developed a model to calculate drag and lift forces and investigate wake effects behind net structures. However, results gained from these models were not accurate enough to evaluate the flow field around and inside net cages. Fredheim and Faltinsen (2003) [29] and Fredheim (2005) [28] presented numerical models to calculate the flow field in front of and inside a three-dimensional porous structure. These models are not practical for the analysis of large and integrated net cage arrays but they agree with experimental studies carried out by Gansel et al.[36], [34], [33] and Harendza et al. (2008)[44], which illustrated the complexity of the flow around porous cylinders within a solidity range from 1 (solid) to 0.1.

Hydrodynamic performance of nets is often characterized in terms of the solidity ratio defined above (Aarsnes et al. (1990); Balash et al. (2009) [7]; Lader and Enerhaug (2005) [57]; Zhan et al. (2006) [86], Klebert et al. (2013) [54]), which depends on the net geometry and on the nature of materials used to construct the net. The netting of a fish cage drowned in a coastal flow is subjected to changes in geometry and porosity. Deformation induced by external forces and changes in porosity due to bio-fouling and contamination may lead to a considerable variation of drag force acting on the net frame, as shown in Fig. 1.2 by Fridman (1986) [32](see also Braithwaite et al. (2007) [13], Firtridge et al. [27]). Generally, a decrease in the porosity of fish cages leads to a greater water blockage, to an increase in the flow speed at the flanks of the cages and to a stronger velocity reduction in their wakes (Gansel et al. (2008) [33], see also Refs. [34][35][36]). Gansel's studies furthermore confirm that the separation point of the wake shifts downstream with the increasing of porosity. They proposed three valuable regimes of the

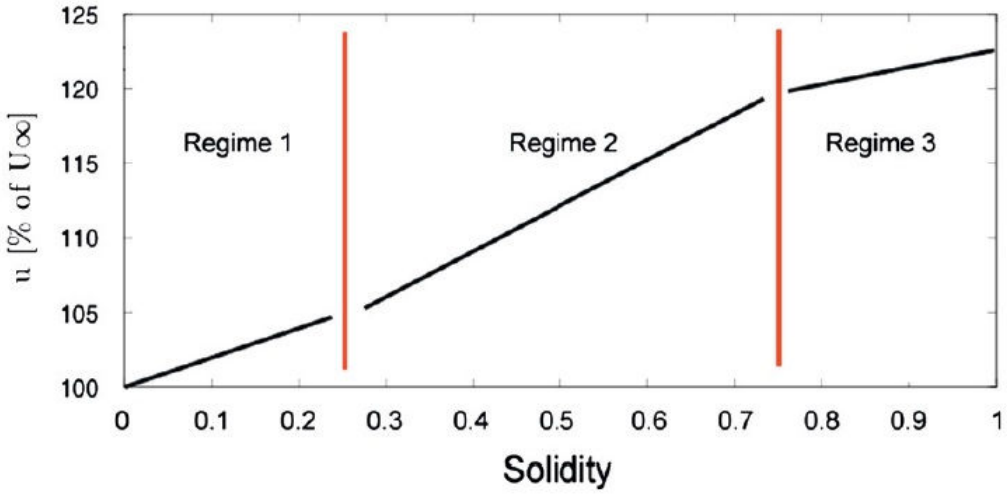

Figure 1.1: *Flow blockage and regimes of the flow through fish cage netting with different values of solidity, Gansel et al (2010)[34]. The flow speed (u) at the flanks of the fish cage, is given as a percentage of the ambient flow speed, U_∞.*

flow around and through porous cylinders as indicated in Fig. 1.1. Each regime corresponds to a certain range of the net cage solidity.

Moe et al. (2010) [43] showed that a cage with a netting solidity of 0.23, in currents from 0.1 to 0.5 $m.s^{-1}$ experienced relatively large deformations (volume reduction up to 70 %). Aarsnes et al. (1990) [2][1] observed that 80% of the expected volume available to hold fish in gravity cage may be lost in a current of $1\,m.s^{-1}$, and the velocity reduction from cage to cage was estimated to be 20% (19,7 % solidity), 30% (40.8 % solidity) and 58% (58.8 % solidity) – Fredricksson [31].

Types of netting and biofouling. In the aquaculture industry, four types of copper netting are mainly used. Expanded copper–nickel (Fig. 1.3a) was originally employed in inshore fish farms in the 1970's (Ansuini and Huguenin, 1978 [51], Huguenin, (1978) [50]; Powell, (1976) [71]). It is made of 90% copper and 10% nickel and is available in a wide range of openings and gauges (NAAMM EMMA 557, 1999; WHEA, 1984). The chain-link woven brass (Fig. 1.3b) is a composition of 65% copper and 35% zinc. Being used inshore since the 1990's, it has been recently adapted for offshore farming (Celikkol et al., (2010) [19]; DeCew et al., (2010) [24]). New material designs include welded silicon–bronze (Fig. 1.3c) and woven silicon–bronze composed of 97% copper with 3% silicon. Researches recently indicated that material and color

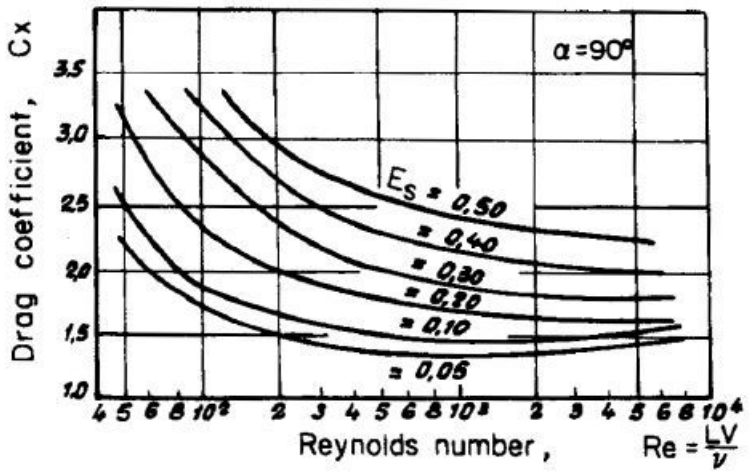

Figure 1.2: *Drag coefficient of an empty net versus the flow Reynolds number, for various net solidities (from Fridman [32]).*

also affect salmon-cage biofouling. Copper treatment, as shown in some studies, reduced fouling and caused a reduction in twine diameter. However, the coating roughness caused a significant increase in the drag coefficient. Results from many other researches also indicate that drag of biofouled nets may be over three times bigger than that of clean nets (see for example Swift (2006) [78]).

Net cages and wave loading. Net cages in open sea will experience more severe wave loading than those used in sheltered areas. But open sea areas are more suitable to keep favourable environmental conditions and avoid pollution. For this reason, it is also necessary to understand the behavior of net cages as they are exposed to large sea-loads from waves and current. However, in the present study, we will concentrate only on steady water region and on the horizontal effect of the current on a vertically seated obstacle. This means that waves will be neglected.

Volumetric sources of drag. The drag discussed in this section is due to the net alone ("empty net"), as twines act as tiny obstacles evenly distributed on a 2D surface. When the volume enclosed by the net contains a large number of objects (structures, fishes, etc.) these objects are also a source of dissipation and drag. Therefore a *volumetric* source of drag has to be accounted for. This is the approach used in the thesis. This point is discussed in Chapter 2.

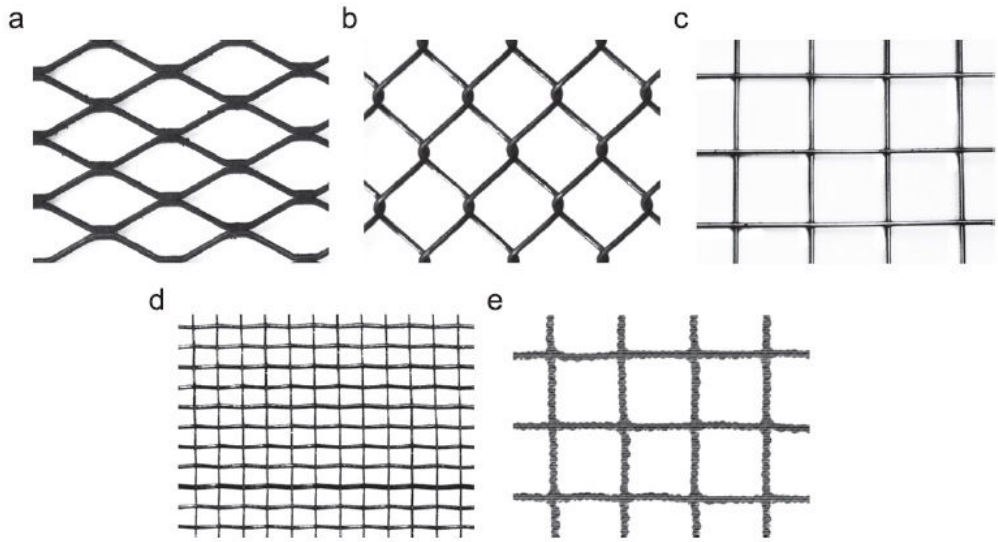

Figure 1.3: *Examples of nettings. (a): flattened expanded copper-nickel, (b): chain-link woven brass, (c): welded siliconbronze, (d): woven silicon-bronze, (e): nylon knotless square net. From Igor Tsukrov (2011)[79].*

1.4 Sediment transport around nets.

Coastal fluid flows bring along billions of particles of various shapes and sizes (see for example Abbott & Francis (1977) [3] ; Bagnold (1966) [6] ; Aldridge (1997) [4] ; Barndorff & Christiansen (1988) [9] ; Barbry (2000) [8], to name but a few references). Obstacles present along the stream cause many changes to the flow itself and to the motion of suspended particles. Indeed, obstacles create wakes, recirculation cells, turbulence, intense unsteady vortices, three-dimensional effects, etc. which significantly affect the motion of particles. In the vicinity of aquaculture cages, these effects are expected to be present, especially if the cage is located in a strong flow area. As discussed at the beginning of this chapter, effluents produced by the cage will also be affected by this complex flow. In addition, the sandbed beneath the cage, where flows are expected to be strong, is likely to be eroded. Therefore, resuspended matter produced below might be transported back into the main flow. These effects have received little attention so far and will be discussed in this thesis.

1.5 Thesis objectives and organization

As described in this chapter, the goal of the thesis is to enhance our understanding of flow and particulate transport in the vicinity of a cage, in the vertical plane. Indeed, the cage itself creates strong vertical gradients of velocity and concentration, which are often neglected in the classical, vertically-averaged, models. Two complementary models (analytical and numerical) will be developed. They will rely on the following approximations:

- two-dimensional flow in the vertical plane,
- rigid rectangular cage,

plus many other approximations that will be described in details later. In spite of these approximations, our models will be compared to flow and turbidity measurements performed in the vicinity of cages installed in the roadstead of Cherbourg. The thesis is organized as follows.

Chapter 2 is an analytical study of the flow through and below an immersed structure. Again, it is based on many approximations (2D flow in the vertical plane, elongated rectangular immersed structure, etc.) but is expected to provide relevant orders-of-magnitude of the various hydrodynamic quantities (velocity and pressure drop) affected by the presence of the cage. It is valid in the limit of highly permeable cages and allows to calculate the reduced velocity inside the cage, as well as the velocity increase below the cage.

Chapter 3 contains a numerical analysis of the same flow, where most of the findings of the analytical model will be confirmed for highly permeable cages. The case of weakly permeable cages will also be considered numerically.

Chapter 4 presents in-situ measurements of current velocities upstream and downstream of the cage. These have been done in October 2016 in the aquaculture farm located in the roadstead of Cherbourg, by means of ADCP facilities. Results are then discussed and compared to our models.

Chapter 5 is devoted to the transport of suspended materials in the vertical plane. It will be shown numerically that the flow perturbation due to the immersed structure can induce a strong vertical mixing which can lead to the "self-contamination" of the cage when its permeability is very small. Results will be compared, qualitatively, to turbidity measurements.

Chapter 6 is the general conclusion of the thesis.

Chapter 2

Analytical model for the flow in the vicinity of immersed structures

Before performing heavy numerical computations at extremely large Reynolds numbers, which are always costly and time consuming, we have chosen to develop an asymptotic analysis of the flow in the vicinity of the farm. It will help us understand the evolution of the flow across the cage, and will bring useful orders-of-magnitudes. In particular, this model will provide an interesting relation between the effective drag coefficient of the net (which measures its lack of permeability) and the pressure drop as well as the velocity perturbation it creates. These information will be used in the next chapters to find the appropriate effective drag coefficient in realistic situations.

2.1 Problem setting and general considerations

The salmon fish farm located in the roadstead of Cherbourg covers an area of about 17 hectares, the depth of the immersed cages being around 10 meters. There have been many researches on the hydrodynamics of such flows, but most of them are 2D analyses in a *horizontal* plane (depth-averaged approaches, see for example Ref. [81]), which do not bring any information about the vertical velocity and concentration gradients. Thus, we consider in this chapter and throughout the thesis a 2D situation in a vertical plane, as sketched in Fig. 2.1, assuming that the net is sufficiently wide to allow this two dimensional approximation. In addition, for the sake

of simplicity, the cage is taken to be a fixed rectangular object denoted as $ABCD$ in Fig. 2.1. The bottom wall is flat and horizontal. The length AB of the cage is denoted as $l_x = x_b - x_a$, and its depth AD is denoted as l_y in the following. The depth of the water column is L_y, and the upstream velocity is U_∞. As expected, the typical Reynolds number of the flow in such a large domain is huge. Indeed, by taking relevant values for the cages in the roadstead of Cherbourg, such as $L_y = 12\,m$ and $U_\infty = 0.5\,m.s^{-1}$, we are led to:

$$Re = \frac{U_\infty L_y}{\nu} \approx 6.10^6 \tag{2.1}$$

where ν is the kinematic viscosity of sea water. The flow is therefore expected to be turbulent and difficult to simulate with a computer, as it presents sharp gradients near walls as well as multi-scale disordered eddies. This is what motivated the asymptotic model developed in this chapter.

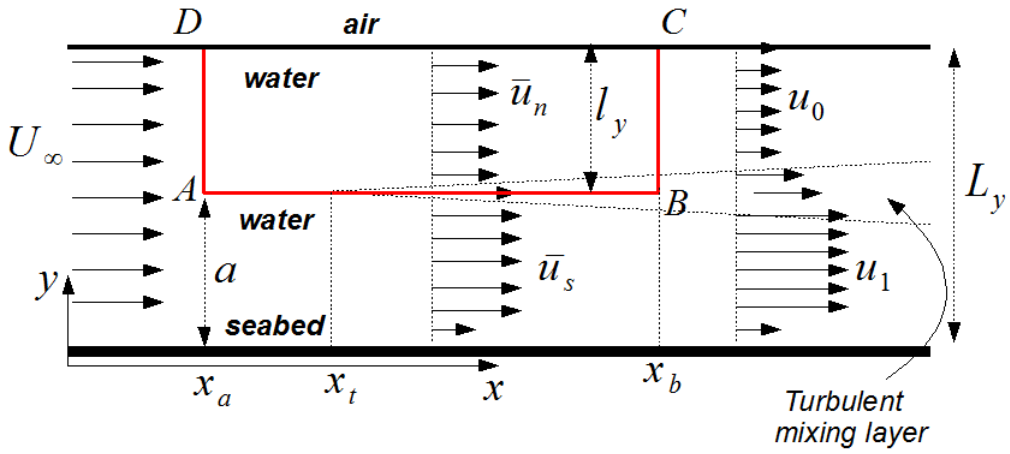

Figure 2.1: *Sketch of a rectangular cage $ABCD$ in the vertical plane. The streamwise flow slows down within the cage ($\bar{u}_n < U_\infty$), and accelerates below ($\bar{u}_s > U_\infty$).*

For *fully impermeable structures* (zero flow rate through the cage), Poizot et al. [70] showed that the flow consists of three parts (Fig. 2.2): a quasi-uniform flow upstream of the obstacle, a very strong flow below and a strong recirculation cell at its rear. In this thesis, cages with a large permeability will be considered, to approach more realistic situations where a non-negligible flow exists through the cage $ABCD$. In particular, no recirculation cell is visible in the wake of such cages, provided their permeability is large enough. The flow structure is therefore simpler, as

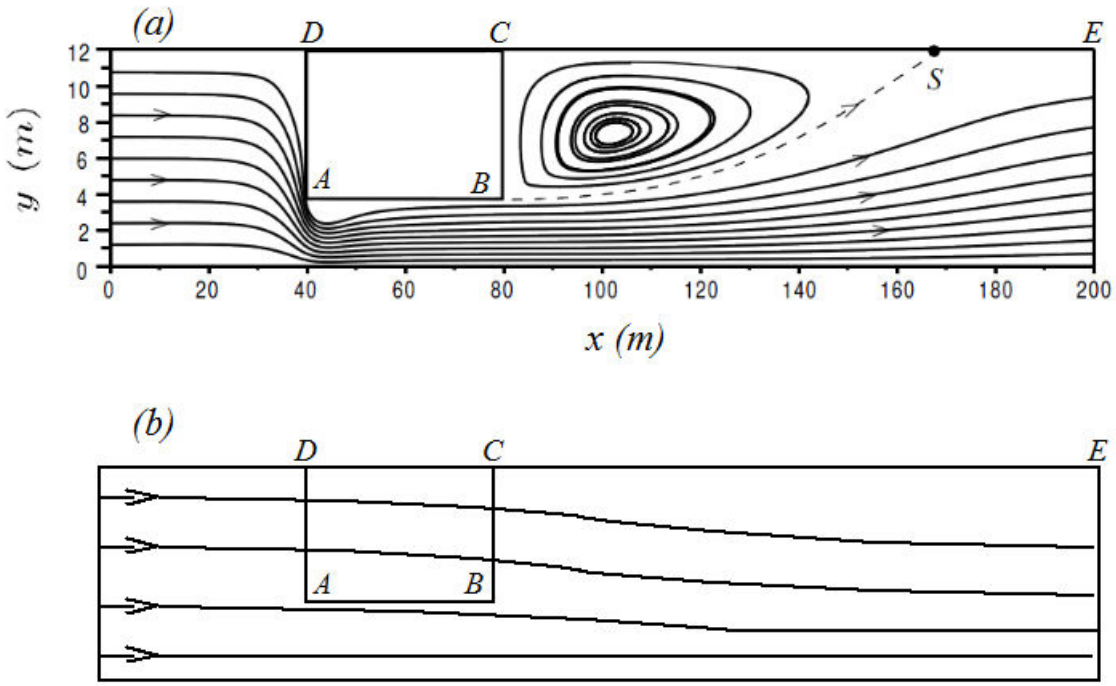

Figure 2.2: *Typical streamlines of the mean flow near a fully impermeable 2D cage ABCD (graph (a), $C_{net} = \infty$, numerical simulations by Poizot et al. [70]). Here, a strong recirculation cell is visible at the rear of the cage. In contrast, for very permeable cages as the ones considered in this thesis, recirculation cells are unlikely and the flow structure is expected to be much simpler (as sketched in graph (b)). Axes are not to scale.*

sketched in Fig. 2.2(b). To model these situations, the immersed obstacle will be taken to be a kind of porous medium, described in the next few lines.

2.1.1 Motion equation and porous medium analogy

In the vertical symmetry plane of the cage, the fluid flow is characterized by the mean velocity $\vec{V} = (\bar{u}(x,y), \bar{v}(x,y))$ and the mean pressure $\bar{P}(x,y)$. Throughout this calculation, in order to get rid of the gravitational force, we denote the value of mean piezometric pressure as $\widehat{P} = \bar{P} + \rho g y$, where y is the upward vertical coordinate. The fluid is assumed to be incompressible and homogeneous, so that

$$\nabla.\vec{V} = 0.$$

The fluid momentum balance equation is:

$$\rho(\nabla\vec{V}).\vec{V} = -\nabla\widehat{P} + \mu\Delta\vec{V} + \nabla.\tau^t + n\vec{F}, \tag{2.2}$$

where μ is the dynamic viscosity of the fluid, ρ is the fluid density, and τ^t is the turbulent stress tensor. The volume force $n(\vec{x})\,\vec{F}(\vec{x})$ appearing in the momentum balance ($\vec{F}$ in newton N and n in m^{-3}), manifests the effect of the cage $ABCD$ on the fluid flow. Indeed, as noticed above, the cage is assumed to be a porous medium defined here as a set of small *elementary obstacles distributed within the whole domain* $ABCD$. The number of obstacles per unit volume is $n(\vec{x})$, and the drag experienced by each obstacle is assumed to be:

$$-\vec{F} = \frac{1}{2} C_D\, s\, \rho |\vec{V}|\vec{V}, \tag{2.3}$$

where C_D is the individual drag coefficient of each object, which is assumed to be constant and identical for all obstacles. The surface s is the apparent surface of each obstacle. This is clearly a very rough approximation for fish farm flows. In particular, the wakes of neighbouring obstacles are assumed not to interact. However, as discussed in the introduction, this approach is widely used in environmental flows (see for example Ref. [81]).

Surface or volume distribution of elementary obstacles ? At this stage, one must define whether the elementary obstacles are distributed over the net only (Fig. 2.3(a)), or inside the entire domain enclosed by the net (Fig. 2.3(b)). In the former case, the solidity of the net, discussed in the introducing chapter, naturally arises in the calculation of the drag (see section 2.1.2 below). We will place ourselves in the latter case, where the drag is induced by the presence of a *volume distribution of fixed obstacles* with individual drag coefficient C_D.

We introduce the coefficient C_{net} of the cage, defined by:

$$n\, l_x\, l_y\, l_z\, \vec{F} = -C_{net} l_y\, l_z\, \frac{1}{2}\, \rho |\vec{V}|\vec{V}, \tag{2.4}$$

which can be thought of as an "effective drag coefficient" of a cage with apparent surface $l_y \times l_z$ and volume $l_x \times l_y \times l_z$ in a uniform flow of velocity $\vec{V}$. It will also be called "impermeability" in this thesis, as it is indeed a measure of the lack of permeability of the cage. It is related to the "individual drag coefficient" C_D as:

$$C_{net} = n(\vec{x})\, l_x\, s\, C_D. \tag{2.5}$$

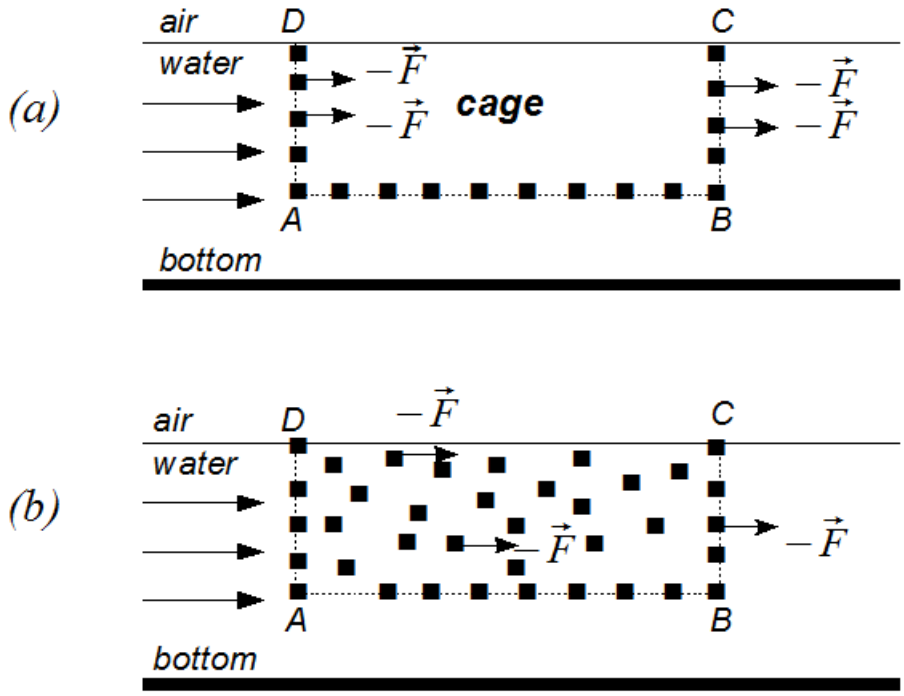

Figure 2.3: *Distribution of elementary obstacles* (■) *in the porous medium analogy. (a): surface distribution, where the drag is induced by the twines of the net only (and by the biofouling of these twines). (b): volumic distribution corresponding to fixed obstacles occupying the entire volume enclosed by the net, together with the net ABCD itself: this is the approach used in this thesis.*

Therefore, even if C_D is small (wing, foil, ...) or of order unity (cube, sphere, ...), the effective drag coefficient C_{net} can be large, because it is proportional to the number of objects per unit volume. It depends on position $\vec{x} = (x, y)$, and is equal to zero outside the cage. Finally, note that the limiting case $C_{net} = 0$ corresponds to a perfectly clean (or to the absence of) cage, and $C_{net} = \infty$, corresponds to the fully impermeable cage studied by Poizot et al. [70] and shown in Fig. 2.2(a).

Under these hypotheses, the Reynolds equations (2.2), projected along the x-direction, read:

$$\bar{u}\frac{\partial \bar{u}}{\partial x} + \bar{v}\frac{\partial \bar{u}}{\partial y} = -\frac{1}{\rho}\frac{\partial \widehat{P}}{\partial x}$$

$$-\frac{\partial}{\partial x}\overline{u'^2} - \frac{\partial}{\partial y}\overline{u'v'} + \nu\left(\frac{\partial^2 \bar{u}}{\partial x^2} + \frac{\partial^2 \bar{u}}{\partial y^2}\right) - \frac{1}{2}\frac{C_{net}}{l_x}\sqrt{\bar{u}^2 + \bar{v}^2}\,\bar{u} \tag{2.6}$$

and in the y-direction:

$$\bar{u}\frac{\partial \bar{v}}{\partial x} + \bar{v}\frac{\partial \bar{v}}{\partial y} = -\frac{1}{\rho}\frac{\partial \widehat{P}}{\partial y}$$

$$-\frac{\partial}{\partial x}\overline{u'v'} - \frac{\partial}{\partial y}\overline{v'^2} + \nu\left(\frac{\partial^2 \bar{v}}{\partial x^2} + \frac{\partial^2 \bar{v}}{\partial y^2}\right) - \frac{1}{2}\frac{C_{net}}{l_x}\sqrt{\bar{u}^2 + \bar{v}^2}\,\bar{v}, \tag{2.7}$$

together with the continuity equation:

$$\frac{\partial \bar{u}}{\partial x} + \frac{\partial \bar{v}}{\partial y} = 0, \tag{2.8}$$

where (u', v') is the fluctuating velocity. For small or moderate C_{net} we conjecture that the flow, for $x_a < x < x_b$ is characterized by four zones (see Fig. 2.1):

- A decelerating flow inside the net $ABCD$, with a horizontal velocity denoted as $\bar{u}_n(x, y)$.
- An accelerating flow below the net $ABCD$, with a horizontal velocity denoted as $\bar{u}_s(x, y)$.
- A mixing-layer between the two previous zones, with thickness $\delta(x) \ll a$ and l_y. This layer extends along segment AB and downstream of this segment.
- A wall boundary layer near the bottom.

In the present model, the bottom wall boundary layer will be neglected, even though it probably dissipates an important part of the kinetic energy. This effect will be left as a perspective.

2.1.2 Link between C_{net} and the drag coefficient of the cage C_X

In the lines above, two drag coefficients have been introduced:

- C_D: drag coefficient of elementary obstacles placed within the cage. It only depends on the shape of objects, and is given by classical hydrodynamic tables.
- C_{net}: the effective drag coefficient of the cage, or "impermeability", which depends on both the shape *and the concentration* $n(\vec{x})$ of elementary obstacles.

These two coefficients are linked by Eq. (2.5). In addition, the total drag experienced by the cage, F_X^{cage}, and the *total drag coefficient* C_X are related by:

$$F_X^{cage} = C_X \frac{1}{2} \rho A U_\infty^2 \tag{2.9}$$

where $A = l_y l_z$ is the apparent surface of the cage. Since F_X^{cage} is the sum of the individual drags experienced by elementary obstacles, we have:

$$F_X^{cage} \vec{i} = - \int_{ABCD} n(\vec{x}) \vec{F} \, dx \, dy \, dz \tag{2.10}$$

where $\vec{i}$ is the unit vector in the x-direction. Assuming that the distribution is uniform (n is constant), this leads to:

$$C_X = C_{net} \int_{x_a}^{x_b} \frac{\sqrt{\bar{u}^2 + \bar{v}^2}}{U_\infty^2} \frac{dx \, dy \, dz}{l_x \, l_y \, l_z} \tag{2.11}$$

One can easily check that $C_X \approx C_{net}$ when C_{net} is small (clean cages). For more and more impermeable cages, C_{net} becomes large, but C_X remains of order unity.

An approximate estimation of C_X ***from*** C_{net}**.** For the sake of simplicity, assume that $\bar{u}$ is constant within the cage, equal to some value u_0, and that $\bar{v}$ is small. Then Eq. (2.11) leads to:

$$C_X \approx C_{net} \left(\frac{u_0}{U_\infty} \right)^2 \tag{2.12}$$

This equation will be used later to estimate C_X. A more accurate expression will be given at the end of this chapter, once the flow equation is solved. Prior to this, we calculate C_X in the case of a surface distribution of elementary obstacles.

2.1.3 Surface distribution of obstacles: link between C_X and solidity

In the case where obstacles are uniformly distributed along the net only (as sketched in Fig. 2.3 (a)), the number of obstacles per unit volume is taken to be:

$$n(\vec{x}) = \frac{N}{S} \delta_S(\vec{x}) \tag{2.13}$$

where N is the total number of obstacles, S is the net surface, and δ_S (m^{-1}) is the Dirac delta function centred on the net surface S, such that:

$$\int_{\mathbf{R}^3} f(\vec{x}) \delta_S(\vec{x}) \, dx \, dy \, dz = \int_S f(\vec{x}) \, dS$$

for any integrable function $f(\vec{x})$. After injecting this $n(\vec{x})$ into Eq. (2.10) we are led to (in projection along x):

$$F_X^{cage} = C_D \frac{1}{2}\rho \frac{N\,s}{S} \int_S \sqrt{\bar{u}^2 + \bar{v}^2}\,\bar{u}\,dS. \tag{2.14}$$

The solidity E_s of the net therefore naturally appears in this expression

$$E_s = \frac{\beta\,N\,s}{S} \tag{2.15}$$

where we have assumed that only the portion AD (the upstream side) of the net contributed to its apparent surface, and β is the proportion of obstacles on this side. This leads to:

$$C_X = C_D\,E_s\,\frac{1}{\beta} \int_S \frac{\sqrt{\bar{u}^2 + \bar{v}^2}\,\bar{u}}{U_\infty^2}\,\frac{dS}{l_y\,l_z}. \tag{2.16}$$

This equation will not be used in the thesis, since we will consider a volumetric distribution.

2.2 Potential flow outside the mixing layer

In the rest of the thesis, we will assume that elementary obstacles are distributed in a uniform volumic manner (as sketched in Fig. 2.3(b)). This means that C_{net} is constant in the interior of the cage, and zero outside.

We first determine the flow outside the mixing or boundary layers ("external flow"), where turbulence and viscosity will be assumed to be absent. We are aware of the fact that turbulence is very likely to occur within the cage, due to the net and the fishes. However, we will neglect this effect in the present work, i.e. we will assume that turbulence is concentrated inside the mixing layer or the bottom boundary layer. In addition, we assume that the cage is strongly permeable and is much longer than deep. Hence, the flow is assumed to be nearly horizontal, as sketch in Fig. 2.2(b).

These assumptions allow us to assume that the velocity field $(\bar{u}, \bar{v})$ in external zones is irrotational:

$$\frac{\partial \bar{v}}{\partial x} - \frac{\partial \bar{u}}{\partial y} = 0, \tag{2.17}$$

and has a strong component towards x, that is

$$|\bar{v}| \ll |\bar{u}|. \tag{2.18}$$

Under these conditions, the horizontal acceleration of fluid points satisfies:

$$\bar{u}\frac{\partial \bar{u}}{\partial x} + \bar{v}\frac{\partial \bar{u}}{\partial y} = \bar{u}\frac{\partial \bar{u}}{\partial x} + \bar{v}\frac{\partial \bar{v}}{\partial x} \simeq \bar{u}\frac{\partial \bar{u}}{\partial x}. \tag{2.19}$$

Indeed, if L is a typical scale of velocity variation along x, we have

$$\bar{u}\frac{\partial \bar{u}}{\partial x} \sim \bar{u}^2/L$$

and

$$\bar{v}\frac{\partial \bar{v}}{\partial x} \sim v^2/L \ll \bar{u}^2/L.$$

Therefore, the streamwise fluid motion equation (2.6) outside the mixing layer takes the simplified form

$$\rho\,\bar{u}(x)\frac{\partial \bar{u}}{\partial x} = -\frac{\partial \widehat{P}}{\partial x} - \frac{1}{2}\rho\frac{C_{net}}{l_x}\bar{u}^2, \tag{2.20}$$

where $\bar{u}$ denotes either $\bar{u}_n$ (inside the cage), or $\bar{u}_s$ (below the cage, with $C_{net} \equiv 0$).

One can argue that the drag force (C_{net} term) appearing in the motion equation is not a gradient in general (i.e. it is not a conservative force). It can therefore be a source of vorticity. However, in the quasi-unidirectional flow considered here, one can check that this effect is small, and that the potential flow approximation is valid outside the mixing layer. Along the line AB however, the discontinuity of this force will be a source of vorticity.

The fluid motion equation (2.7), combined with the continuity equation (2.8) leads to:

$$\rho\,(\bar{u}\frac{\partial \bar{v}}{\partial x} - \bar{v}\frac{\partial \bar{u}}{\partial x}) = -\frac{\partial \widehat{P}}{\partial y} - \frac{1}{2}\rho\frac{C_{net}}{l_x}\bar{u}\bar{v}, \tag{2.21}$$

where we neglected viscosity and made use of approximation (2.18). This result shows that, *as long as C_{net} is below a few units*, we have:

$$|\frac{\partial \widehat{P}}{\partial y}| \sim \rho\frac{\bar{u}\bar{v}}{L} \ll \rho\frac{\bar{u}^2}{L} \sim |\frac{\partial \widehat{P}}{\partial x}|. \tag{2.22}$$

The transverse (piezometric) pressure gradient is therefore much smaller than the streamwise gradient:

$$|\frac{\partial \widehat{P}}{\partial y}| \ll |\frac{\partial \widehat{P}}{\partial x}|. \tag{2.23}$$

In addition to these approximations, we make use of results of numerical simulations (presented in the next chapters) which show that, as long as C_{net} is not too large, we have for all $x \in [x_a, x_b]$:

$$\frac{\partial \widehat{P}}{\partial x} = \text{negative constant} \equiv -\alpha \tag{2.24}$$

where α denotes the absolute value of the pressure gradient. The pressure drop along x is due to the drag of the net. If the upper bound corresponds to an air/water interface $y = H(x)$, then $\widehat{P}(x, H) = P_{atm} + \rho g H(x)$, and the piezometric pressure loss corresponds to a (slight) decrease in the height of the interface ($H(x)$ decays with x), since the absolute pressure at $y = H(x)$ is constant and equal to the atmospheric pressure. In practice this effect is negligible and the numerical simulations can be performed by assuming a horizontal air/water interface.

For $x > x_b$, that is behind the cage, the mean flow is composed of a slow stream with horizontal velocity $\bar{u}_n(x_b)$ for $y > a + \delta$ of a fast stream with velocity $\bar{u}_s(x_b)$ for $y < a - \delta/2$, and a mixing layer of thickness $\delta(x)$ expanding between the two.

Flow inside the cage, outside the mixing layer.

By including Eq. (2.24) into (2.20), we are lead to:

$$\rho \bar{u}_n(x)\bar{u}_n'(x) = \alpha - \frac{1}{2}\rho \frac{C_{net}}{l_x}\bar{u}_n^2, \tag{2.25}$$

which can be readily integrated, using the condition $\bar{u}_n(x_a) = U_\infty$, and gives:

$$\bar{u}_n^2(x) = \frac{2\,\alpha\, l_x}{\rho\, C_{net}} + \left(U_\infty^2 - \frac{2\,\alpha\, l_x}{\rho C_{net}}\right) e^{-C_{net}(x-x_a)/l_x} \tag{2.26}$$

In particular, the (squared) velocity of the fluid exiting the cage at $x = x_b$, above the mixing layer, reads:

$$\bar{u}_0^2(x_b) = \frac{2\,\alpha\, l_x}{\rho\, C_{net}} + \left(U_\infty^2 - \frac{2\,\alpha\, l_x}{\rho\, C_{net}}\right) e^{-C_{net}}. \tag{2.27}$$

Flow below the cage, outside the mixing layer.

The same arguments, applied to the quasi-horizontal flow $\bar{u}_s(x)$ below the cage lead to:

$$\rho\, \bar{u}_s(x)\bar{u}_s'(x) = \alpha \tag{2.28}$$

so that:

$$\bar{u}_s^2(x) = U_\infty^2 + \frac{2\,\alpha}{\rho}(x - x_a), \tag{2.29}$$

and the velocity of the fluid exiting the bottom zone of the cage is:

$$\bar{u}_s^2(x_b) = U_\infty^2 + \frac{2\,\alpha}{\rho} l_x. \tag{2.30}$$

In addition, flow rate conservation, in this 2D configuration, reads:

$$U_\infty L_y = \bar{u}_n(x_b)\, l_y + \bar{u}_s(x_b)\, a, \tag{2.31}$$

even if the velocity profile is smoothed out in the mixing layer, provided $\delta(x) \ll a$ and l_y.

Flow at the rear of the cage, outside the mixing layer

Because our experimental approach will be devoted to current measurements at the rear of the cage, we are particularly interested in determining $\bar{u}_n(x_b)$ and $\bar{u}_s(x_b)$, as well as the pressure drop α, in terms of the various parameters of the problem. Equations (2.27), (2.30) and (2.31) can be solved to determine these three unknowns. After some algebra we are led to:

$$u_0 \equiv \bar{u}_n(x_b) = U_\infty \frac{\sqrt{B^2 - AC} - B}{A}, \tag{2.32}$$

$$u_1 \equiv \bar{u}_s(x_b) = U_\infty \left[1 + \frac{l_y}{a} - \frac{l_y}{a}\frac{\sqrt{B^2 - AC} - B}{A}\right], \tag{2.33}$$

$$\alpha \equiv -\frac{\partial \widehat{P}}{\partial x} = \frac{1}{2}\frac{\rho U_\infty^2}{l_x}\left[\left(1 + \frac{l_y}{a} - \frac{l_y}{a}\frac{\sqrt{B^2 - AC} - B}{A}\right)^2 - 1\right], \tag{2.34}$$

where A, B and C are functions of C_{net} and of the sole ratio l_y/a:

$$A(C_{net}, \frac{l_y}{a}) = 1 - \frac{1 - e^{-C_{net}}}{C_{net}}\left(\frac{l_y}{a}\right)^2, \tag{2.35}$$

$$B(C_{net}, \frac{l_y}{a}) = \frac{1 - e^{-C_{net}}}{C_{net}}\left[\left(\frac{l_y}{a}\right)^2 + \frac{l_y}{a}\right], \tag{2.36}$$

$$C(C_{net}, \frac{l_y}{a}) = \frac{e^{-C_{net}} - 1}{C_{net}}\frac{l_y}{a}(\frac{l_y}{a} + 2) - e^{-C_{net}}. \tag{2.37}$$

To shorten notations, Eq. (2.34) will be written:

$$\alpha = \frac{1}{2}\frac{\rho U_\infty^2}{l_x} K(C_{net}, \frac{l_y}{a}) \tag{2.38}$$

where

$$K(C_{net}, \frac{l_y}{a}) = \left(1 + \frac{l_y}{a} - \frac{l_y}{a}\frac{\sqrt{B^2 - AC} - B}{A}\right)^2 - 1. \tag{2.39}$$

Also, we have chosen to simply note u_0 in place of $\bar{u}_n(x_b)$ and u_1 in place of $\bar{u}_s(x_b)$, as these quantities will be extensively used below. The piezometric pressure difference between the inlet and the outlet of the cage is simply αl_x, that is:

$$\widehat{P}(x_a) - \widehat{P}(x_b) = \frac{1}{2}\rho U_\infty^2 K(C_{net}, \frac{l_y}{a}). \tag{2.40}$$

If one works with a free air/water surface, the decay of the height of the interface $H(x)$ between sections $x = x_a$ and $x = x_b$ will be given by:

$$H_a - H_b = \frac{\widehat{P}(x_a) - \widehat{P}(x_b)}{\rho\, g} = \frac{U_\infty^2}{2g}\left[\left(1 + \frac{l_y}{a} - \frac{l_y}{a}\frac{\sqrt{B^2 - AC} - B}{A}\right)^2 - 1\right]. \tag{2.41}$$

One can check that it is negligible for the parameters considered in this thesis: this is the reason why numerical simulations of Chapter 3 will involve a simple rigid air/water interface with a stress-free boundary condition.

Equations (2.32), (2.33) and (2.40) are the main result of this section: they will be compared to simulations and in-situ measurements in the next chapters. Prior to that, we study the flow equation inside the mixing layer to derive an appropriate expression for the complete mean velocity profile from bottom to top.

The resultant drag of elementary obstacles

Since the velocity $\bar{u}_n(x)$ inside the cage is known, one can make use of Eq. (2.11) to evaluate the total drag coefficient due to the entire set of elementary obstacles present in the cage. After some algebra we are led to:

$$C_X = K(C_{net}) + \left(1 - \frac{K(C_{net})}{C_{net}}\right)(1 - e^{-C_{net}}) \tag{2.42}$$

Note that it only contains the contribution of the flow outside the mixing layer. One can check that, when $C_{net} \to 0$, this expression leads to $C_X \to 0$, as expected.

2.3 Flow inside the mixing layer

Due to the velocity difference $u_1 - u_0$, a mixing layer arises somewhere below the cage (at $x = x_t$, say) and extends in the downstream direction. Even if this velocity difference is only of a few 10 $cm.s^{-1}$, the large Reynolds numbers considered here allow us to treat the mixing layer as a turbulent one. This is done in the next sections, to determine the mean streamwise velocity profile.

2.3.1 Normalized flow transport equations in the case of strongly permeable cages

We will non-dimensionalize the Reynolds equations (2.6)-(2.7), by using relevant orders-of-magnitude. Then, dominant terms only will be conserved to derive a simplified model involving the key quantities. The approach is classical, and can be found for example in the book by Candel [14].

We assume that the mixing layer is thin, with a thickness denoted as $\delta(x)$. The typical value of $\delta(x)$, denoted Δ, is therefore assumed to satisfy:

$$\Delta \ll l_y \ll l_x = x_b - x_a.$$

In addition, we assume here that the cage is strongly permeable, i.e. that C_{net} is small enough (this will be rigorously specified later, in Eq. (2.52)). This implies that $u_1 - u_0$ is much smaller than $(u_1 + u_0)/2$, which is itself of the order of the upstream flow U_∞:

$$\frac{|u_1 - u_0|}{u_1 + u_0} \ll 1. \tag{2.43}$$

Within the mixing layer, variables are non-dimensionalized as follows:

$$x = x_* l_x, \quad y = y_* \, \Delta, \quad \bar{u}(x,y) = U_\infty u_*(x_*, y_*), \quad \bar{v}(x,y) = V \, v_*(x_*, y_*), \tag{2.44}$$

where starred variables are assumed to be of order unity, and the order-of-magnitude V is *a priori* unknown. Equations (2.44) manifest the fact that vertical gradients, inside the mixing layer, are much stronger than horizontal gradients. The continuity equation reads:

$$\frac{U_\infty}{l_x}\frac{\partial u_*}{\partial x_*} + \frac{V}{\Delta}\frac{\partial v_*}{\partial y_*} = 0, \tag{2.45}$$

so that the coherence of this equation requires $V \sim U_\infty \Delta / l_x$. We therefore set:

$$V := U_\infty \frac{\Delta}{l_x} \ll U_\infty.$$

Let $\tilde{u}$ be the order-of-magnitude of turbulent fluctuations within the mixing layer:

$$u' = \tilde{u} \, u'_*, \quad v' = \tilde{u} \, v'_*.$$

Then, let us write $\widehat{P} = \widehat{P}_* \, \rho U_\infty^2$. Under these hypotheses the Reynolds equations inside the mixing layer read:

$$u_* \frac{\partial u_*}{\partial x_*} + v_* \frac{\partial u_*}{\partial y_*} = -\frac{\partial \widehat{P}_*}{\partial x_*} - \left(\frac{\tilde{u}}{U_\infty}\right)^2 \frac{\partial}{\partial x_*} \overline{u'^2_*}$$

$$-\left(\frac{\tilde{u}}{U_\infty}\right)^2 \frac{l_x}{\Delta}\frac{\partial}{\partial y_*}\overline{u'_* v'_*} + \frac{\nu}{U_\infty l_x}\left(\frac{\partial^2 u_*}{\partial x_*^2} + \left(\frac{l_x}{\Delta}\right)^2 \frac{\partial^2 u_*}{\partial y_*^2}\right) - \frac{1}{2}C_{net}u_*^2 \tag{2.46}$$

and:

$$u_*\frac{\partial v_*}{\partial x_*} + v_*\frac{\partial v_*}{\partial y_*} = -\left(\frac{l_x}{\Delta}\right)^2 \frac{\partial \widehat{P}_*}{\partial y_*} - \left(\frac{l_x}{\Delta}\right)\left(\frac{\tilde{u}}{U_\infty}\right)^2 \frac{\partial}{\partial x_*}\overline{u'_* v'_*}$$

$$-\left(\frac{l_x}{\Delta}\right)^2\left(\frac{\tilde{u}}{U_\infty}\right)^2 \frac{\partial}{\partial y_*}\overline{v_*'^2} + \frac{\nu}{U_\infty l_x}\left(\frac{\partial^2 v_*}{\partial x_*^2} + \frac{\partial^2 v_*}{\partial y_*^2}\left(\frac{l_x}{\Delta}\right)^2\right) - \frac{1}{2}C_{net}|u_*|\, v_*. \tag{2.47}$$

2.3.2 Identification of dominant terms

Equations (2.46)-(2.47) highlight various non-dimensional ratios, the order-of-magnitude of which can be easily determined. In particular, we have:

$$\frac{l_x}{\Delta} \gg 1.$$

The ratio $\tilde{u}/U_\infty$ is the order of turbulent intensity. It seems coherent to assume that $\tilde{u} \sim |u_1 - u_0|$, so that (2.43) implies:

$$\frac{\tilde{u}}{U_\infty} \ll 1.$$

Finally, the Reynolds number $U_\infty l_x/\nu$ is clearly very large. The reduced equation (2.47), to leading order, implies:

$$\frac{\partial \widehat{P}_*}{\partial y_*} = 0 \tag{2.48}$$

so that the piezometric pressure is constant in each cross-section, like in the external flows. This quantity will be matched with pressure in the uniform zones satisfying Eq. (2.25).

If we add the constraint

$$\left(\frac{\tilde{u}}{U_\infty}\right)^2 \frac{l_x}{\Delta} = O(1)$$

and keep orders $O(1)$ in (2.46), and use Eq. (2.38) reproduced here in non-dimensional form:

$$\frac{\partial \widehat{P}_*}{\partial x_*} = -\frac{1}{2}C_{net}U_\infty^{*2}\, K \tag{2.49}$$

where $K(C_{net}, l_y/a)$ is a constant of order unity (and $U_\infty^* \equiv 1$), we get:

$$u_*\frac{\partial u_*}{\partial x_*} + v_*\frac{\partial u_*}{\partial y_*} = -\left(\frac{\tilde{u}}{U_\infty}\right)^2 \frac{l_x}{\Delta}\frac{\partial}{\partial y_*}\overline{u'_* v'_*} - \frac{1}{2}C_{net}(u_*^2 - K\, U_\infty^{*2}). \tag{2.50}$$

The drag term appearing in this equation is proportional to the difference between u_* and $U_\infty^*\sqrt{K}$. It is therefore of the order of $C_{net}\tilde{u}/U_\infty$. Therefore, if

$$C_{net}\frac{\tilde{u}}{U_\infty} \ll \left(\frac{\tilde{u}}{U_\infty}\right)^2 \frac{l_x}{\Delta} \sim 1, \tag{2.51}$$

the drag term will be negligible in Eq. (2.50) and the two other terms will remain. This condition is not very strong, as it can be satisfied even if C_{net} is larger than unity. One just has to make sure that:

$$C_{net} \ll \left(\frac{\tilde{u}}{U_\infty}\right) \frac{l_x}{\Delta}. \tag{2.52}$$

Under these conditions, Eq. (2.50) becomes:

$$u_*\frac{\partial u_*}{\partial x_*} + v_*\frac{\partial u_*}{\partial y_*} = -\left(\frac{\tilde{u}}{U_\infty}\right)^2 \frac{l_x}{\Delta}\,\frac{\partial}{\partial y_*}\overline{u_*'v_*'}. \tag{2.53}$$

This is the turbulent Prandtl equation without pressure gradient. To close these equations we will make use of the Boussineq hypothesis:

$$\overline{u'v'} = -\nu_T(x,y)\,\frac{\partial \bar{u}}{\partial y} \tag{2.54}$$

where the turbulent kinematic viscosity is taken to be much larger than the molecular viscosity:

$$\nu_T \gg \nu.$$

Coming back to dimensional variables we get the reduced dimensional Prandtl equations inside the mixing layer:

$$\bar{u}\frac{\partial \bar{u}}{\partial x} + \bar{v}\frac{\partial \bar{u}}{\partial y} = \frac{\partial}{\partial y}\left(\nu_T\frac{\partial \bar{u}}{\partial y}\right). \tag{2.55}$$

The matching conditions for velocity are taken to be:

$$\bar{u}(x,+\infty) = u_0 \quad \text{et} \quad \bar{u}(x,-\infty) = u_1. \tag{2.56}$$

This is therefore a classical mixing layer without pressure gradient. One should not believe however that C_{net} is absent from this model: the effect of the net appears in boundary conditions u_0 and u_1 (Eqs. (2.32) and (2.33)), which depend on C_{net}.

2.4 Mixing length model and self-similar solution

To solve the equation (2.55) above, we have to find a model for turbulent viscosity. Numerical simulations suggest to choose a model of the form:

$$\nu_T = \kappa(x - x_a)(u_1 - u_0) \tag{2.57}$$

where κ is a non-dimensional constant. Under these conditions, invariant subgroup analysis of Eq. (2.55) shows that there exists a self-similar solution in terms of the reduced variable:

$$\xi = \sigma \frac{y - a}{x - x_t} \tag{2.58}$$

where σ is the spread rate of the mixing layer and x_t is x-coordinate of the origin of the turbulent zone.

2.4.1 Mean velocity

The self-similar solution of Eq. (2.55), first exhibited by Goertler [39], reads:

$$\bar{u} \simeq \frac{u_1 + u_0}{2} - \frac{u_1 - u_0}{2}\mathrm{erf}(\xi). \tag{2.59}$$

It has been obtained to leading order in $|(u_1 - u_0)/(u_1 + u_0)|$ (see for example Candel [14] for a detailed derivation). The spread rate σ is related to the reduced velocity difference by the empirical formula:

$$\sigma = \sigma_0 \frac{u_1 + u_0}{u_1 - u_0},$$

where the non-dimensional constant σ_0 has been measured by means of various experiments [85], and one usually takes $\sigma_0 \simeq 11$. The non-dimensional constant κ is related to the spread rate by:

$$\kappa = \frac{1}{4\sigma^2}\frac{u_1 + u_0}{u_1 - u_0} = \frac{1}{4\sigma_0^2}\frac{u_1 - u_0}{u_1 + u_0} \tag{2.60}$$

2.4.2 Second-order moments and turbulent intensity

Once the average velocity is known, the Boussinesq hypothesis allows to calculate the moments of 2nd order. We obtain:

$$\overline{u'v'} = q_{uv}\,(u_1 - u_0)^2\, e^{-\xi^2} \tag{2.61}$$

where the constant q_{uv} is given by:

$$q_{uv} = \frac{1}{4\sigma_0\sqrt{\pi}} \approx 0.013 \tag{2.62}$$

The moment $\overline{u'u'}$ is out of reach of the model, but is taken to be of a similar form:

$$\overline{u'u'} = q_{uu}\,(u_1 - u_0)^2\, e^{-\xi^2} \tag{2.63}$$

where the constant q_{uu} has been studied experimentally [85]: $0.025 \leq q_{uu} \leq 0.034$. The turbulent intensity at any point (x, y) is:

$$I(x,y) = \frac{\sqrt{\overline{u'u'}}}{\overline{u}} = \frac{\sqrt{q_{uu}}\,(u_1 - u_0)\, e^{-\xi^2/2}}{\frac{u_1+u_0}{2} - \frac{u_1-u_0}{2}\mathrm{erf}(\xi)}. \tag{2.64}$$

It is maximum and independent of x along the axis of the mixing layer $y = a$:

$$I_0 \equiv I(x,a) = 2\sqrt{q_{uu}}\,\frac{u_1 - u_0}{u_1 + u_0}. \tag{2.65}$$

By using the results of the previous section, we obtain the turbulent intensity in terms of the effective drag coefficient C_{net} and of the ratio l_y/a:

$$I_0 = 2\sqrt{q_{uu}}\,(\frac{l_y}{a} + 1)\,\frac{A + B - \sqrt{B^2 - AC}}{(\sqrt{B^2 - AC} - B)(1 - \frac{l_y}{a}) + A(1 + \frac{l_y}{a})}. \tag{2.66}$$

2.5 A preliminary result from the asymptotic model

To illustrate these formulas, we have chosen to plot a single key quantity appearing in this model, namely u_0/U_∞ the slow velocity at the exit of the net, being understood that more results will be presented and compared to simulations and in-situ measurements in the next chapters.

Figure 2.4 shows a comparison between our result of Eq. (2.32) and three numerical simulations. Two simulations have been performed by using the OpenFoam software (post-doc of Romuald Verjus, 2015), and one has been done by means of the Fluent software presented in the next chapter. The same computational domain is used for the three computations, only the upstream velocity U_∞ differs. Agreement between numerics and theory is acceptable in regard of the numerous approximations of the model and of the fact that no parameter has been tuned ad hoc. Discrepancies are due to the limitations of the theoretical model which neglects some important and realistic physical aspects, like the boundary layer near the bottom ($y = 0$). Indeed, because the bottom boundary layer is not accounted for in the theoretical model, the velocity

u_1 below the cage is overestimated, so that the velocity u_0 inside the cage is underestimated. This explains why numerical predictions are above the theoretical curve, with an error from a few percent to about 15%.

This preliminary result is encouraging, and will allow us to estimate what C_{net} should be used in realistic situations. Indeed, suppose one measures the velocity inside and/or below the net, then Eq. (2.4) will directly indicate what effective drag coefficient should be used to mimic the effect of the cage. This will be done in Chapter 4. Prior to this, the numerical modelling of the cage is presented in the next chapter.

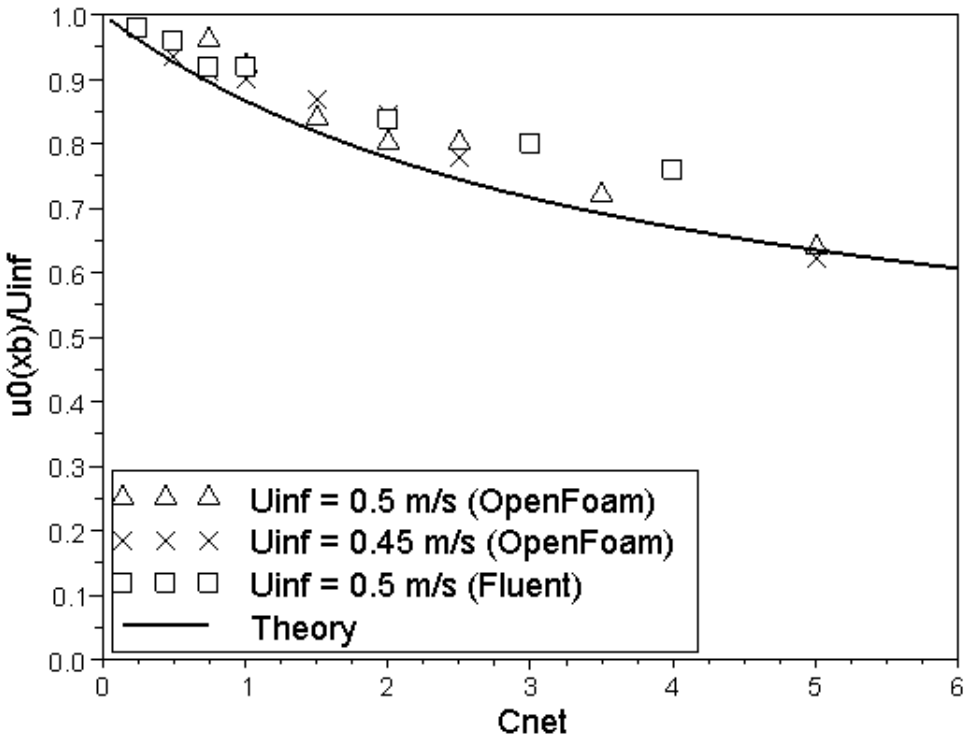

Figure 2.4: *Plot of the ratio u_0/U_∞ (solid line), versus the effective drag coefficient of the cage, obtained from the analytical solution (2.32), with $U_\infty = 0.5\,m.s^{-1}$, $L_y = 12\,m$, $l_y = 8\,m$. Symbols correspond to three simulations done with slightly different numerical solvers, using a similar domain. OpenFoam computations have been done during the post-doc of R. Verjus (2015), Fluent computations have been performed during the present thesis. This curve will be used to estimate the effective C_{net} of real cages (see Chapter 4).*

2.6 Conclusion of this chapter

We have derived a simple set of formulas to determine the perturbation of the flow due to the presence of the permeable cage, in the limit of very large Reynolds numbers. The lack of permeability of the cage was characterized by the effective drag coefficient C_{net} which has been rigorously defined. The model is based on a few approximations, some of which can be removed in a next version and are listed in the next few lines.

Turbulence intensity within the cage. It is zero in both the analytical and the numerical models, but one can add this effect, provided turbulence intensity can be measured within the cage. Indeed, the inner cage itself is a source of turbulence due to the net and to the presence of the numerous small-scale objects ("fishes") within the cage. Accounting for this source of turbulence could be done the same way as in Caton et al. [18] (urban flows).

Absence of pressure gradient inside the mixing layer. Inside the mixing layer, the C_{net} term has no effect to leading order, so that Eq. (2.50) could be approximated by the classical Prandtl equation (2.55). This is valid only if C_{net} is moderate and satisfies the asymptotic condition (2.52). If this condition is removed (very large C_{net}), then Eq. (2.50) has to be solved instead of (2.55). This is feasible at least numerically, as a self-similar solution has not been shown to exist in this case to the best of our knowledge.

Bottom boundary layer. The bottom boundary layer is absent from this model. This is clearly a serious limitation of the theory, and a non-trivial one. We believe it can be solved, in the near future, by considering the Prandtl equation in the vicinity of the bottom wall $y = 0$. Here, the C_{net} term does not exist (and does not balance the longitudinal pressure drop), but the longitudinal pressure drop in the uniform flow zone below the net (where velocity is equal to u_0) will induce a pressure gradient inside the bottom boundary layer. The analytical model will then require to solve the turbulent Prandtl equation *with* constant pressure gradient, which will not lead to the classical logarithmic law-of-the-wall. Note that this limitation will also make the numerical computations approximate as soon as standard wall functions are used.

Constant and moderate C_{net}. We have assumed that C_{net} was piecewise constant, i.e. that fishes are uniformly distributed within the cage. If fishes accumulate near the bottom of the cage, as can be observed in real farms, one has to introduce variable C_{net}'s in the model. In

addition, the present theory requires the drag coefficient to be moderate, and cannot predict the hydrodynamics of very impermeable cages.

Most of the limitations and perspectives described in the above lines will require the use of computational techniques, like the one described in the next chapter.

Chapter 3

Numerical modeling of the flow in the vicinity of an immersed structure

To validate the theoretical calculations proposed in the previous chapter, numerical simulations have been carried out by means of a finite volume model (Fluent). The $k-\omega$ SST turbulence model has been used, for its ability to give convincing results in flows where boundary layer separation and reattachment occur. The physical hypotheses and the numerical method will be discussed first. Then, numerical results concerning the flow structure, pressure drop and velocity profiles will be presented and compared to the analytical model whenever possible.

3.1 Introduction

Nowadays, with the rapid development of science and technology, more and more computational methods have been introduced to solve complex problems of fluid mechanics. Hence, a large variety of methods can be used to simulate a flow in either simple or complex geometries. Regarding aquacultural fish nets, numerous research works have already been carried out and proposed valuable results and conclusions, with different kinds of approaches and approximations (see for example Ref. [81] and references therein). Generally speaking, there exists no universal model to cover all fluid dynamics problems, even for newtonian fluids in simple geometries as considered here in our 2D model. Indeed, when the Reynolds number is very large turbulence

plays a key role in friction, energy dissipation, mixing, and detachment of boundary layers. Unfortunately, different turbulence models can then lead to very different mean flows and forces, and to paradoxical results. In spite of these difficulties, we aim at developing a model that should be as simple as possible, but should capture the relevant physical properties of interest. In addition, the transport of suspended sediments should also be included in this model (this will be discussed in Chapter 5).

According to Huang et al. [49], and Zhao et al. [88] [10], the inertial force on a fishing net is rather small compared to external forces, and can be neglected. In the present work, the net has been assumed to have a fixed rectangular shape, and its dynamics is completely frozen: only the force balance on the fluid has to be considered. The fishnet cage has been taken to be the same porous medium as in the previous chapter, modeled with an effective drag coefficient C_{net}, and the fluid flow through the net satisfies the Reynolds equations (2.6)-(2.7), together with the continuity condition (2.8). The C_{net} terms appearing in Eqs. (2.6)-(2.7) have been introduced into the Fluent code by means of User Defined Functions.

In the next section, some turbulence models are quickly recalled. The reader familiar with such models may skip this part.

3.2 A short review of 1st order turbulence models

3.2.1 Averaging process - Boussinesq's hypothesis

In turbulent flows, the detailed structure of instantaneous fields is not reproducible. However, statistical moments are reproducible, and these are key quantities for the scientist as well as the engineer (Candel [14], Chassaing [20]). This is the reason why one often decomposes the instantaneous velocity v_i as a mean velocity $V_i \equiv \bar{v_i}$ plus a fluctuating velocity v_i':

$$v_i(\vec{x},t) = V_i(\vec{x},t) + v_i'(\vec{x},t), \quad \overline{v'}_i = 0, \tag{3.1}$$

the average operator $\overline{(.)}$ being the ensemble average, that is the average over a large number of realizations of the flow. (It can also be taken as the time average of a single realization if the ergodic hypothesis applies.) A similar decomposition applies for pressure, and any other variable field if any. Assuming that averaging operator commutes with derivatives, and that

$\overline{\bar{a}b} = \bar{a}\,\bar{b}$, the Navier-Stokes equations lead to the Reynolds equations (or RANS[1]) (2.6)-(2.7) of page 26, reproduced here in index notation and repeated indices summation ($v_1 \equiv u$, $v_2 \equiv v$):

$$\frac{\partial V_j}{\partial x_j} = 0, \tag{3.2}$$

$$\frac{\partial V_i}{\partial t} + \frac{\partial V_i}{\partial x_j} V_j = -\frac{1}{\rho}\frac{\partial P}{\partial x_i} + \nu \frac{\partial^2 V_i}{\partial x_j \partial x_j} - \frac{\partial}{\partial x_j}\,\overline{v_i' v_j'} + nF_i/\rho, \tag{3.3}$$

where the volume force F_i due to the cage has been defined in Chapter 2 (Eq. (2.4)). Therefore, the motion equation of the mean flow is the classical Navier-Stokes equation plus the divergence of a new stress ("Reynolds stress"):

$$\tau_{ij}^t = -\rho \overline{v_i' v_j'} \tag{3.4}$$

which manifests the effect of turbulence on the mean flow. To solve (3.2)-(3.3) one has to calculate, or model, this tensor. For that, various models exist according to their degree of accuracy.

Boussinesq's hypothesis and 1st order models. On can model this tensor directly, by relating it to the mean flow. Doing this, Eqs. (3.2)-(3.3) will be *closed*, and can be solved provided one makes use of appropriate boundary conditions for the average quantities V_i and P. These are "1st order" models because the closure appears explicitly in the equation of the 1st order moment $\bar{v}_i \equiv V_i$. The most common closure is the Boussinesq hypothesis which relates turbulent stresses to zones where mean deformation is present:

$$-\overline{v_i' v_j'} + \frac{2}{3} k\,\delta_{ij} = \nu_T \Big(\frac{\partial V_i}{\partial x_j} + \frac{\partial V_j}{\partial x_i} \Big), \quad k = \frac{1}{2}\overline{v_j' v_j'}. \tag{3.5}$$

This model introduces two new unknown variables: the turbulent viscosity $\nu_T(\vec{x}, t)$ (in units of $m^2.s^{-1}$, also called eddy viscosity) and the turbulent kinetic energy per unit mass k (in units of $J.kg^{-1}$). This is precisely the equation used in the theoretical model of Chapter 2, where a turbulent viscosity had been introduced and modeled by means of a mixing length hypothesis (see Eqs. (2.54) and (2.57) page 36).

If no other equation is necessary to close (3.2)-(3.3), like in our theoretical model, one talks about a "1st order model with 0 transport equation", i.e. no extra transport equation is needed to determine all quantities. This is the most common model for turbulent mixing layers (mixing length model) or turbulent boundary layers. If one needs an extra (closed) transport equation

[1] Reynolds Averaged Navier-Stokes equations.

to determine either ν_T or k, then the model is a "1st order model with 1 transport equation" (e.g. the Spalart-Allmaras model).

Models with 2 transport equations. If turbulent viscosity is assumed to depend only on k and on the viscous dissipation rate of turbulent kinetic energy ε (in units of W/kg), then dimensional analysis leads to:

$$\nu_T = C_\mu k^2/\varepsilon,$$

where C_μ is a non-dimensional constant close to 0.09. A transport equation has then to be introduced, and closed, to determine ε, and we obtain the family of $k-\varepsilon$ models which are the most widely used 1st order models with 2 equations. If, instead of considering the dissipation rate ε, one introduces the specific dissipation rate $\omega = \varepsilon/k$ (in units of s^{-1}) to model the turbulent viscosity, dimensional analysis leads to:

$$\nu_T = \alpha^* k/\omega,$$

where α^* is a non-dimensional constant. This is the $k-\omega$ model of Wilcox, which is also a 1st order model with 2 transport equations (one for k and one for ω). It has been shown to be efficient near walls. It is a variant of this model that will be used in the present chapter, an which is presented below. For higher-order models, we refer the reader, for example, to the book by Chassaing [20].

3.2.2 SST $k-\omega$ model

This is the model that will be used in the present thesis. Like the $k-\varepsilon$ and the $k-\omega$ models, the SST $k-\omega$ turbulence model is a 2 equation model based on the concept of turbulent viscosity (Boussinesq hypothesis) briefly described above. It can be thought of as a combination of the $k-\varepsilon$ and the $k-\omega$ models, and has been designed to be efficient near walls as well as in the free stream (away from walls). A "blending function" is used to activate the $k-\varepsilon$ in the free stream, and the $k-\omega$ model near walls. However, the STT $k-\omega$ model requires highly meshed domains to resolve the laminar sub-layer, so that the dimensionless wall distance of the first node should be $y^+ \sim 1$. In practice, one can hardly reach this critical value of y^+, and it is difficult for the model to converge in general, so one has to accept results where residuals drop down about 4 orders.

Model	Advantages	Disadvantages
Mixing-Length Model	• Easy to implement, requiring less computing resources • Well-established • Suitable for thin shear layers (e.g. jets, wakes)	• Incapable for flows with separation/recirculation
Spalart-Allmaras	• Algrebraic calculation of length scale provides economic computations • Good results in flows with adverse pressure gradients • Suitable for external aerodynamics	• Definition of length scale difficult given complex geometries
Standard k-ε	• Need only supply initial and/or boundary conditions • Performs well for many industrially-relevant flows • Most validated model	• Extremely poor performance in flows with adverse pressure gradients leading to separation/recirculation
Wilcox k-ω	• Integration of flow solution to the wall does not require extra damping functions for low-Re regimes • Turbulent boundary conditions prescribed at the wall (k=0, $\omega \rightarrow \infty$)	• Prediction of separation is early and excessive
SST k-ω	• Blending functions allows use of k-ω model near-wall and k-ε in fully turbulent region far from wall • Excellent agreement for flows with or without adverse pressure gradients	• Extra functions increase complexity and computational resources required

Figure 3.1: *Comparison of turbulence models, reproduced from Ref. [83].*

3.3 Numerical computation of the 2D flow near the cage

We consider the same two-dimensional domain as the one depicted in Chapter 2, reproduced below. The dimensions of the computational domain are taken to be much smaller than in real conditions:

$$L_x = 40m, \qquad L_y = 1.2m, \qquad l_y = 0.8m, \qquad a = 0.4m, \qquad x_a = 10m, \qquad x_b = 20m, \quad (3.6)$$

so that our numerical model can be thought of as a simulation of the flow in a laboratory experiment at a reduced scale (about 10 times smaller than the real flow domain). The Reynolds number is still very large (a few 10^5), so that very fine meshing will be required to make sure that the near wall treatment is accurate enough.

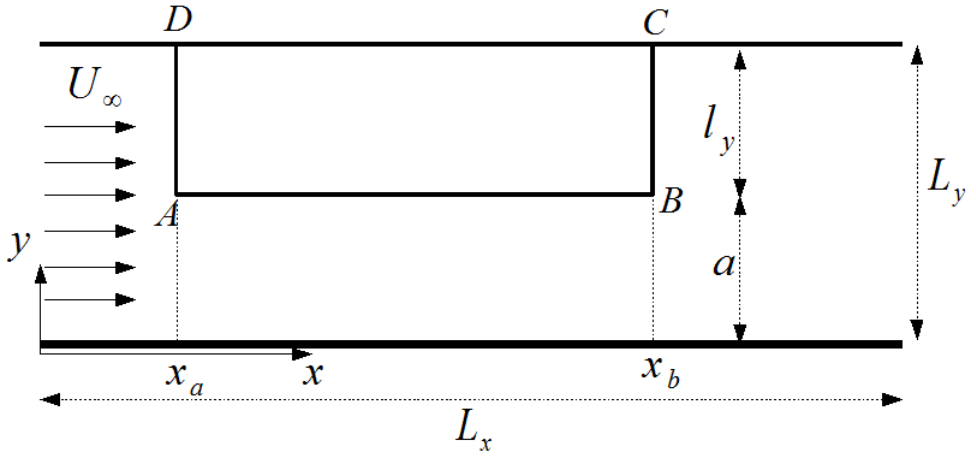

Figure 3.2: *Sketch of the computational domain and of the rectangular cage ABCD in the vertical plane.*

The Reynolds equations (3.2)-(3.3), or equivalently (2.6)-(2.7), have been discussed in details in Chapter 2 and at the beginning of the present chapter. They are solved using a finite-volume method (Fluent), with User Defined Functions to implement the C_{net} terms. It is assumed that the mean flow is steady. The corresponding boundary conditions, which are of great importance for the validity of the computation, are discussed in the next section.

3.3.1 Boundary conditions

Inlet and outlet conditions. To ensure a smooth velocity profile at the inlet, velocity at $x = 0$ has been taken to be an empirical power-law function of the form:

$$u_{in}(y) \equiv u(0, y) = \frac{9}{8} U_\infty \left(\frac{y}{L_y} \right)^{1/8} \tag{3.7}$$

which has been normalized to have $U_\infty L_y = \int_0^{L_y} u_{in}(y)\, dy$. The upstream velocity recorded in the roadstead of Cherbourg ranges from $0.1\, m.s^{-1}$ up to $1.5\, m.s^{-1}$. The averaged velocity of the mean flow has been chosen as $U_\infty = 0.5\, m.s^{-1}$ in the following simulations. The *outflow* boundary condition has been set at the outlet of the calculating domain.

Turbulence at the inlet. The turbulent intensity I at the inlet is taken to lie in the range $1\% < I < 5\%$, which corresponds to the case of common turbulence conditions with moderate intensity.

Near-wall treatment and meshing. At the bottom wall $y = 0$, the no-slip boundary condition has been set in our calculations. Standard wall functions are used, so that the so-called 'log-law' describes the turbulent boundary layer. The non-dimensional wall distance y^+ ranges from about 30 to 60, as required for the use of such wall functions.

Upper surface. Finally, to approach real conditions, the surface $y = L_y$ has been set as a free-slip boundary condition to account for the negligible viscous stress exerted by air on water. Note that this interface is frozen (i.e. it does not deform), as the theoretical model has shown that the deformation of the air/water interface due to the drop of piezometric pressure is negligible here (see Eq. (2.41) page 32).

3.4 Simulation results for a cage at laboratory scale

3.4.1 Pressure drop

The following figures show the drop of piezometric pressure for various drag coefficients C_{net} ranging from of a few units to a few hundreds. Again, the pressure is plotted for various horizontal lines from the bottom ($y = 0$) to the surface ($y = L_y$).

In the case of moderate effective drag coefficients (C_{net} of a few units), pressure along horizontal planes all collapse on the same curve (Fig. 3.3), and this confirms that $\widehat{P}$ is independent

of y. These curves also show an abrupt pressure drop due to the presence of the cage, in quantitative agreement with Eq. (2.25). For these values of C_{net}, the asymptotic condition (2.52), that is $C_{net} \ll \left(\frac{\tilde{u}}{U_\infty}\right)\frac{l_x}{\Delta}$, is satisfied, since $\left(\frac{\tilde{u}}{U_\infty}\right)\frac{l_x}{\Delta}$ is about a few tens. As long as this condition, together with Eq. (2.49) are fulfilled, the Prandtl equation (2.55) is expected to be valid.

The table below shows the difference in piezometric pressure $\widehat{P}(x_a) - \widehat{P}(x_b)$ predicted from Eq. (2.40), and obtained from the simulations of Fig. 3.3. We observe that the global behavior is recovered without any ad hoc tuning of parameters, though discrepancies are visible. These discrepancies are due to the fact that the model relies on the assumption that $l_y/l_x \ll 1$, and this ratio is not so small in the numerical computation.

C_{net}	1	2	3	4
$\widehat{P}_a - \widehat{P}_b$ (Eq. (2.40))	76 Pa	136	182	219
$\widehat{P}_a - \widehat{P}_b$ (simulations)	58 Pa	108	153	192
relative error	31 %	26 %	19 %	14 %

Under increasing C_{net} (Fig. 3.4, $C_{net} = 50, 100, 200, 500$), we observe that the horizontal pressure profiles are still independent of y, but the linearity of $\widehat{P}(x)$ (Eq. (2.25)) is no longer satisfied. This means that convective acceleration terms come into play, even outside the mixing layer, and that streamlines becomes much more distorted, especially near the inlet section of the cage $x = x_a$ where the flow is forced to go below the cage. In addition, the asymptotic condition (2.52) page 35 is no longer fulfilled when C_{net} is of a few hundred. For both reasons, we do not expect the asymptotic model to be valid here, as a more complex flow takes place for such "dirty" cages with a low permeability. Finally, Fig. 3.5 shows $\widehat{P}(x)$ for various C_{net}, to highlight the role of the low permeability on the pressure drop.

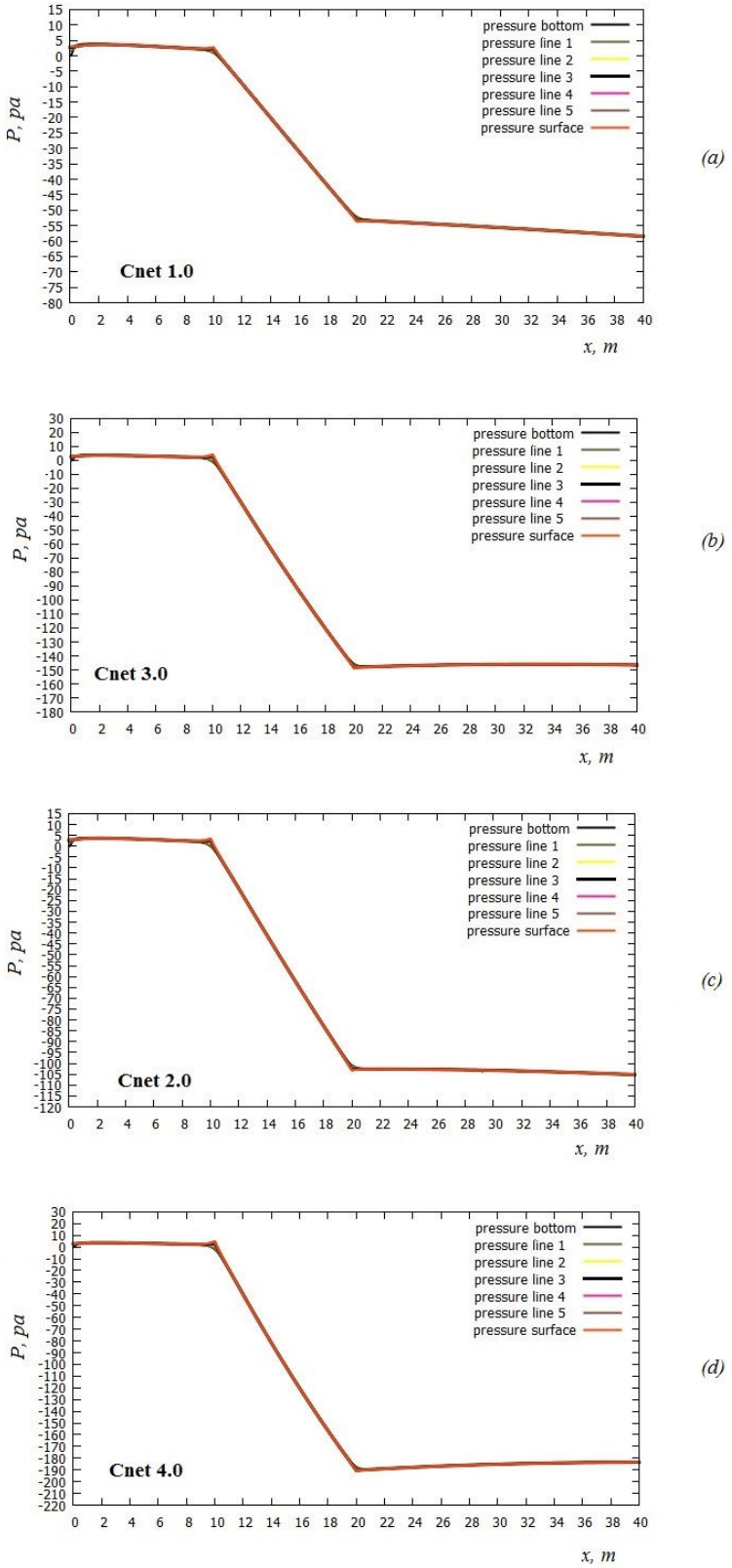

Figure 3.3: *Piezometric ressure drop* $\widehat{P}(x)$*, along various horizontal lines equispaced from the bottom* ($y = 0$) *to the surface* ($y = L_y$)*, in the case of moderate* C_{net}*. Parameters are given by Eqs. (3.6) and (3.7). The cage covers the range* $10\,m = x_a < x < x_b = 20\,m$.

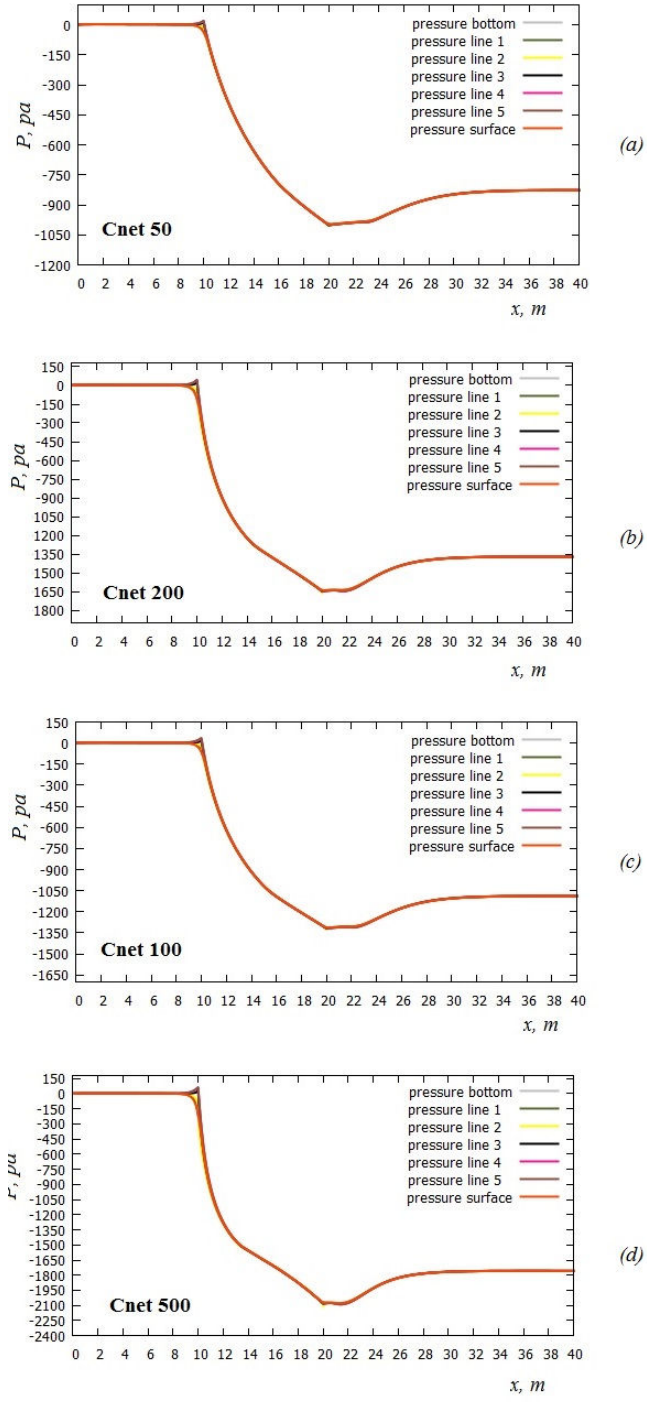

Figure 3.4: *Pressure drop across the computational domain, in the case of large* C_{net}*. Parameters are given by Eqs. (3.6) and (3.7). The cage covers the range* $10\,m = x_a < x < x_b = 20\,m$.

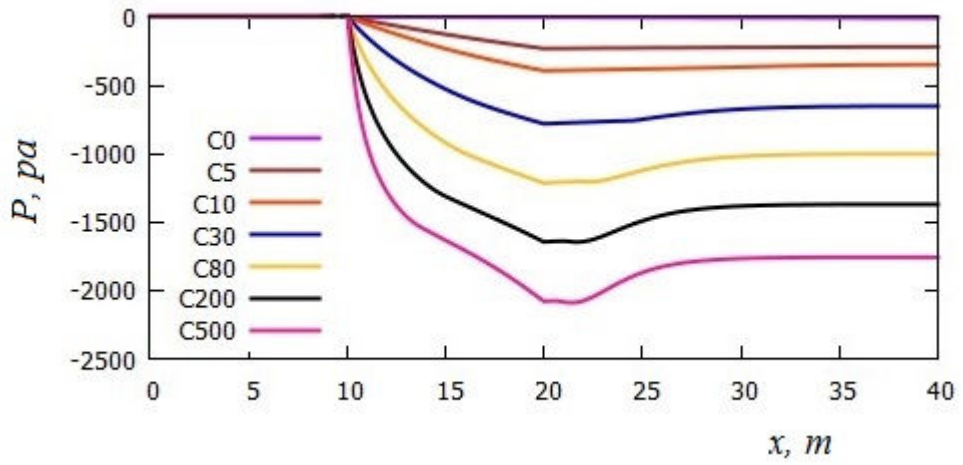

Figure 3.5: *Pressure drop across the computational domain for various values of C_{net} between 0 and 500. Parameters are given by Eqs. (3.6) and (3.7). The cage covers the range* $10\,m = x_a < x < x_b = 20\,m$.

3.4.2 Bottom shear stress

The shear stress $\tau_w = \mu \dfrac{\partial \bar{u}}{\partial y}$ at the bottom of the domain ($y = 0$), where μ is the dynamic viscosity of the fluid, is a quantity of great interest to predict the appearance of erosion and resuspension of materials below the cage. Indeed, as soon as τ_w is known, one can make use of Shield's criterion to estimate whether the motion of particles could be initiated. Resuspension is an important impact of any immersed structure on its environment, especially when permeability is low (see for example Poizot et al. [70]). Figure 3.6 shows the bottom shear stress obtained from numerical simulations (same parameters as above, Eqs. (3.6) and (3.7)): clearly, the presence of the cage has a huge effect of this quantity, as it can significantly increase the bottom shear stress as soon as the effective drag coefficient C_{net} is of a few tens.

3.4.3 Turbulent intensity

The turbulent intensity I is defined as $I = u'/U$, where u' is the root-mean-square (rms) of the turbulent velocity fluctuation and $\bar{u}$ is the mean velocity amplitude:

$$U = \sqrt{(\bar{u})^2 + (\bar{v})^2}. \tag{3.8}$$

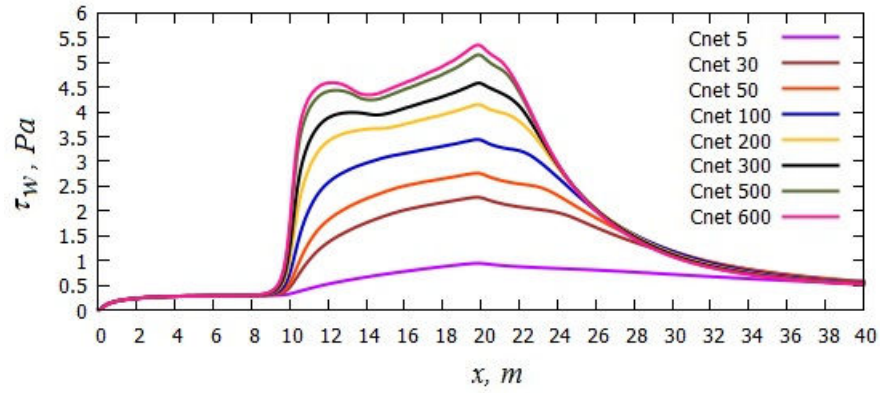

Figure 3.6: *Bottom shear stress τ_w versus x, for various effective drag coefficients of the cage. Parameters are given by Eqs. (3.6) and (3.7). The cage covers the range* $10m = x_a < x < x_b = 20m$.

The rms velocity is also related to the fluctuating kinetic energy k per unit mass (already met in section 3.2) via:

$$k = \frac{3}{2}u'^2.$$

A global view of turbulent intensity, obtained from our numerical simulations, is shown in Fig. 3.7, for various values of C_{net}. As can be seen from this picture, turbulence has a tendency to increase under the cage and downstream of the cage. For small values of C_{net}, the thickness of the turbulent mixing layer increases linearly with x below and behind the cage, and this comforts the choice (2.58) for the normalized x-coordinate of the theoretical model. For larger values of C_{net}, numerical simulations clearly show that this linear growth breaks, and the topology of the turbulent zone is more complex. This is due to the appearance of the recirculation zone, which will be discussed in section 3.4.4.

Figure 3.8 shows the turbulent intensity at moderate C_{net}'s, along the horizontal line $y = a = 0.4\,m$. We clearly observe that the effective drag coefficient has a huge effect on turbulence production, as I growth drastically, and reaches a peak value which increases with C_{net}. The dashed lines corresponds to the theoretical value I_0 obtained from Eq. (2.66) with $q_{uu} = 0.02$ (i.e. smaller than the accepted experimental values). Even though discrepancies are visible, the model gives an acceptable estimate of turbulent intensity due to the turbulent mixing layer.

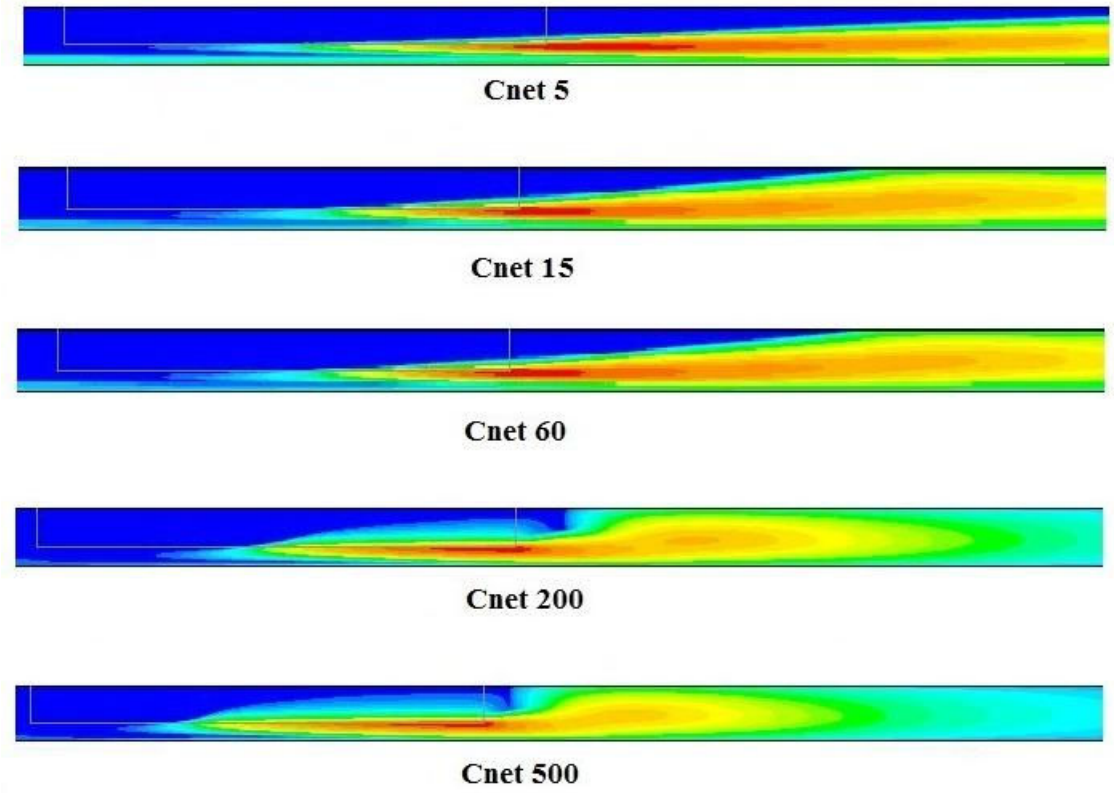

Figure 3.7: *Turbulent intensity for different values of C_{net}. Red: large intensities. Blue: small intensities.*

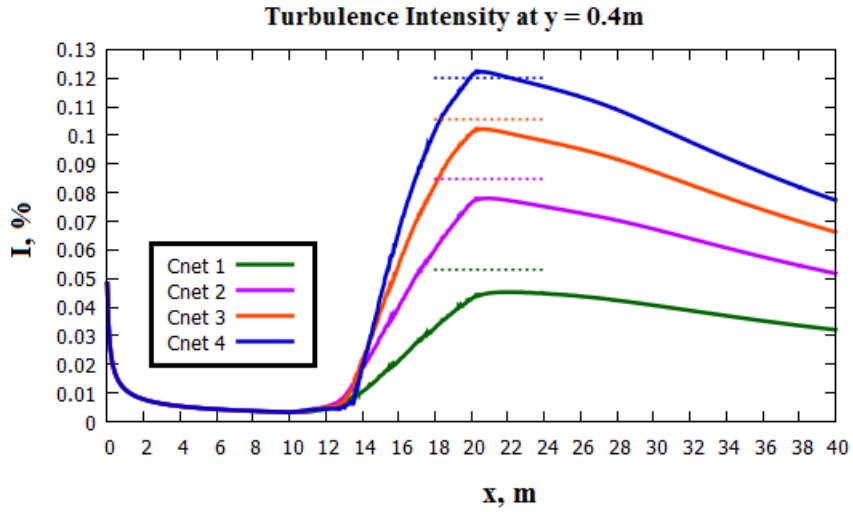

Figure 3.8: *Profiles of turbulent intensity (in per cent) along the horizontal line $y = a$, for $C_{net} = 1, 2, 3$ and 4. Solid lines: numerical simulations. Dashed lines (same color code): theory, Eq. (2.66). The cage goes from $x_a = 10\,m$ to $x_b = 20\,m$.*

3.4.4 Flow structure - Streamlines and extent of the recirculation cell

Figure 3.9 shows the streamlines of the mean flow obtained from our numerical simulation. For small values of C_{net}, streamlines are almost parallel and horizontal. A vertical flow component appears near the inlet of the cage when C_{net} increases. In addition, a recirculation cell is visible at the rear of the cage. Clearly, the typical size of the cell increases with C_{net}. In order to quantify this dependence, we have chosen to define the "cell extent" as the length of the reverse flow zone along the interface (see Fig. 3.10 (upper graph)):

$$\mathcal{L} = |CS|.$$

In terms of the upper horizontal velocity component $u(x, L_y)$ (obtained from our simulations), the cell extent has a simple expression:

$$\mathcal{L} = \frac{1}{2}\left[x_E - x_C - \int_C^E sign(u(x, L_y))dx\right] \tag{3.9}$$

Indeed, in the absence of cell we have $u(x, L_y) > 0$ for all $x \in [x_C, x_E]$, so that $\mathcal{L} = 0$. When a cell is present, with a reattachment point S, we have:

$$\mathcal{L} = \frac{1}{2}\left[x_E - x_C + x_S - x_C - (x_E - x_S)\right] = x_S - x_C.$$

Figure 3.10 (lower graph) shows the cell extent $\mathcal{L}$ versus C_{net}. We observe that $\mathcal{L}$ remains equal to 0 for all C_{net} below 15. Then, $\mathcal{L}$ takes positive values and increases abruptly. This confirms that there exists a critical value of C_{net} where a bifurcation occurs, and the topology of the flow changes. We are aware of the fact that boundary layer detachment, which is a key mechanism for the occurrence of recirculation cells, is very difficult to recover with a CFD code, i.e. it requires to use very fine meshes and very efficient turbulence models. By changing either the turbulence model or the near-wall treatment, one might obtain different values for the critical C_{net}. However, the overall behaviour might not be too different and bifurcations will occur, whatever the details of the numerical method.

For larger values of C_{net}, the cell extent converges to a constant value of about 5 m. We have checked that this limiting value is independent of the horizontal dimension L_x of the computational domain, provided the outlet is far enough from the net.

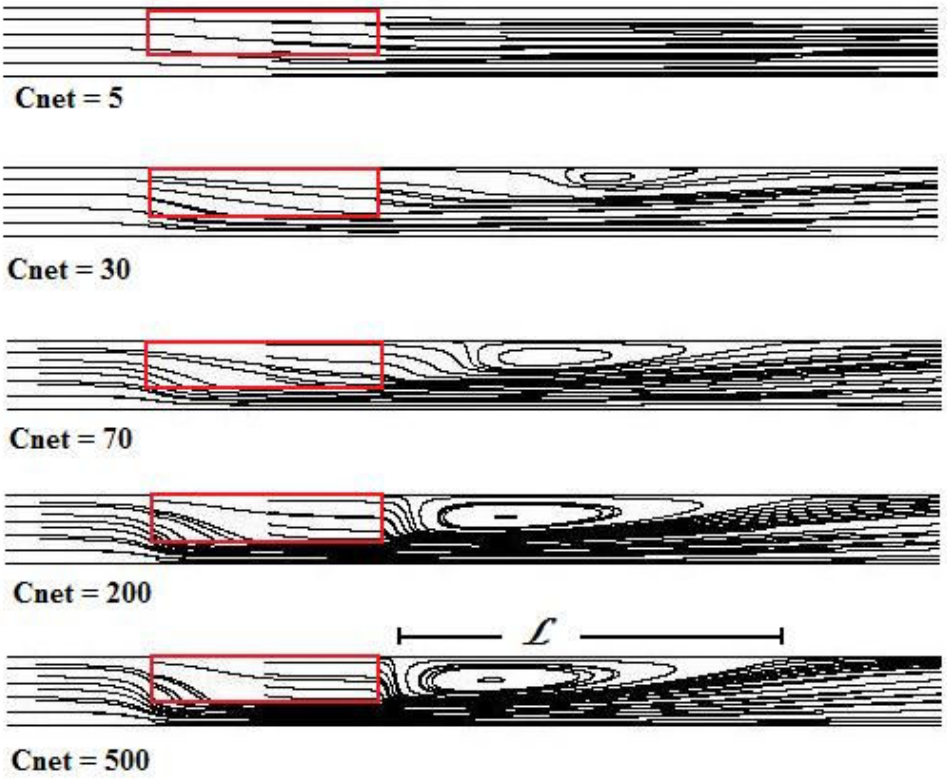

Figure 3.9: *Streamlines of the mean flow for various finite values of* C_{net}.

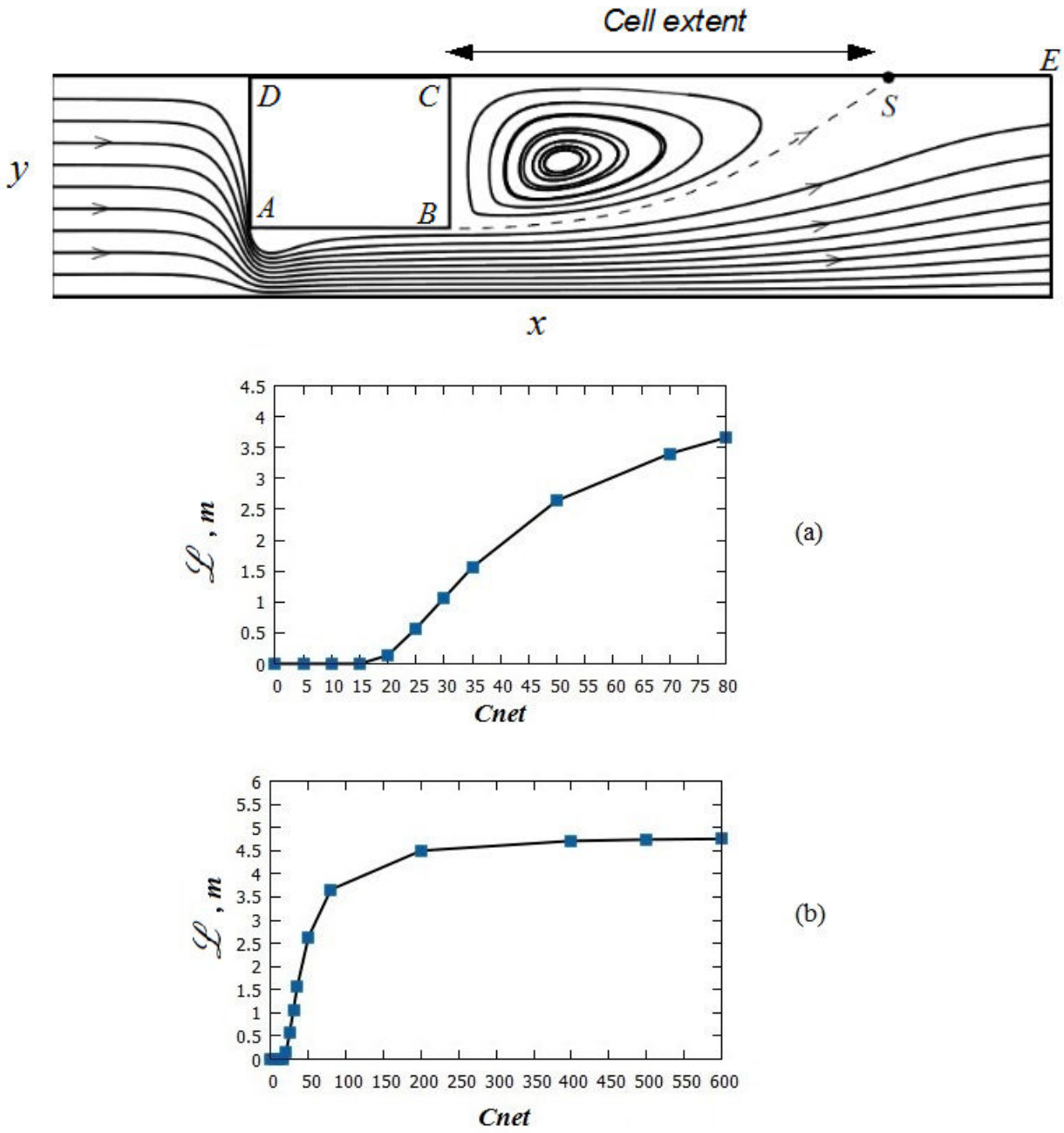

Figure 3.10: *Upper graph: mean streamlines when* $C_{net} = \infty$. *The "cell extent"* $\mathcal{L}$ *is defined as the length of the reverse flow zone along the interface, that is* $\mathcal{L} = |CS|$. *Graphs (a) and (b): plot of the cell extent* $\mathcal{L}$ *versus* C_{net}.

3.4.5 Flow reduction within the cage

As discussed in the first chapter, many experimental studies about fishnets have shown that a significant reduction of the flow could happen inside the cages [30][56][52][49][36][55]. According to the conditions of these measurements (shape and size of the cages, intensity of biofouling, fish concentration, upstream flow, etc.), the percentage of velocity reduction can take very different values ranging between 10 % and 80 %. In this section, we aim at proposing a simple model for the link between the effective drag coefficient of the cage C_{net} and the relative flow rate passing through the cage. For that, we define the flow rate, per unit width through the net, as the flux of velocity through the exit of the net (in units of $m^3.s^{-1}.m^{-1}$):

$$Q_{net} = \int_a^{L_y} u(x_b, y)dy. \tag{3.10}$$

The total flow rate is:

$$Q_{total} = \int_0^{L_y} u(x_b, y)dy = U_\infty L_y. \tag{3.11}$$

The relative flow rate through the rear end of the cage Q_i is defined as:

$$Q_i = \frac{Q_{net}}{Q_{total}} \tag{3.12}$$

and is plotted in Fig. 3.11. We observe that Q_i is below 10 % when C_{net} is above 500: such cages can be considered as nearly impermeable. The same curve in log-log plot for $5 \leq C_{net} \leq 500$ shows a nearly linear decay, and this strongly suggest a power-law of the form:

$$Q_i \simeq \alpha\, C_{net}^{-\beta} \tag{3.13}$$

with $\alpha \simeq 0.8$ and $\beta \simeq 0.3$, and C_{net} larger than 5. The dashed line of the upper graph of Fig. 3.11 confirms that Eq. (3.13) is a good approximation.

As stated in Chapter 2, the theoretical model is expected to give satisfactory results for C_{net} of order unity. In this case, Eq. (2.32) page 31 leads to[2]:

$$Q_i \simeq \frac{u_0(C_{net})\, l_y}{U_\infty\, L_y} = \frac{\sqrt{B^2 - AC} - B}{A}\, \frac{1}{1 + a/l_y}, \tag{3.14}$$

[2]Here we assume that the flow rate at the rear end of the net $x = x_b$ is $u_0 l_y$, i.e. that the flow is uniform here. We could also integrate the erf profile (2.59) from $y = a$ to $y = L_y$, to account for the velocity inside the mixing layer, but this would bring minor corrections.

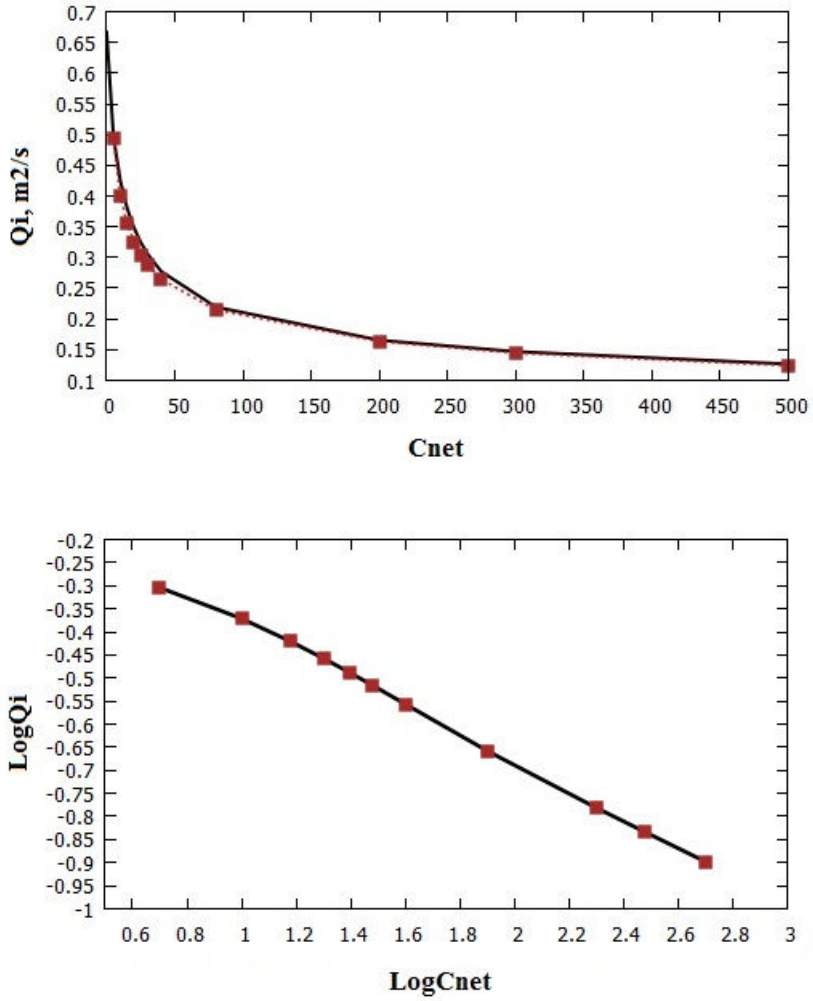

Figure 3.11: *Relative flow rate Q_i through the rear end of the cage versus C_{net}, in lin-lin plot (upper graph) and in log-log plot (lower graph).*

where the non-dimensional functions $A(C_{net}, l_y/a)$, $B(C_{net}, l_y/a)$ and $C(C_{net}, l_y/a)$, have been given in Eqs. (2.35)-(2.37). We have checked that this formula agrees with our numerical results. For example, when $C_{net} = 5$, Eq. (3.14) leads to $Q_i \approx 42\%$, in agreement with our numerical result shown in Fig. 3.11. For very small C_{net}'s, the theoretical model leads to the trivial result $Q_i \simeq l_y/L_y \simeq 0.66$, as the velocity is nearly uniform here (except near the bottom boundary layer). This result is recovered in our numerical computations (see first point in Fig. 3.11).

Finally, to give an idea of velocity reduction for large C_{net}'s we have plotted the horizontal velocity $\bar{u}(x, y_0)$ versus x, along a fixed horizontal line of height $y_0 = 3L_y/4$ crossing the cage, and for various C_{net}'s (Fig. 3.12). We observe that velocity at the end of the cage is divided by about 5 when C_{net} is above 200. This reduction then seems to be less sensitive to C_{net} for even larger C_{net}'s.

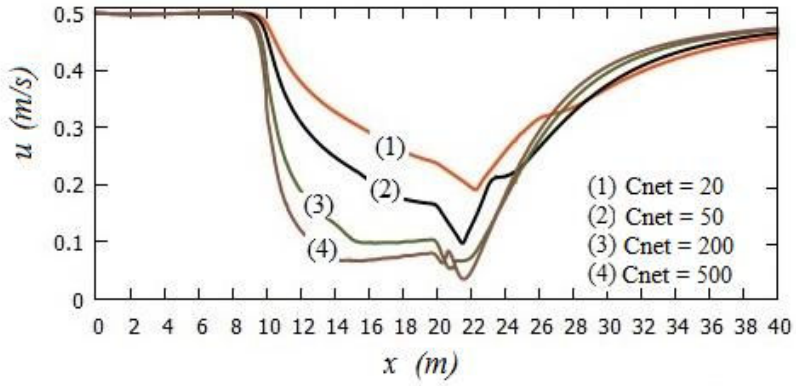

Figure 3.12: *Horizontal velocity $\bar{u}(x, y_0)$ versus x, along a fixed horizontal line of height $y_0 = 3L_y/4$ crossing the cage.*

3.5 Conclusion of this chapter

The analytical model presented in the previous chapter helped us design a numerical model for the flow in the vertical plane. The main advantage of these simulations is that they generalize the theoretical approach to less permeable cages, since they allow to consider not only moderate, but also large values of C_{net}. However, they still rely on a large number of approximations (2D domain, fixed rectangular cage, moderate dimensions, absence of waves, etc.) and cannot be considered as extremely realistic. Nevertheless, they bring some interesting information about

the hydrodynamics, which are listed below.

Pressure drop. Piezometric pressure drop along the stream is an interesting effect that has been captured by our model. It is due to the presence of the cage which creates a drag. Even though this drag acts inside the cage only, the longitudinal piezometric pressure gradient exists also *below* the cage, where the fluid velocity increases with x. In particular, the boundary layer at the bottom wall has a *favourable pressure gradient*: this effect will be taken into account in further studies.

Bottom shear stress. The acceleration of the flow below the cage increases the bottom shear stress. In the case of our cage at laboratory scale (depth = 1.2 m, cage length = 10 m, total length = 40 m), and with an inlet velocity of 0.5 $m.s^{-1}$, the bottom shear stress can reach values of a few Pa. Such stresses could have en effect on the sand bed below. This point will be discussed in Chapter 5.

Streamlines and flow structure. For small or moderate C_{net}'s, streamlines are nearly parallel, i.e. the flow is mostly towards x at each point of the computational domain, even at the rear of the cage. No recirculation cell exists, and the cell-extent $\mathcal{L}$ is perfectly equal to zero for all C_{net} below 15. Clearly, this critical value depends on the geometry of the domain and on the upstream velocity. Then, a bifurcation occurs, a recirculation cell appears at the rear of the cage, and $\mathcal{L}$ increases abruptly with C_{net}, and reaches an asymptotic value of about 5 m (Fig. 3.10). When the cell appears, the flow rate through the cage drops. This effect is expected to be of major importance for sediment transport (that will be studied in Chapter 5): when the recirculation cell reaches its limiting extent, the cage is "hydrodynamically blocked" and all effluents produced by fishes will exit the cage *from below*, instead of being driven away by the main stream.

The recirculation cell has an additional effect (studied in details by Poizot et al. [70]): suspended particles traveling below the cage and passing near the "separatrix" streamline BS (see upper graph of Fig. 3.10) are likely to be trapped by the recirculation cell. This trapping phenomenon has been observed in many different situations, as soon as separatrices exist in a flow. In this case, they spend a long time spinning inside the cell and can be driven back towards the border of the cage. Effluents transported this way create a so called "self-contamination" of the cage [70]). This effect will be discussed in more details in Chapter 5.

Flow reduction within the cage. The flow rate within the cage decreases when the effective drag coefficient increases. For the parameters considered here, and for large C_{net}'s, simulations clearly suggest that the relative flow rate through the cage Q_i obeys a power-law of the form of Eq. (3.13). For $C_{net} > 500$, the relative flow rate is below 10 %, so that the cage is nearly impermeable. The parameters α and β appearing in this power-law certainly depend on the geometry of the problem (size of the cages, etc.) but this question requires to be investigated in details.

Chapter 4

In-situ flow measurements

After having performed theoretical and numerical analyses of the flow around a simplified model of immersed obstacle, we now turn to real fish farms. This chapter is devoted to flow measurements carried out during the thesis at the aquaculture fish farm of Cherbourg, which has been mentioned several times in the previous chapters. We first introduce flow measurements using current meters located at positions of interest. These results will then be commented and compared with analytical and numerical calculations described above.

4.1 Area under study and positions of current meters

Fig. 4.1 shows the study area located in the roadstead of Cherbourg. The aquaculture fish farm covers an area of around 17 hectares (photographs of Figs. 4.2 and 4.3). This farm consists of cylindrical and cubic nets. The average height of the nets lies between 7 and 8 metres below the sea surface, and the distance from their bottom to the seabed ranges from 3 to 7 metres, according to the deformation of the fishnet cage and to the sea level variations due to the tides. In the numerical and analytical parts of the present thesis, the deformation of the net was omitted. Thus, we don't expect our models to accurately agree with measurements.

Flow velocities have been measured at various positions around and inside the fish farm. For reasons of cost and convenience, only 3 positions were chosen to set our current meters. A Seaguard current meter was located inside one of the fishnet cages and two ADCP's were

positioned upstream and downstream of the fishnet cage system. The three instruments were positioned as follows (Fig. 4.4):

- the ***Seaguard current meter*** (Seaguard Andera) was set at the right corner of the last fish net cage,
- the ***IRSN ADCP*** (Teledyne RDI Sentinel V50) was installed 20 meters beyond the cage, on the East side,
- the ***Intechmer ADCP*** (Teledyne RDI Sentinel S50) was set 50 meters beyond the cage, on the West side.

For safety and technical reasons, we could not install a device below the cages (as initially planned), which is a zone of great interest that has received little attention so far. Therefore, we have limited our study to the comparison between velocities in front of and behind the cage. Positions of the three current meters (the Intechmer ADCP, the IRSN ADCP, the Seaguard current meter) are illustrated in Fig. 4.4.

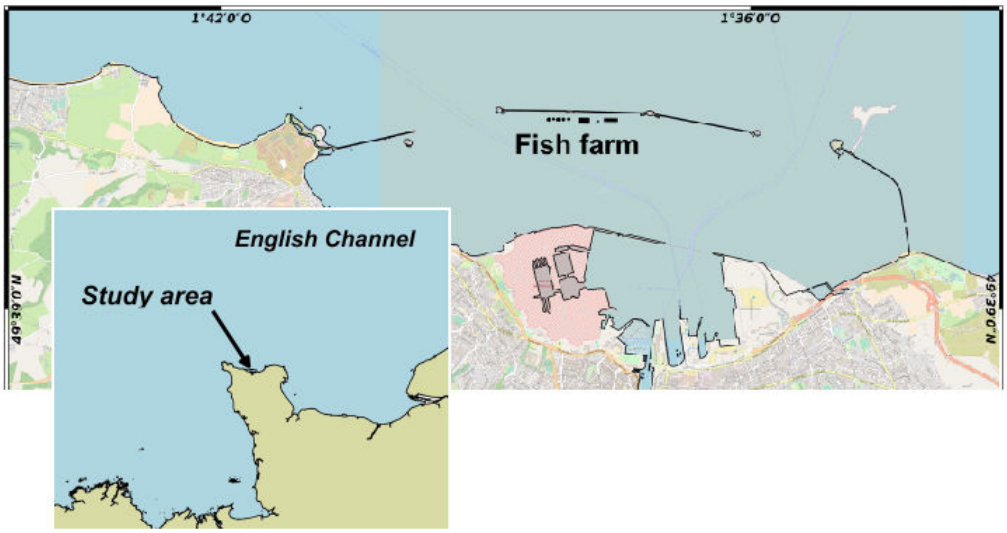

Figure 4.1: *Map of the Cherbourg roadstead showing the aquaculture fish farm.*

Figure 4.5 zooms on the locations of the three measuring instruments, installed in October 2016. Due to technical limitations and external circumstances, data recorded from the Seaguard Andera were unreliable and had to be discarded. As a consequence, velocity measurements *inside* the fishnet are unavailable. Measurements were performed during 18 days for the S50

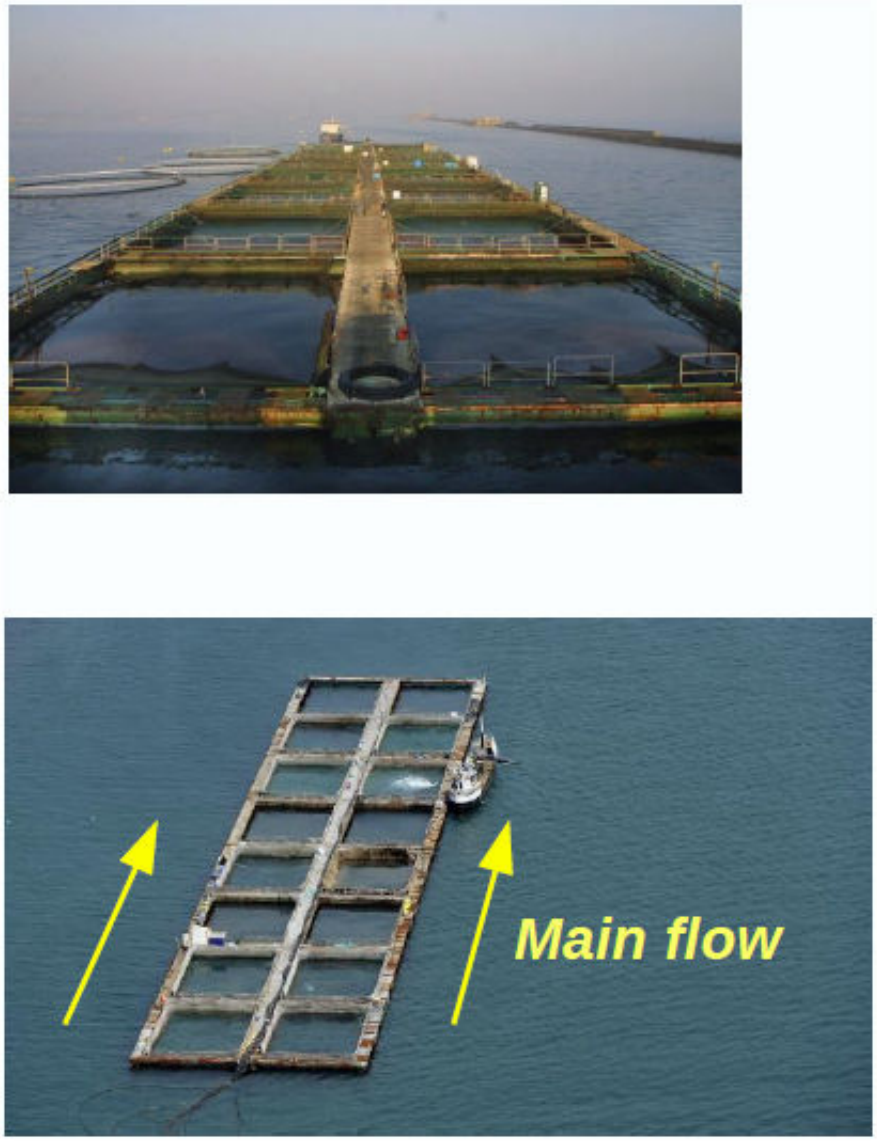

Figure 4.2: *Photographs of the fish farm.*

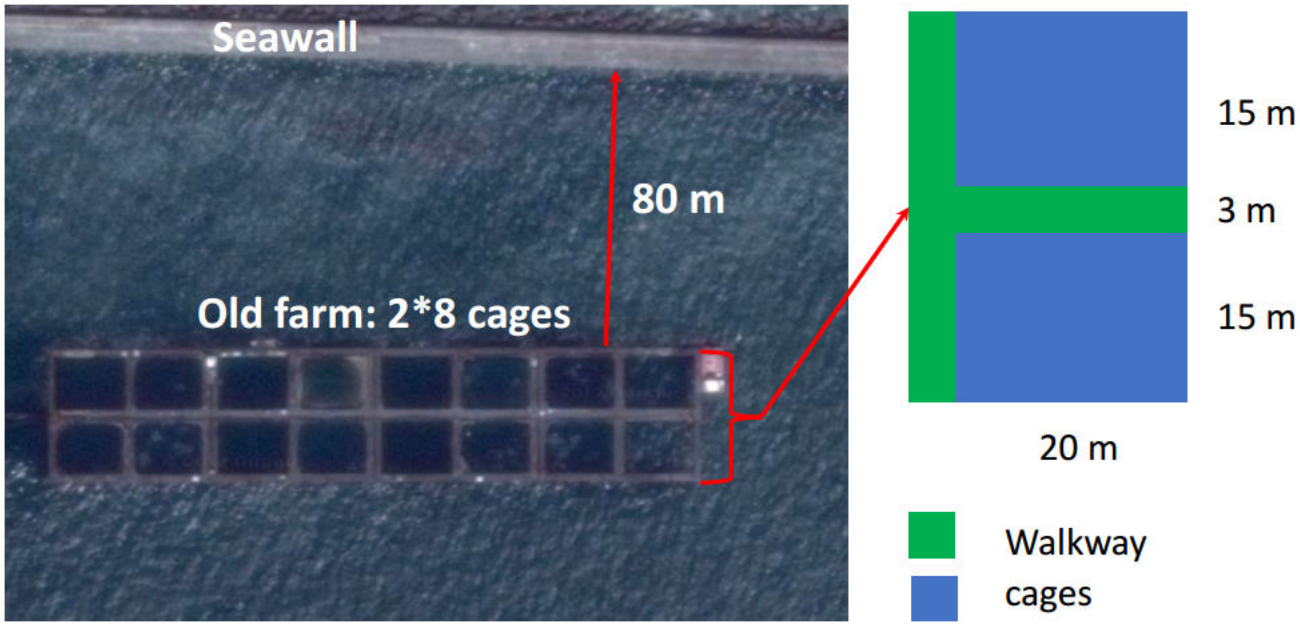

Figure 4.3: *Photograph of the fish farm (top view). The whole set of 16 cages covers a rectangular domain* $160\,m \times 33\,m$.

ADCP (from 10/06/2016 to 10/24/2016) and 16 days for the V50 ADCP (from 10/06/2016 to 10/22/2016), because this current meter ran out of battery sooner than scheduled. Both devices operated on the same firmware with the same version (47.17.0.22) and were set up with the same configuration, to ensure that they produce comparable data. Data were permanently collected during this time.

4.2 General considerations about ADCP measurements

In this section, we introduce some common knowledge about ADCP's, how they work and how to use them efficiently in combination with the Teledyne RDI Sentinel V50 software. Readers familiar with ADCP techniques may skip this part.

An ADCP is defined as a hydro-acoustic current meter, designed to measure water current velocities over a certain range of depth, and based on the Doppler effect of sound waves scattered back from particles within the water column. They can be considered as a device with multiple current-meters monitoring the velocity vertically. These equipment could be utilized in different ways and for different purposes depending on specific measurement requirements and conditions.

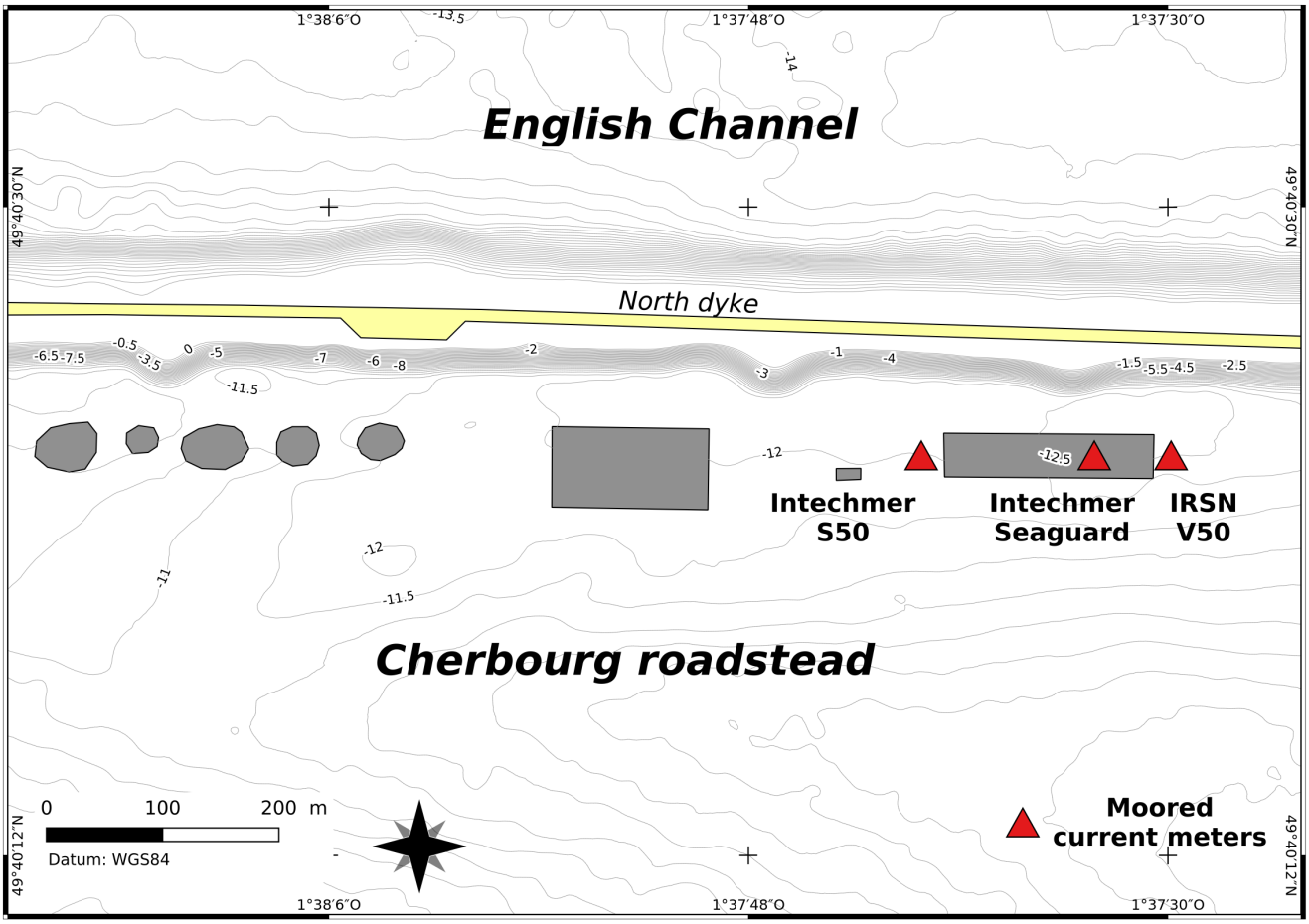

Figure 4.4: *Setting positions of the three current meters: the Intechmer ADCP (RDI Sentinel S50), the IRSN ADCP (RDI Sentinel V50), the Seaguard Andera current meter.*

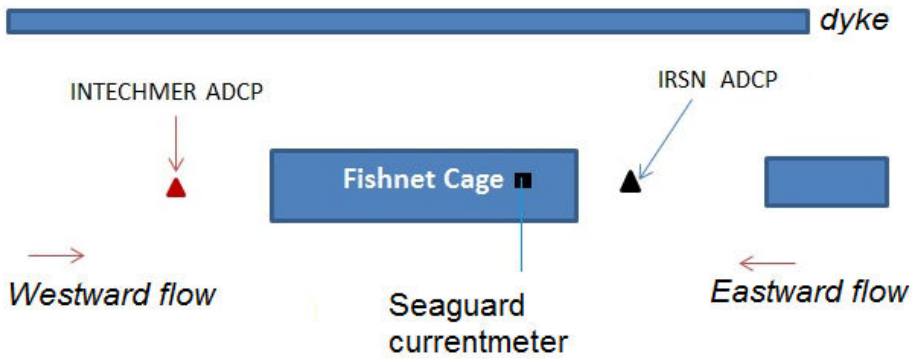

Figure 4.5: *Zoom on the locations of current meters. The scale is given by the length of the fishnet cage which is about 160 m.*

4.2.1 Velocity measurements using the Doppler effect

The Doppler effect is the change in frequency, or equivalently in wavelength, of a waver (or any other periodic event) for a moving observer. This effect can be met whenever a source of waves moves with respect to an observer. Compared to the emitted frequency, the frequency of the measured wave is higher during the approach and lower during the recession. The Doppler shift is defined as the difference between the recorded frequency when one stands still and the recorded frequency when one moves. One should bear in mind that the effect does not result from an actual change in the frequency of the source.

To transmit and receive sound signals, ADCP's make use of piezoelectric transducers which transmit sound impulses at a constant frequency f_s into the water. In practice, this frequency ranges from 38 kHz to several MHz. This basal range of frequency is highly pitched, so that it is out of reach of dolphins and toothed whales. Along their path, sound waves are affected and scattered by suspended particles, and reflect back towards the instrument. If particles move away from the instrument, the recorded frequency f_D of reflected waves will be slightly smaller than their original frequency f_s. In contrast, if particles move towards the current meter, waves with a higher frequency will be sent back. The instrument uses the difference in frequency between the waves it sends and the waves it receives (the so-called Doppler shift) to calculate how fast the suspended particles are moving. Sound waves that hit particles far away from the profiler request longer time to come back than waves that strike particles in the vicinity of the profiler. The profiler manages to measure current speed at various depths from each series of impulses, by calculating the Doppler shift and the time it takes for the waves to bounce back. The relation between the Doppler shifted frequency f_D and the source frequency f_s is expressed as:

$$f_D = 2f_s \frac{V}{c} \tag{4.1}$$

where c is the speed of sound in water (about 1500 $m.s^{-1}$), V is the velocity of the back-scatterer (i.e. the particles suspended in water). The factor 2 appearing in this equation manifests the fact that an ADCP both emits and receives sound. Indeed, the Doppler effect occurs twice: a first effect along the path from the transducer to the scatterer, and a second effect from the scatterer to the transducer.

However, Doppler shift happens only when the distance between the source and the receiver

changes. Indeed, if a scatterer moves perpendicular to the acoustic beam, the distance between the ADCP transducer remains unchanged, then the Doppler shift does not occur. Thus, the deflection of the velocity vector of the targeted scatterer from the acoustic beam axis of the ACDP should be accounted for as:

$$f_D = 2f_s \frac{V}{c} \cos(\theta) \tag{4.2}$$

where θ is the angle between the ADCP beam and the velocity vector of the scatterer (see Fig. 4.6). The velocity of the scatterer measured by the ADCP can therefore be calculated as:

$$V = c\frac{f_D}{2f_s cos(\theta)} \tag{4.3}$$

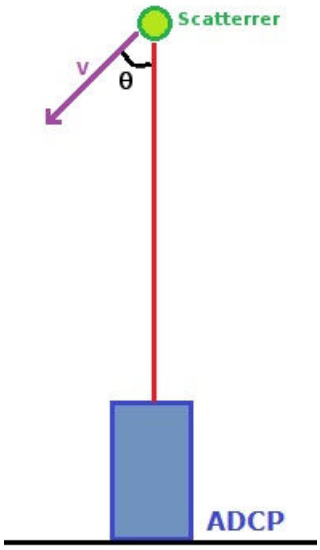

Figure 4.6: *Sketch illustrating the deflection of velocity from the scatterer.*

4.2.2 Benefits and limitations

Benefits:

- ADCP's provide a velocity profile along the water column. They avoid using long strings of current meters, as was frequently done in the past.

- ADCP's can measure velocities along a water column up to 1000 m long.

- ADCP's can measure small scale and low speed currents.

- Unlike previous technologies, ADCP's measure the absolute speed of water, not just how fast one water mass moves with respect to another.

Limitations:

- Recorded data are more accurate when high frequency impulses are used. However, low frequency signals travel further in water. Therefore, scientists have to estimate a reasonable distance within which measurements will be as accurate as possible.

- ADCP's run out of batteries rapidly, so that the duration of measurements has to be estimated a priori.

- To produce reliable data, ADCP's must hit a sufficient amount of suspended particles, so that truthful data are difficult to achieve in clear water regions.

- The device may miscalculate the current in the presence of bubbles in turbulent water or swimming marine life.

- Users should take precautions against plankton, barnacles, algae etc,... that could cling on to the transducers.

4.3 Environmental conditions of the fishnet cages of Cherbourg's roadstead

Measurements took place from mid October 2016 to the beginning of November of the same year. The fish farm is located inside the roadstead, near a seawall (dyke) built in the Nineteenth Century: this wall protects the nets from major swells or waves, as well as from the North wind. However, if wind blows from East or West, waves are generated. Therefore, wind and other meteorological parameters have been considered during our study by means of a weather station (Davis Vantage Pro 2) set at CNAM-Intechmer. This weather station is located 4.8 km southeast of the study area, as shown in the map of Fig. 4.7. These meteorological parameters

are listed below.

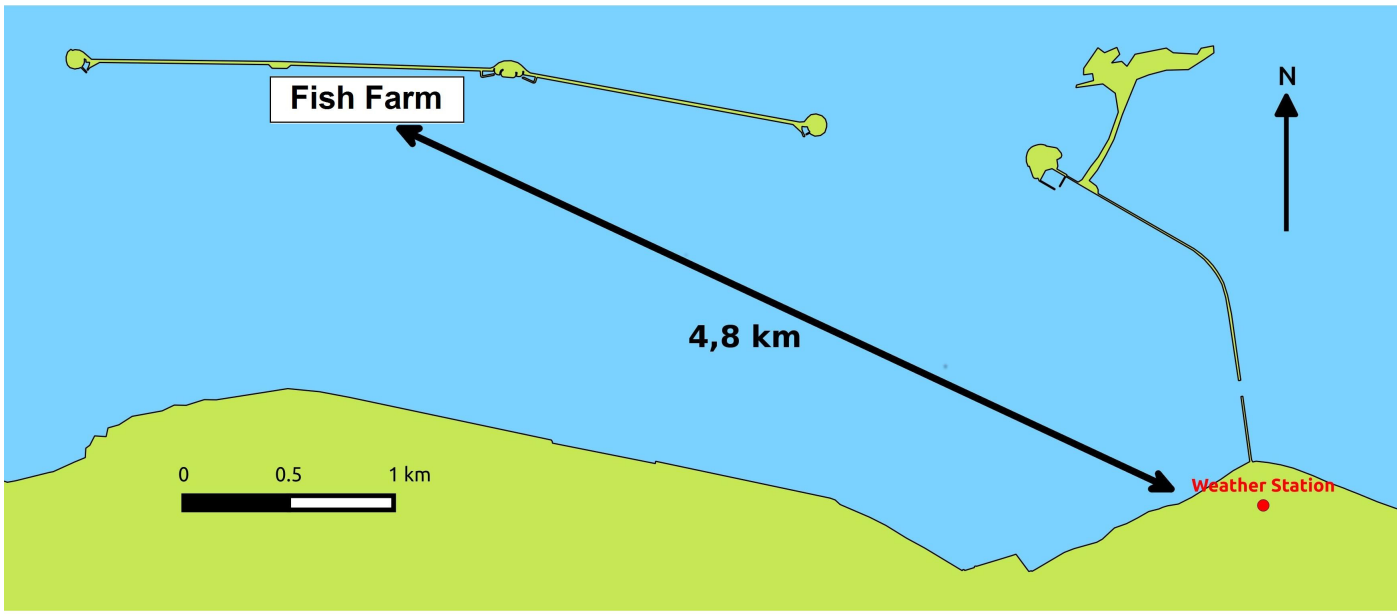

Figure 4.7: *Weather station positioned at CNAM-Intechmer.*

4.3.1 Temperature and rainfall

During the 18 days of measurement, the temperature in the region of interest varied from 11.3 ^{o}C to 14.6 ^{o}C. The cumulative rainfall for this period was 2.1 mm per day, on average. The three highest rainfalls were recorded on October 09th, 15th and 23rd 2016, and were equal to 4.6 mm, 14.4 mm, and 8.9 mm respectively (see Fig. 4.8).

4.3.2 Wind

During the first day, devoted to the deployment of the devices, the mean wind in the region of interest was approximately 17.8 $km.h^{-1}$. Five days later, the wind speed reached its peak of around 25.0 $km.h^{-1}$. The strongest wind lasted during three consecutive days, from October 18th to October 20th. These records allow us to foresee sea surface agitation during certain periods of time. In fact, they must be correlated to the wind direction. Indeed, if wind comes from the North, less surface agitation is expected to happen in comparison with other directions like East or West, which are more aligned with the dyke. In practice, wind from the East

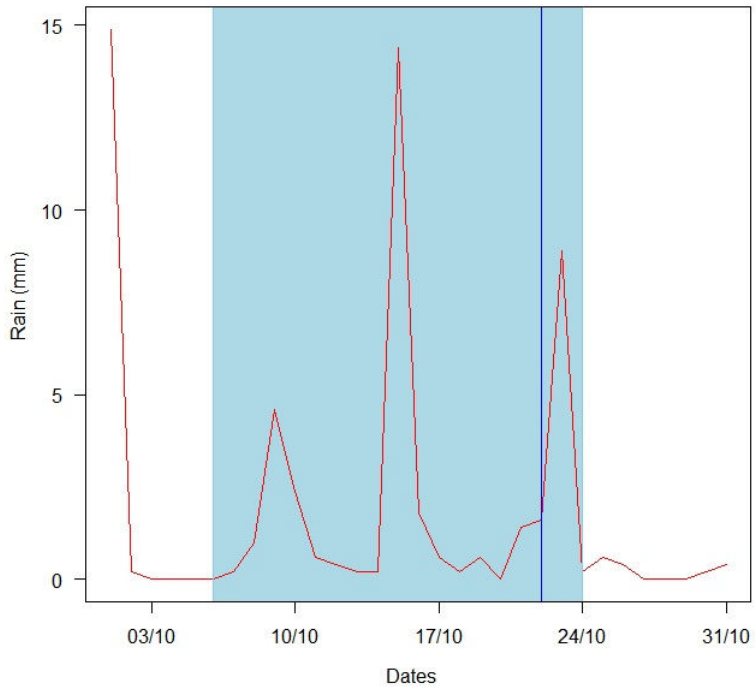

Figure 4.8: *Rainfall recorded during the period of measurements (October 2016).*

occupies more than 50% of time and therefore waves were expected to be mostly induced by the Eastern wind during measurements. Figure 4.9 illustrates the distribution of wind speeds.

4.3.3 Tides

The water depth measured near fish cages varied from 14.0 m to 18.0 m, depending on the tidal height at the time of measurement. The instruments were set up at the beginning of a spring tide cycle in order to capture the strongest and most significant current. Tide variation is shown in Fig. 4.10. As can be seen on this graph, the lowest tide level (corresponding to a tide coefficient equal to 32), was reached on October 10th, 2016, that is four days after the beginning of measurements. The highest tide level, characterized by a tide coefficient of 114, was reached on October 17th, almost in the middle of the measurement period.

4.3.4 Atmospheric pressure

Figure 4.11 shows the mean variation of atmospheric pressure during measurements, enclosed in the blue area. As illustrated in the graph, the pressure recorded during the measurement period

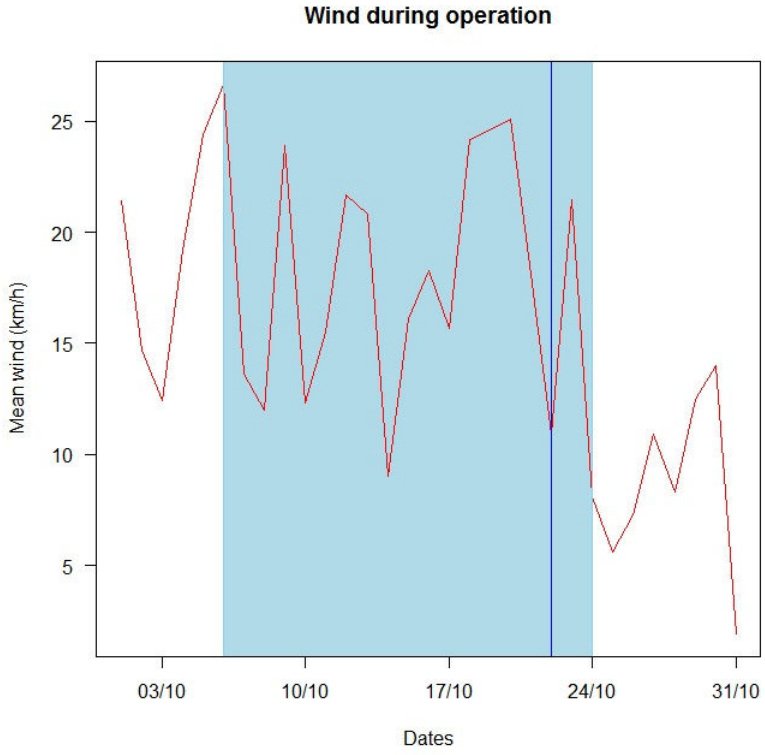

Figure 4.9: *Mean wind speed during measurements (October 2016).*

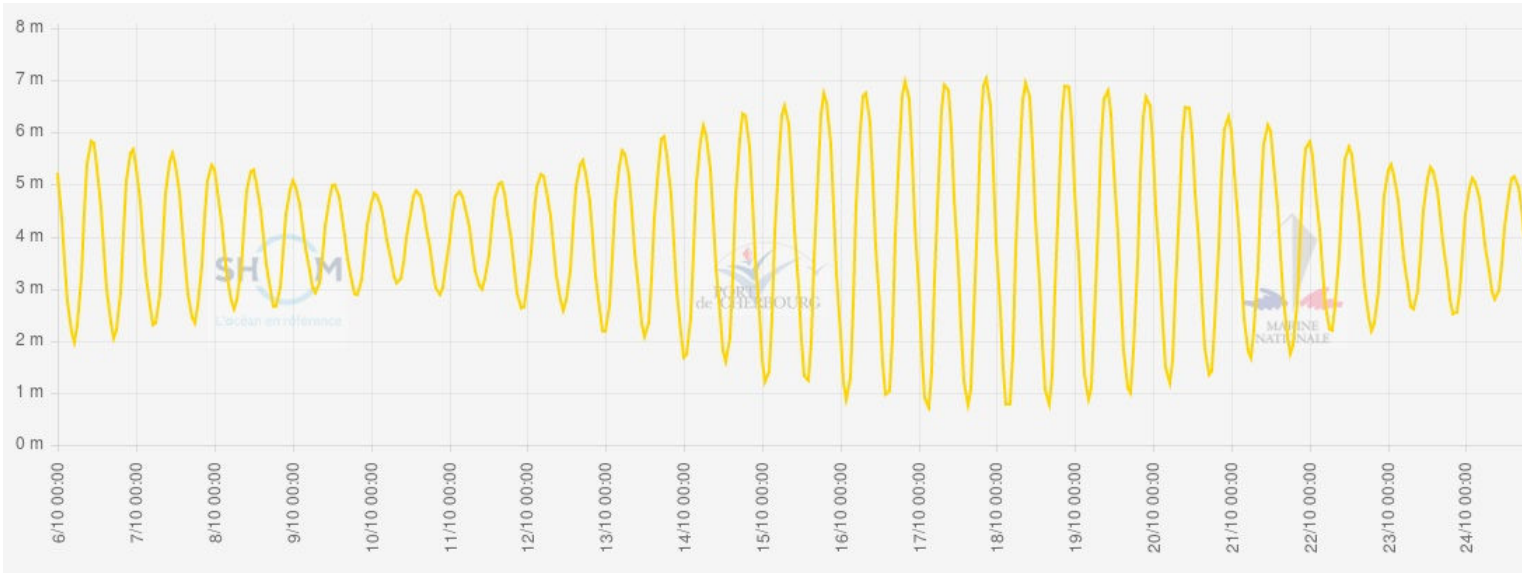

Figure 4.10: *Tidal range during measurements (source: shom.fr).*

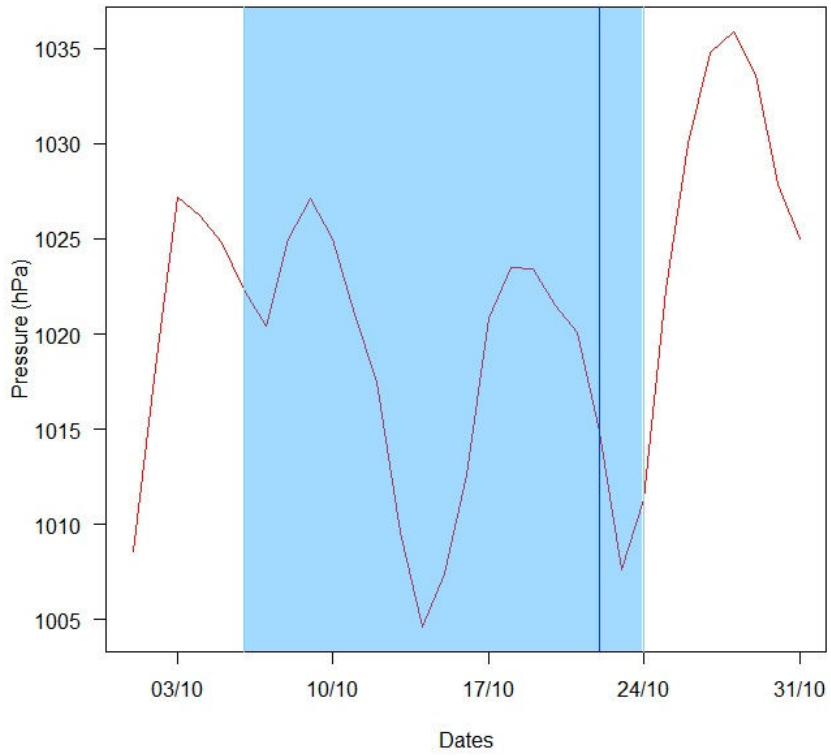

Figure 4.11: *Atmospheric pressure recorded during measurements.*

tends to be anticyclonic. A first peak value of 1027 hPa was reached on October 9th, 2016, and a second peak of 1023 hPa was reached on October 18th. During the period from October 14th to 23rd, the pressure dropped to values around 1005 hPa and 1010 hPa.

4.4 Instruments deployment

As indicated above, the IRSN ADCP (Teledyne RDI Sentinel V50) was set to the East and the Intechmer ADCP (Teledyne RDI Sentinel S50) was positioned on the West side of the fishnet cage. They are fixed on the seabed, as illustrated in Fig. 4.12. The devices were moored using bottom tripods (see photograph in Fig. 4.13), and mounted by professional divers to ensure that the foundation on the seabed was stable and horizontal.

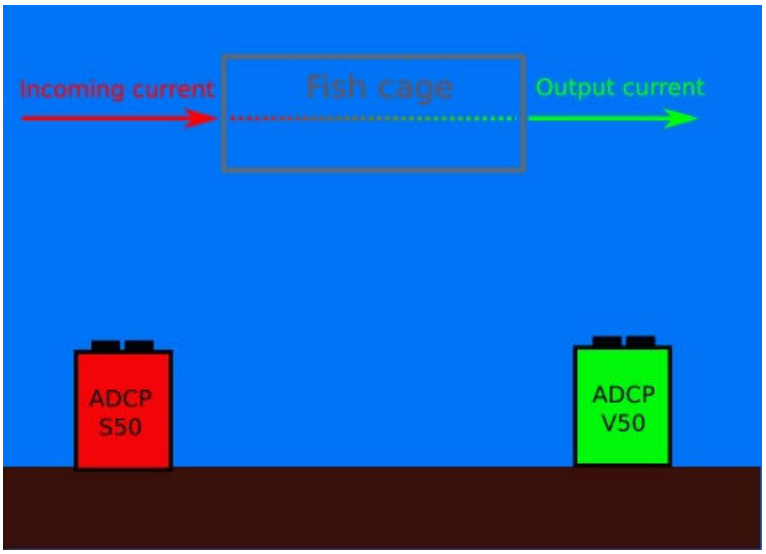

Figure 4.12: *Sketch showing ADCP's installed on the seabed, on the West (Intechmer ADCP S50) and East (IRSN ADCP V50) sides of the cage. (Diagram not to scale.)*

The two ADCP's measured the same height of water column, ran the same firmware, and were configured for the same depth-cell size. They did not have the same battery life, but this didn't affect the study. Each device recorded vertical velocities along the water column, in front of and behind the fishnet cage respectively. They were both activated and started recording on October 10th at 3:00 PM. The IRSN ADCP stopped functioning on October 22th at 12:51:02 PM and the Intechmer ADCP on October 24th at 10:16:11 AM. Technical properties of ADCP's

Figure 4.13: *An ADCP fixed on its tripod during the measurements campaign (October 2016).*

corresponding to these measurements are written in the table of Fig. 4.14.

	Sentinel S50	Sentinel V50
Deployment	10/06/2016 3:00:00 PM	
Last record	10/24/2016 10:16:11 AM	10/22/2016 12:51:02 PM
Frequency	491 kHz	
Beam angle	25°	
Beam count	5	
Start temperature	17,24°C	
Firmware version	47.17.0.22	
Salinity	35 psu	
Cell Size	0,5 m	
Number of cells	22	
Blank	1 m	
Bandwidth	25%	
Lag	0,25 m	
Transmit	0,57 m	
First cell range	1,68 m	

Figure 4.14: *Technical properties of both ADCP's during measurements. (Intechmer ADCP S50 and IRSN ADCP V50.)*

Although ADCP's were fixed on the seabed, they could not measure the current speed along the whole water column, due to the blind zone of the instruments. As illustrated in Fig. 4.15, this blind zone is composed of a 0.8 m height due to the frame itself, plus an extra limitation of 1.68 m due to the measurement device. Thus, both ADCP's could not measure velocities within a bottom layer of thickness 2.48 m. The green region of Fig. 4.15 indicates the zone where velocity measurements could be performed. Depending on the tide at the time of measurement, the ADCP's could record velocities in the water column up to 14 m or 18 m above the bottom.

Concerning the Broadband ADCP, the depth cell size ranges from 0.12 m for the highest frequencies to 32 m for the lowest. Both ADCP's use 22 cells, with a depth cell size of 0.5 m. Since the depth cell size is equal to the distance between current meters, each ADCP measures a water column of 11 m. The number of depth cells represents the number of current meters,

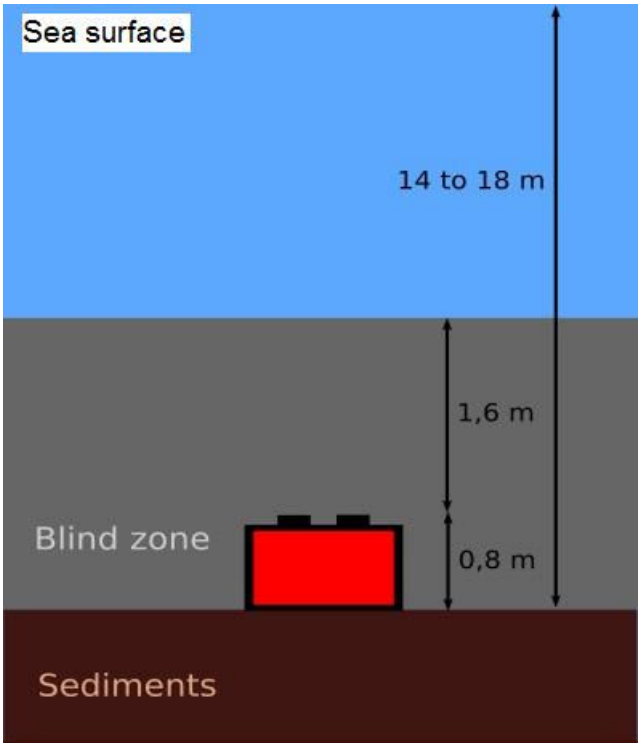

Figure 4.15: *ADCP's blind zone (grey), working zone (blue), sediment bed (brown).*

i.e. each depth cell can be thought of as a single current meter. Hence, our ADCP's contain 22 cells corresponding to 22 current meters placed along a vertical segment of 11 m.

During the period of measurements, the farm was almost perfectly clean. Moreover, it was observed that the fish farm was predominantly occupied by salmons at an early stage, i.e, salmon fry, parr and smolt etc. This implies a negligible fish concentration and a weak contamination of the fishnet cage by bio-fouling. Besides, we also noticed that the outer space of the cage complex was almost free from clinging plankton and phytoplankton or barnacle. This suggests that the flow passing through this obstacle might not meet a significant hydrodynamic resistance due to living organisms. In regard of previous results gained from our theoretical or numerical models, we believe that a small or moderate value of C_{net} should be applied to our problem. This point will be discussed in details below.

After more than two weeks, current meters were pulled out of the water with the help of a diver. They were all in good condition whilst being lifted up on the surface. ADCP data was then processed by a specific software dedicated to these instruments: results are presented in the next

section.

4.5 Data treatment

The post-processing software is highly flexible and allows both automatic and manual configuration, as well as the execution of individual steps. Data produced by a BroadBand ADCP basically includes four different kinds of standard profiles. Velocity data obtained from these ADCP measurements were recorded in earth coordinates format. This means that a velocity measured at a single point and a given time is converted into North, East and up components (corresponding to two horizontal and one vertical coordinates). Also, to reduce the impact of uncertainties on our measurements, data has been averaged over a significant number of samples.

4.5.1 Raw data processing

ADCP's produce raw data files containing different physical parameters measured in the form of various trains of impulses ("pings", see for example Fig. 4.16). These data files have been processed to derive various average quantities of interest for our hydrodynamical problem.

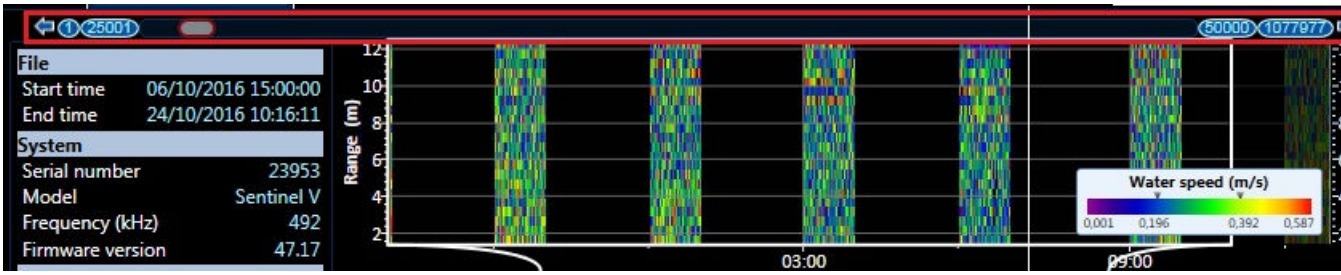

Figure 4.16: *An example of measured data, presented via the interface of the post-processing software.*

Raw data has been post-processed at Intechmer by E. Poizot: low-pass filtering (to account for perturbations produced by fishes) and high-pass filtering (for the noise in back-scattered intensity) have been used. More details can be found in the internal note in Ref. [69].

Depth and mean flow direction

Our facilities measure water currents occurring mostly in two opposite directions: Westward and Eastward flows. The following graphs (Figs. 4.17 and 4.18) illustrate the changes in the direction of the mean flow during neap and spring tides, during the period of measurements. In addition, the depth of the water column is shown. These two graphs emphasize some noteworthy facts listed below:

- The measuring depth which could be reached by the instruments varies from 13.5 m to 18.5 m during spring tides, and from 15.5 m to 16.5 m during neap tides.
- Ebb currents flow to the West at almost 270^o, and flood currents flow to the East at almost 90^o.
- Ebb starts a few hours before high tide, and flood starts after low tide during spring tides, and before low tides during neap tides.
- During neap tides, 2/3 of the flow is ebb, and 1/3 is flood.
- During spring tides, flood occupies 1/4 of the flow, and ebb takes the whole other 3/4 part.

Based on these observations, both ADCP's introduce almost the same data.

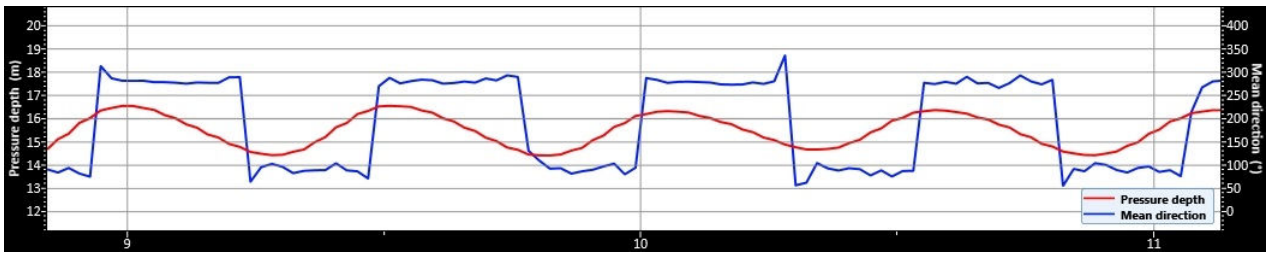

Figure 4.17: *Depth and mean flow direction during neap tides.*

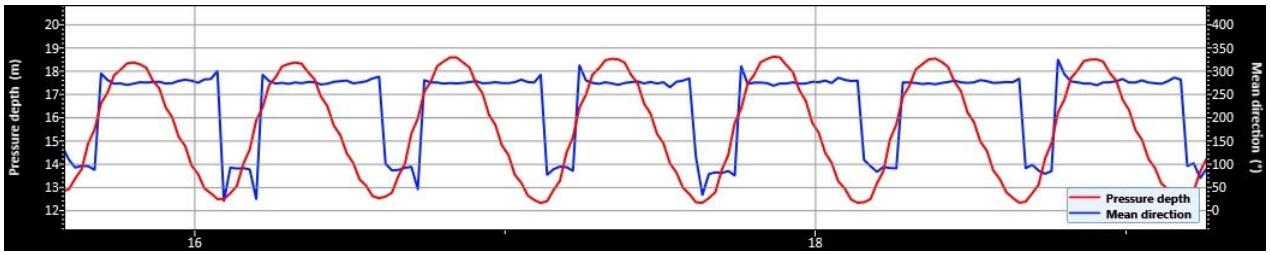

Figure 4.18: *Depth and mean flow direction during spring tides.*

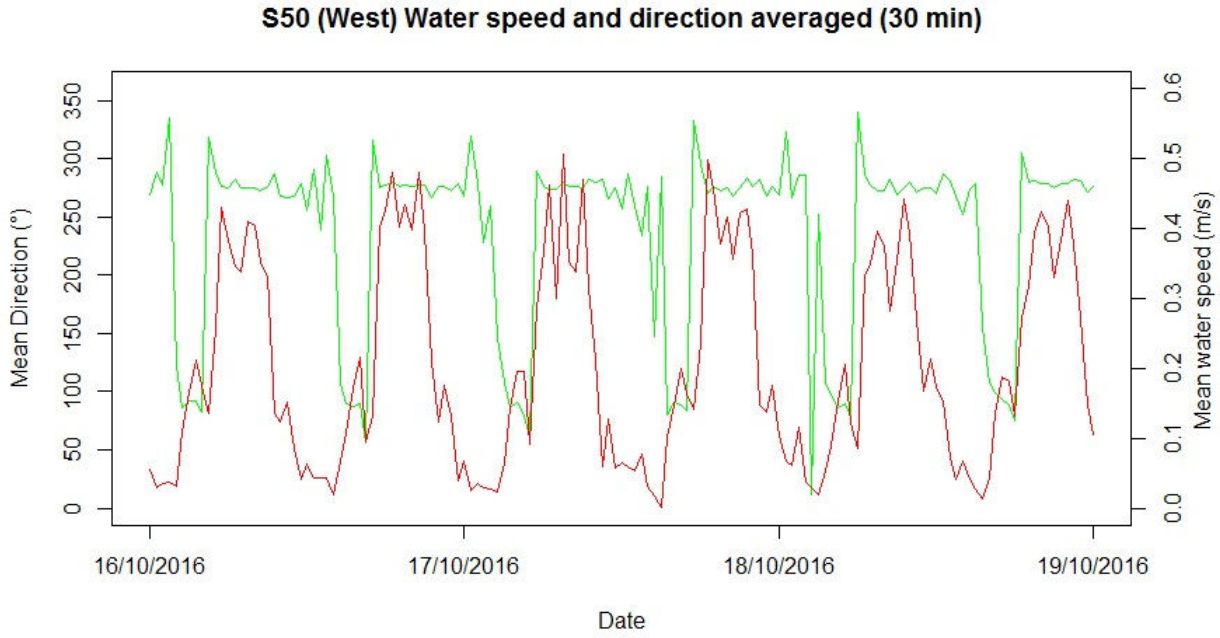

Figure 4.19: *Direction (green) and speed (red) of the mean velocity recorded by the Intechmer ADCP during four days.*

Figures 4.19 and 4.20 show the direction (degree) and speed ($m.s^{-1}$) of the mean velocity recorded by the Intechmer ADCP during four days. Both curves have been obtained by averaging recorded values over a time interval of 30 minutes. In general, the graph shows the changes of water speed with respect to the variation of the tide. During ebb-tide, when the current reaches its strongest, the East current (measured by the V50 ADCP) is stronger than the West current (measured by the S50 ADCP). This is because the ebb streams to the West, and the fishnet cage tends to attenuate the incoming flow. The same phenomenon can be observed when the current is lowest. West (S50) current is lower for a longer period. An opposite phenomenon is observed during the flood. At the end of the flood, the minimum water speed is reached for both ADCP's. This lowest velocity is observed to be slightly higher by the S50 (West) ADCP than by the V50 (East) ADCP. This is a consequence of the fact that the flood flows to the East, and is therefore slowed down by the fishnet cage located in between the two currents streaming West and East. Or in other words, this could be regarded as an evidence of "speed loss" due to the presence of the immersed structure.

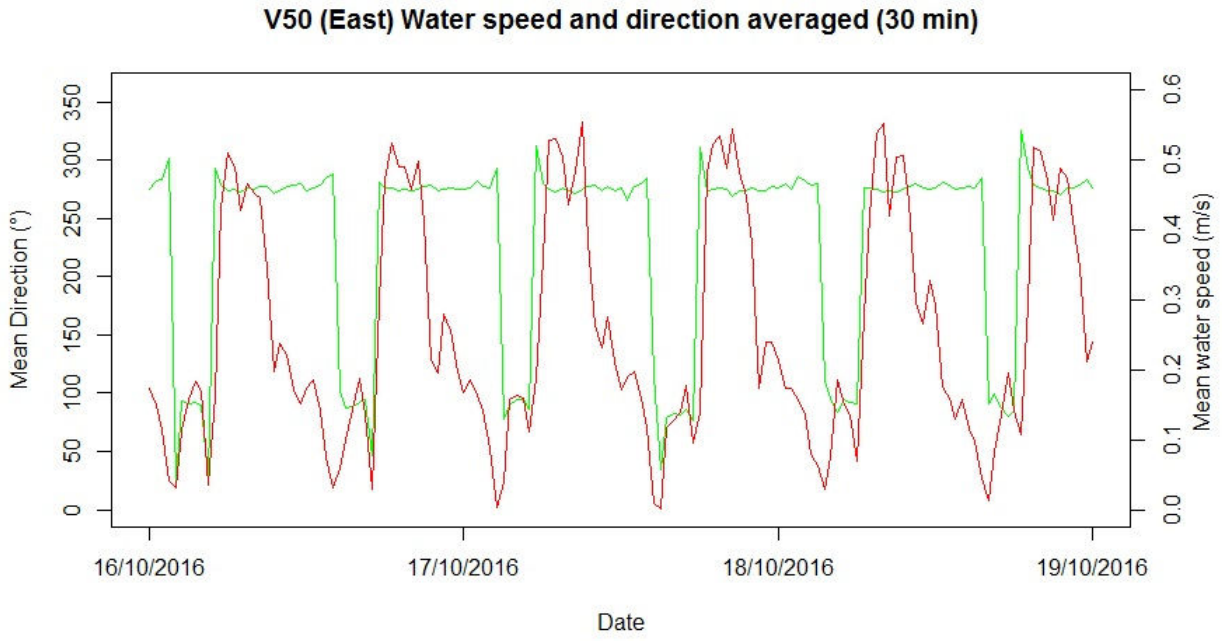

Figure 4.20: *Direction (green) and speed (red) of the mean velocity recorded by the IRSN ADCP during four days.*

4.6 Measurement results and comparison with models

4.6.1 Mean velocity profiles

To check qualitatively and quantitatively numerical and experimental data, we made comparisons between velocity magnitudes at corresponding positions. Thus, for each cell y_j ($j = 1, .., 22$) from top to bottom, we extracted samples $U_i(y_j)$ of velocity magnitude from ADCP's, corresponding to discrete times $t_i = i \times \delta t$, and averaged over N values to obtain the experimental mean velocity profile:

$$\overline{U}(y_j) = \frac{\sum_{i=1}^{N} U_i}{N}. \tag{4.4}$$

We chose $N = 1200$, together with a time step $\delta t = 1\,s$, so that the average was taken over $N \times \delta t = 20\,min$. (Note that some samples with undefined values were excluded from the averaging procedure.) Two datasets are presented, denoted as *DATA1* and *DATA2*, corresponding to two different times of measurement. Figure 4.21 shows the mean velocity profiles upstream and downstream of the cage, obtained from the *DATA2* dataset. We clearly observe that the upstream velocity is almost uniform throughout the water column, whereas the downstream

velocity is affected by the presence of the cage. This downstream profile will be compared to models in the next few lines.

Comparison with the theoretical model

We have considered the theoretical model of Chapter 2, to verify whether it could be applied to our field measurements. First, we noticed that the velocity averaged over the cross-flow direction y, which should be independent of the streamwise (horizontal) coordinate x in a perfectly 2D channel, does not take the same values upstream and downstream: differences of about 7 or 8 % are observed. This shows that the flow is not fully 2D here, and that, as expected, three-dimensional effects are present in the real cages. In spite of this approximation, the model can be used to recover interesting orders of magnitude. We observed that the ratio u_1/U_∞ was approximately equal to 1.2 for both *DATA1* and *DATA2*. According to Eq. (2.33) page 31, this corresponds to an effective drag coefficient:

$$C_{net} \approx 1.1 \tag{4.5}$$

This rather moderate value confirms the above observation (see dicussion page 80), i.e. that cages are not very dirty and have a low hydrodynamic resistance. A pedagogical interpretation of this value is proposed at the end of this section.

The experimental profile has been compared to our theoretical profile $\bar{u}(x_s, y)$ given in Eq. (2.59), at $x = x_s$, where x_s is the x-coordinate of the ADCP (as sketch in Fig. 4.22). Because the Intechmer ADCP was located 20 m away from the rear of the cage, we set:

$$x_s = x_b + 20\,m.$$

Also, simulations show that the turbulent zone does not start at $x = x_a$ (the very beginning of the cage), but at an unknown position $x = x_t$ where instabilities below the cage have occurred, and the laminar mixing layer has turned to a fully developed turbulent mixing layer. The theoretical erf (error-function) profile of Eq. (2.59) is then used with a renormalized variable $\xi = \sigma_0(y - a)/(x - x_t)$ instead of $\sigma_0(y - a)/(x - x_a)$. The origin of the fully turbulent zone has been taken to be the last quarter of the cage, that is $x_t = x_b - 40\,m$. This choice has no effect on the velocity reduction, by only affects the width of the erf profile. The shape of the experimental downstream profile suggests that the axis of the turbulent zone should be located

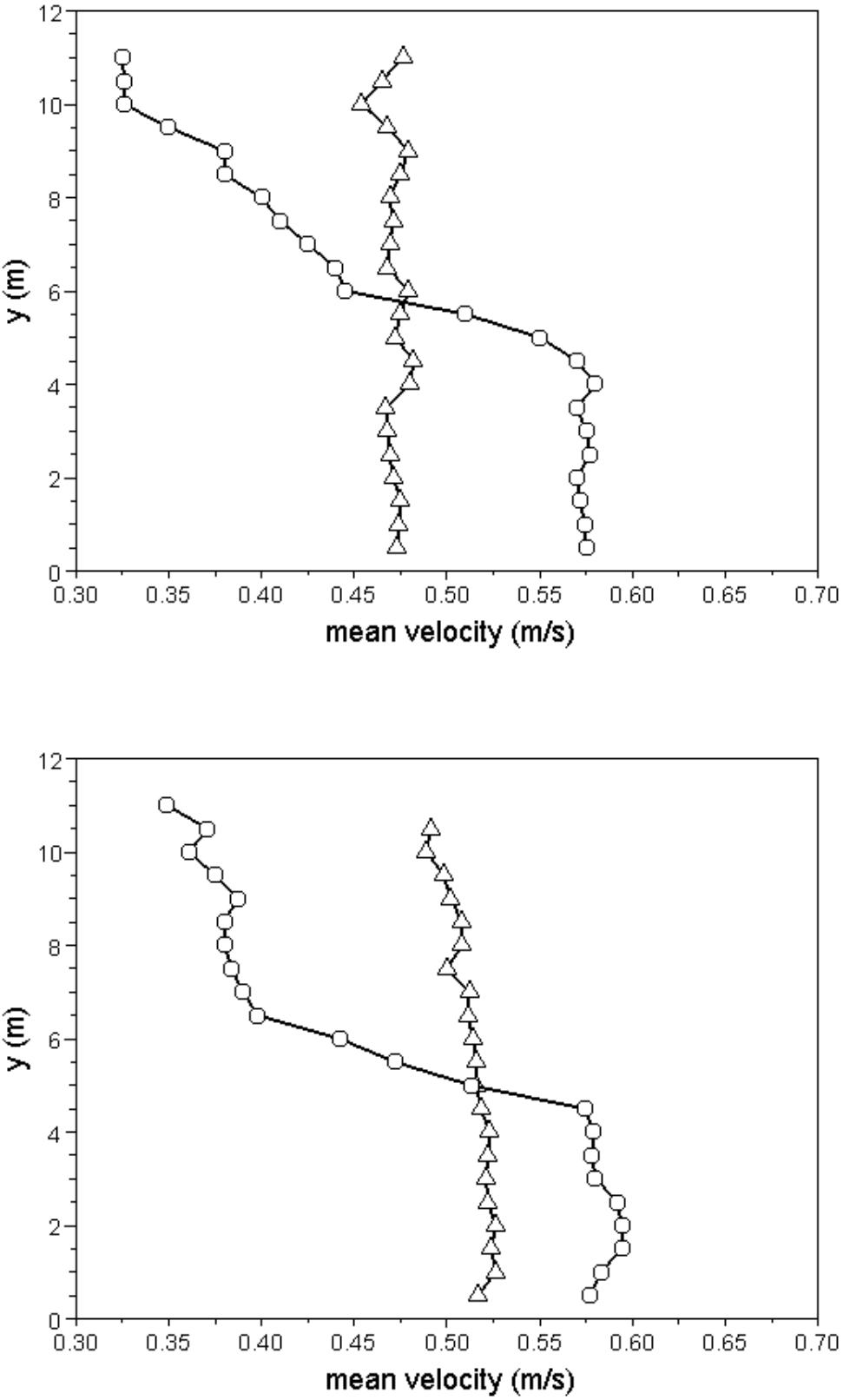

Figure 4.21: *Velocity profiles from datasets DATA1 (upper graph) and DATA2 (lower graph). Triangles: velocity upstream of the cage. Circles: velocity downstream of the cage.*

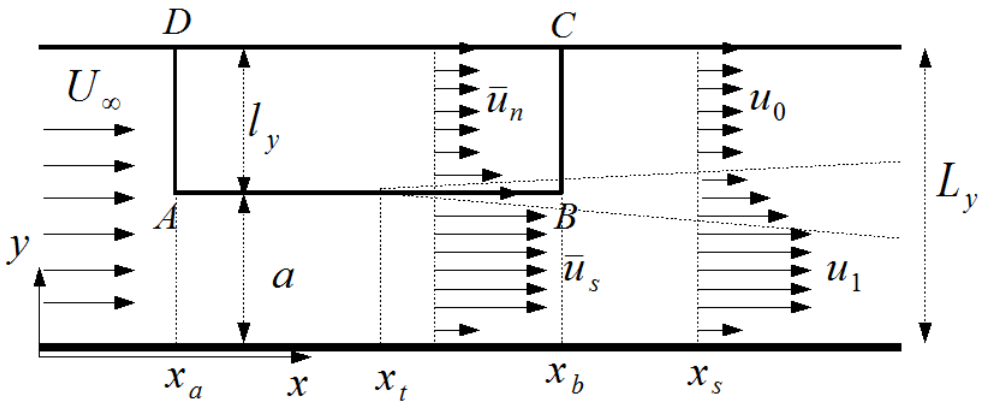

Figure 4.22: *Sketch of the model cage ABCD, showing the position of the beginning of the turbulent zone at* $x = x_t$.

at $y = 5.5\,m$, and this is the value that has been taken for a. We are aware of the fact that the real cage does not have a rectangular shape, and this is certainly an important approximation that will be discussed below.

Under these hypotheses, the resulting theoretical profiles could be calculated and are shown in Fig. 4.23, together with the corresponding experimental profiles from datasets *DATA1* and *DATA2*. We observe that the agreement is acceptable, and that the value $C_{net} \approx 1.1$, as well as the choice of the parameters x_t and a, allow realistic predictions of the various tendencies. As expected, the model is not very accurate, but this is due to the numerous simplifications it contains and which have been discussed in details at the end of Chapter 2.

An interpretation of the numerical value of C_{net}. To illustrate the value $C_{net} \approx 1.1$ for the effective drag coefficient, consider its definition (Eq. (2.5) page 24), in terms of the drag coefficient C_D of individual obstacles. In a real situation, these obstacles are composed of the border of the net, together with the numerous fishes swimming against the flow. Assume that the net and the fishes are removed, and replaced by fixed balls, with an individual drag coefficient $C_D \approx 0.44$ in the limit of large Reynolds numbers, and a diameter $d = 6\,cm$ (like tennis balls). The apparent surface of such balls is $s = \pi d^2/4 \approx 0.0028\,m^2$. Assume that balls are equally distributed throughout the cage, and that their number per cubic meter is $n = 22$, then formula (2.5) leads to: $C_{net} \approx 1.1$. Therefore, our cage can be thought of (hydrodynamically speaking), as a set of 22 tennis balls per cubic meter held fixed inside the nets.

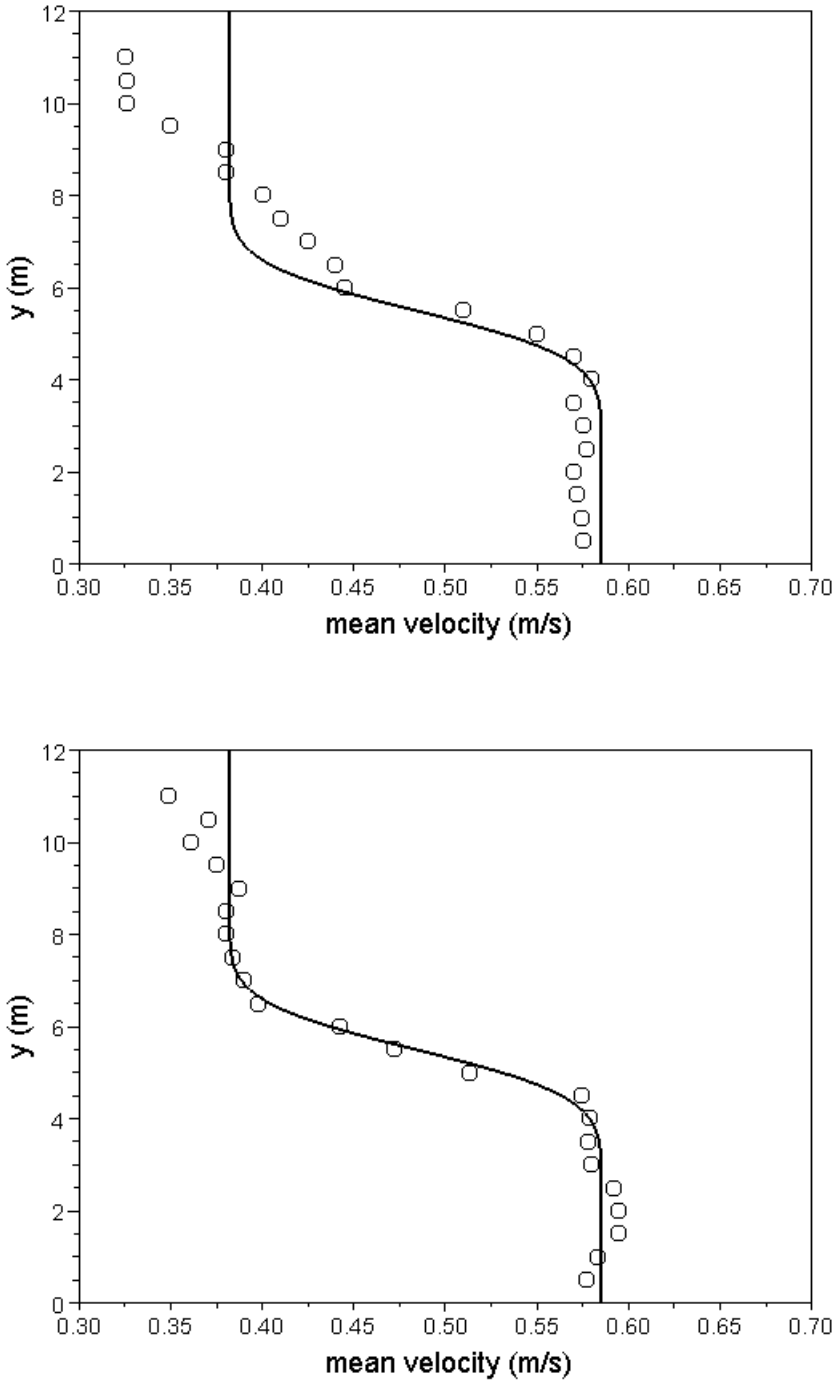

Figure 4.23: *Circles: mean velocity profile downstream of the cage, from DATA1 (upper graph) and DATA2 (lower graph). Solid lines: theoretical profiles* $\bar{u}(x_s, y)$ *(Eq. (2.59)) with* $x_s = x_b + 20\,m$, $x_b - x_t = 40\,m$, $L_y = 12\,m$, $a = 5.5\,m$, $C_{net} = 1.1$. *The upstream velocity* U_∞ *used in the model has been taken as the vertical average of the experimental downstream profile, which is close to* $U_\infty = 0.47\,m.s^{-1}$ *in both cases.*

4.7 Conclusion of this chapter

The effect of a real cage on the main stream has been highlighted, by means of ADCP measurements. Even though the cage under study was rather clean, a non-negligible flow reduction behind the cage (and an acceleration below) could be measured. The cage is out of reach of our numerical model, as the corresponding Reynolds number is of several million. However, we observed that some features of the analytical model were recovered experimentally, in spite of the numerous approximations of the theory.

Chapter 5

Transport of suspended particles around an immersed structure

This chapter is devoted to one of the most significant impacts of immersed structures in coastal flows, that is sediment resuspension and transport. Two approaches will be used to study this effect. Firstly, a numerical approach based on our RANS simulations, coupled to a discrete phase model for sediments, will be presented. Even though erosion and resuspension will not be included strictly speaking in this model, it will be shown that the immersed obstacle has a strong effect on sediment transport, especially if the obstacle has a small permeability (large C_{net}). Secondly, in-situ turbidity measurements performed near the fish cages of Cherbourg's roadstead will be reported. These data are in qualitative agreement with simulations, as they confirm that suspended sediments or effluents can be carried upward in the wake of the cage, and remain in this zone for some time, instead of being flushed away by the main flow.

5.1 General considerations and context of the study

As shown in the previous chapters, large immersed structures tend to act as floating barriers which cause changes to the direction, speed and characteristics of the flow passing over. These perturbations significantly affect the turbidity of water [68][38]. Therefore, estimating turbidity

in the wake of the cages is a crucial task to develop sustainable coastal industries, especially in the case of aquaculture. Indeed, as discussed in the introducing chapter, fish farms are placed in areas with high water circulation [66], to reduce their environmental impact as well as risks of fish diseases. This solution has two main advantages: (1) water inside the fishnet is regularly refreshed, so that the oxygenation conditions are enhanced, leading to better growing conditions for the fishes ; (2) faeces and uneaten fish food are expected to be transported downstream and diluted, therefore reducing the local environmental impact of the fish farm. In spite of these favourable conditions, high mortality rates can be recorded in farms under high stream flows [73]. The salmon fish farm of the roadstead of Cherbourg investigated in this thesis is under high tide current conditions, and its near area is regularly monitored by means of various environmental indicators (salinity, turbidity, sediment quality, benthic life, hydrodynamics, etc.). However, high mortality episodes were recorded in the last decade, and were not always clearly understood.

To determine possible causes of these events, various *external* processes have been proposed, such as flash floods, marine snow, amoeba infections, ferries and harbour traffic, etc. After field observations and measurements, no clear evidence could be retained to identify any of these external sources as directly responsible for fish mortality.

We therefore focused on possible contaminations by resuspended faeces or non-ingested feed (or any other fine sediment) emerging from below the fishnets, and produced by the accelerated flow under the production structures, as already suggested by Cromey et al. [23]. Our results are presented in the following sections and in Ref. [70]: it will be shown, using turbidity measurements and numerical simulations, that self contamination of cages by particles emerging from below the nets is possible.

Sources of particles. In this chapter, we will consider three categories of particles, described in the next few lines and sketched in Fig. 5.1, according to their sources.

- ***Far field particles***: representing sediments carried by the mean flow upstream from the immersed structure. In general, depending on the magnitude of the tide, they can have a wide range of shapes and weights. (These particles will be represented in blue in our simulations below.)

- ***Effluent particles***: these are particles produced by the industrial activity related to

the immersed structure itself. In the case of fishnets, effluent particles are mostly uneaten food and excrements. (Colored in red in our simulations.)

- ***Particles resuspended from the sediment bed***: this group includes materials accumulated at the sea bottom, and consisting of gravels, pebbles, sands and silts, shells, crustacean, etc. It can also contain effluents deposited on the bottom, and resuspended under high current conditions. (Colored in green in our simulations.)

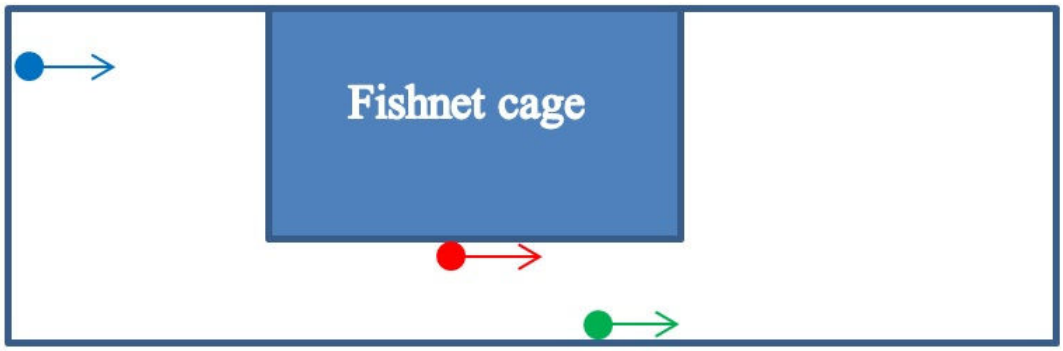

Figure 5.1: *Sources of particles: far field particles (blue), effluent particles (red), particles resuspended from the sediment bed (green). This colour code will be used throughout the chapter.*

5.2 Numerical analysis of sediment transport in a domain at laboratory scale

Simulations of sediment transport have been done by means of the Fluent software. The flow domain is the rectangular domain with a reduced scale already presented in Chapter 3 (i.e. depth = 1.2 m, cage length = 10 m, total length = 40 m). The physical assumptions concerning particles are presented in the next paragraphs.

5.2.1 Particle size distribution

ADCP measurements presented in the previous chapter have shown that the mean flow velocities range from 0.1 to 1.5 $m.s^{-1}$ according to the time of measurements. This current, upstream of the cage, already contains particles (the far field particles), which are relatively light. It can also

contain effluent particles with various weights and sizes, some of which are quickly deposited, others being transported away. Also, the current is likely to resuspend particles from the sand bed. We have chosen to simulate particles with radii r_p distributed in the range:

$$0.1\,mm \leq 2r_p \leq 10\,mm \tag{5.1}$$

with a Rosin-Rammler distribution. According to the Hjulström - Sundborg diagram (Fig. 5.2), in a flow of velocity $U_\infty = 0.5\,m.s^{-1}$ like the one considered here, particles between $0.1\,mm$ and $1\,mm$ could be brought from the far field or produced by erosion from the bed. Particles between $1\,mm$ and $10\,mm$ are also likely to be transported in the main stream. In contrast, particles above a few $10\,mm$ are less likely to be suspended in such flows. Therefore, the range (5.1) appears to be appropriate for the situation considered here.

The density of simulated particles is taken to be $\rho_p = 2710\,kg.m^{-3}$, which is close to usual values of sand particles found in the site under study. The total mass flow rate of injected particles has been taken to be $10^{-5}\,kg.s^{-1}$ in all cases.

5.2.2 Particle motion equation and non-dimensional parameters

Following discussions in the previous section, it is assumed that particles are much smaller than the mean flow length scales, and that their concentration is small. In particular, they do not modify the flow and do not interact. The motion equation of each particle reads:

$$\frac{d\vec{x}_p}{dt} = \vec{V}_p(t), \tag{5.2}$$

$$m_p \frac{d\vec{V}_p}{dt} = C_D \frac{1}{2} S_p \rho_f |\vec{V}(\vec{x}_p,t) - \vec{V}_p(t)|(\vec{V}(\vec{x}_p,t) - \vec{V}_p(t)) + (m_p - m_f)\vec{g}, \tag{5.3}$$

where $\vec{x}_p$ and $\vec{V}_p$ are the particle position and velocity, m_p is the mass of the particle, m_f is the mass of fluid displaced by the particle ($-m_f\vec{g}$ is the buoyancy force). C_D is the drag coefficient, which depends on the particle Reynolds number $Re_p = 2|\vec{V} - \vec{V}_p|r_p/\nu$ (where r_p is the radius of the particle, which is assumed to be spherical here). The apparent surface of the particle is $S_p = \pi r_p^2$. Other contributions of the hydrodynamical force (pressure gradient of the undisturbed flow (i.e. Tchen's force), added mass, Boussinesq-Basset history force, lift), will be neglected. For a detailed discussion about the physical origin and the relevance of these forces, see Gatignol (1983) [37], Maxey & Riley (1983) [62]. Specific discussions about lift and Basset

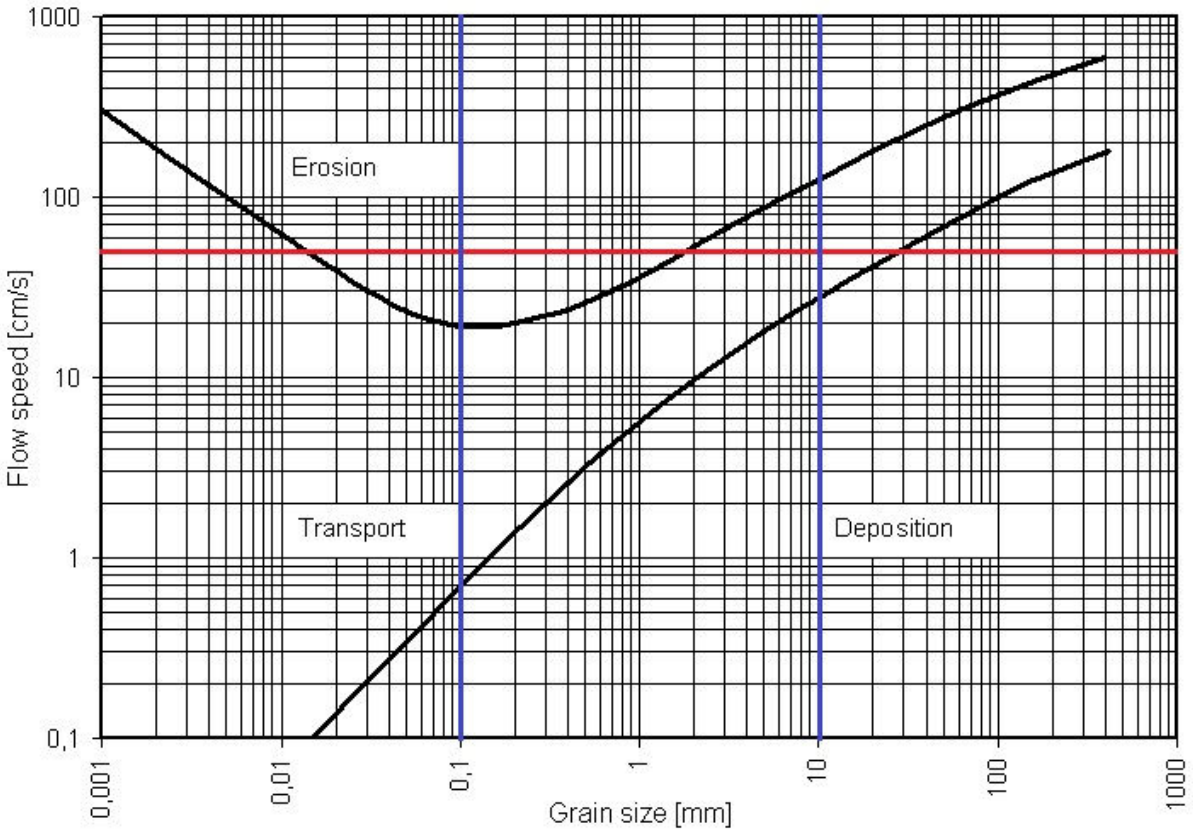

Figure 5.2: *The Hjulström-Sundborg diagram [47][77], showing the relationships between particles' size and their ability to be transported, eroded or deposited in river flows. The red line corresponds to* $U_\infty = 0.5\, m.s^{-1}$. *Blue lines indicate the range of particle sizes considered in our simulations.*

forces can be found in the works by Magnaudet (1997) [61], Candelier et al. (2004 and 2005) [16][17], Candelier & Angilella (2006) [15]. For a discussion about the Maxey-Riley-Gatignol equation applied to sediments, see Escaurazia & Sotiropoulos (2011) [26].

In Eq. (5.3), vector $\vec{V}$ is the mean fluid velocity given by the RANS simulations which have been described in details in Chapter 3. Hence, the drag force appearing in this equation does not account for the effect of turbulent eddies on the particle. This is an important effect however, since it causes the turbulent dispersion of suspended sediments. In order to take this effect into account, we make use of the classical "eddy lifetime model" [74] [42] (also called the Discrete Random Walk model), which consists in assuming that the particle interacts with an eddy of typical velocity $u' = \sqrt{2k/3}$ (the rms velocity of turbulent fluctuations), which is characterized by an eddy lifetime τ_e depending on the local turbulence characteristics. One usually takes $\tau_e = 2T_L$, where T_L is the Lagrangian time scale, i.e. the integral scale of the autocorrelation function of fluid points velocity. It is computed from the second-order moments as:

$$T_L \simeq C_L \frac{k}{\varepsilon}$$

where $C_L \approx 0.15$ is a non-dimensional constant (other values are also proposed in the literature), and k (turbulent kinetic energy per unit mass) and ε (turbulent dissipation per unit mass) have been presented in Chapter 3. During a period τ_e, a random velocity component $u'\vec{\xi}$ is added to the mean fluid velocity (where $\vec{\xi}$ is a normalized random vector). The particle will interact with this vortex during a time lapse T depending on τ_e and on the particle response time $\tau_p = m_p/(6\pi\mu r_p)$. In the eddy lifetime model implemented in Fluent one uses (see also Graham [41]):

$$T = \min(\tau_e, t_{cross}) \tag{5.4}$$

where t_{cross} is the time required for the particle to cross the vortex, which is modelled as

$$t_{cross} = -\tau_p \ln\left(1 - \frac{L_e}{\tau_p|\vec{V} - \vec{V_p}|}\right). \tag{5.5}$$

In the limit of large particle inertia this leads to

$$t_{cross} \approx \frac{L_e}{|\vec{V} - \vec{V_p}|} \tag{5.6}$$

which corresponds to the ballistic limit. In contrast, in the limit of weak particle inertia ($\tau_p \to 0$), t_{cross} diverges and the interaction time is simply equal to the eddy lifetime $T = \tau_e$: the particle

trajectory is affected by the vortex till the vortex vanishes. Finally, after a time T, a new fluctuating velocity is considered by creating a new random vector $u'\,\vec{\xi}$.

Stokes number and fall velocity of particles. Prior doing heavy simulations, it is convenient to estimate the orders-of-magnitude of the particle response time, Stokes number, fall velocities, and fall Reynolds numbers. By using a linear drag law (i.e. taking $C_D = 24/Re_p$), as expected for particles with a small Reynolds number, and dividing Eq. (5.3) by m_p, we are led to:

$$\frac{d\vec{V}_p}{dt} = \frac{1}{\tau_p}(\vec{V}(\vec{x}_p, t) - \vec{V}_p(t)) - \frac{V_T}{\tau_p}\vec{e}_y, \tag{5.7}$$

where

$$\tau_p = \frac{m_p}{6\pi\mu r_p} = \frac{2}{9}\frac{\rho_p}{\rho_f}\frac{r_p^2}{\nu} \tag{5.8}$$

is the particle response time already discussed above, and

$$V_T = \frac{(m_p - m_f)g}{6\pi\mu r_p} = \frac{2}{9}\left(\frac{\rho_p}{\rho_f} - 1\right) g\frac{r_p^2}{\nu} \tag{5.9}$$

is the fall (or settling, or terminal) velocity in still fluid and in Stokes flow conditions (Re_p less than about 4). For more inertial regimes ($Re_p \gg 1$), Eq. (5.3) does not provide any explicit relation for V_T (because C_D depends on the particle velocity in a more complex manner), so that we choose to make use of the simplified, empirical, explicit and easy-to-use, formula of Chen (1997) [21]:

$$V_T = \frac{\nu}{2r_p}\left(\sqrt{25 + 1.2d_*^2} - 5\right)^{3/2} \tag{5.10}$$

where

$$d_* = 2r_p\left((\frac{\rho_p}{\rho_f} - 1)\frac{g}{\nu^2}\right)^{1/3}.$$

From these quantities we obtain two important non-dimensional parameters. By using a flow length scale L, and velocity scale U_∞, the non-dimensional response time (Stokes number) is:

$$St = \frac{U_\infty\,\tau_p}{L}. \tag{5.11}$$

When $St \ll 1$, particles instantly obey the mean flow, i.e. they have no inertia. In contrast, $St \gg 1$ indicates an inertial regime. In the table below, we have taken $L = 1\,m$ and $U_\infty = 0.5\,m.s^{-1}$, which are relevant orders-of-magnitude for our simulations at laboratory scale. The fall Reynolds number, that is the particle Reynolds number Re_p in still fluid, is

$$Re_T = \frac{2r_pV_T}{\nu}. \tag{5.12}$$

The table below shows these parameters for three typical particle sizes.

diameter $2r_p$ (mm)	0.1	1	10
response time τ_p (s)	0.0014	0.14	14
Stokes number St	$7\,10^{-4}$	0.07	7
fall velocity V_T $(m.s^{-1})$	0.01	0.11	0.44
V_T/U_∞	0.02	0.22	0.88
fall Reynolds number Re_T	1	110	4400

These values show that particles of size 0.1 mm travel in inertialess conditions: both the inertia of the particle and the inertia of the fluid can be neglected to simulate these objects, as both the Stokes and the terminal particle Reynolds numbers are smaller than unity. Also, these particles sediment, but their settling velocity (1 $cm.s^{-1}$) is much smaller than the main flow velocity. Particles of size 1 mm still have a small Stokes number, but they are more sensitive to gravity. They are expected to sediment in the conditions considered here. Particles of size 10 mm have an inertial dynamics: their proper inertia is not negligible ($St \not\ll 1$). In addition, the inertia of the fluid displaced by such particles is important, as the Reynolds number of these objects is large, so that their dynamics is dominated by wake effects and non-linear drag. Also, sedimentation is significant for such particles.

Note that even though V_T/U_∞ is small, the ratio V_T/u_n (where u_n is the typical horizontal velocity inside the cage), might not be small. Indeed, according to the values of C_{net}, velocities inside the cage can be much smaller than the upstream velocity. In particular, when C_{net} is large, *we expect sedimentation to be significant within the cage*, even for our smallest particles. This point will be checked in the following section.

Initial conditions for particles. In order to integrate Eqs. (5.2)-(5.3), initial conditions are required for the position $\vec{x}_p(0)$ and velocity $\vec{V}_p(0)$ of the particles. As already discussed in Fig. 5.1, initial positions will be taken at the inlet of the domain for far field particles, along a segment just below the net at $y = a$ for effluent particles, and along a horizontal segment slightly above $y = 0$ for particles from the sediment bed. Initial velocities are equal to the local mean fluid velocity.

5.2.3 Results: particle dispersion for C_{net} = 1, 100 and 1000

Figures 5.3, 5.4 and 5.5 show particle trajectories for increasing values of C_{net}, i.e. from very permeable cages ($C_{net} = 1$) to nearly impermeable cages ($C_{net} = 1000$).

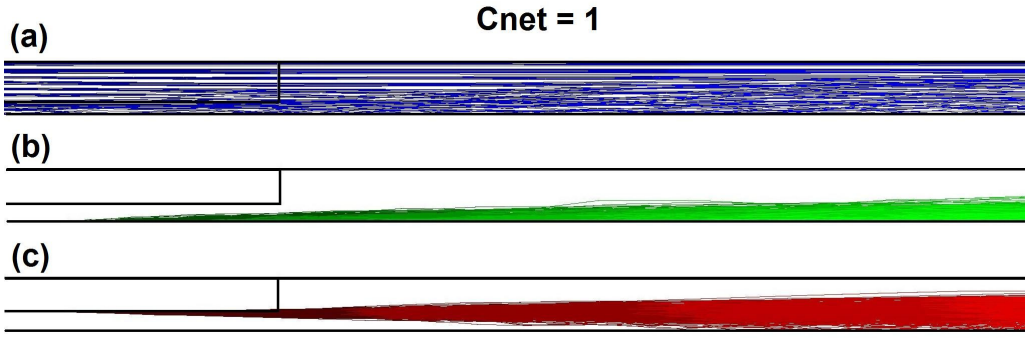

Figure 5.3: *Particle trajectories in the case* $C_{net} = 1$. (a) *: particles transported by the upstream flow ;* (b)*: particles from the seabed ;* (c)*: effluent particles.*

When $C_{net} = 1$, trajectories are nearly linear, and show very few randomness. This is a clear indication that turbulence intensity is small in this case, as expected since the only source of turbulence is the velocity difference between the interior of the cage and the fast flow below. This difference being rather limited for such a permeable ("clean") cage, particles' random walk is also small. A small randomness is however visible below the cage, where some turbulence is created, and is responsible for the expansion of the plumes. Sedimentation seems to have very little effect in this flow where velocities are close to 0.5 $m.s^{-1}$ almost everywhere, except in the bottom boundary layer.

When $C_{net} = 100$ (Fig. 5.4), the cage is much less permeable and trajectories are significantly different from the previous case. Random walk is more pronounced, as the turbulent intensity is now larger. A new effect is visible however: particles from the upstream flow now sediment *within the cage*. This is in agreement with the fact that the velocity inside the cage drops down to about $0.1\,m.s^{-1}$ (see Fig. 3.12 page 61). Therefore, the fall velocity is no longer negligible compared to the mean fluid velocity, as soon as particles are larger than 1 mm (see table page 98). Settling therefore occurs along oblique lines that are clearly visible in Fig. 5.4.

A closer look at Fig. 5.4 also shows that effluents or particles from the upstream flow can

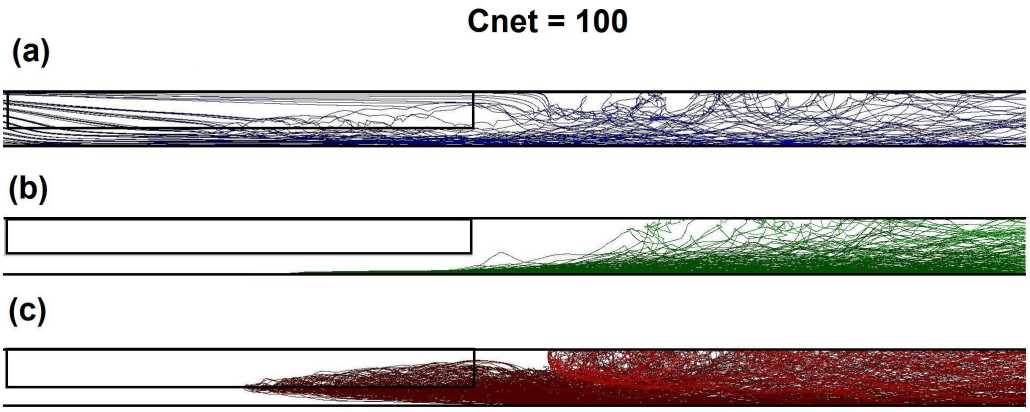

Figure 5.4: *Particle trajectories in the case* $C_{net} = 100$. (a) *: particles transported by the upstream flow ;* (b)*: particles from the seabed ;* (c)*: effluent particles.*

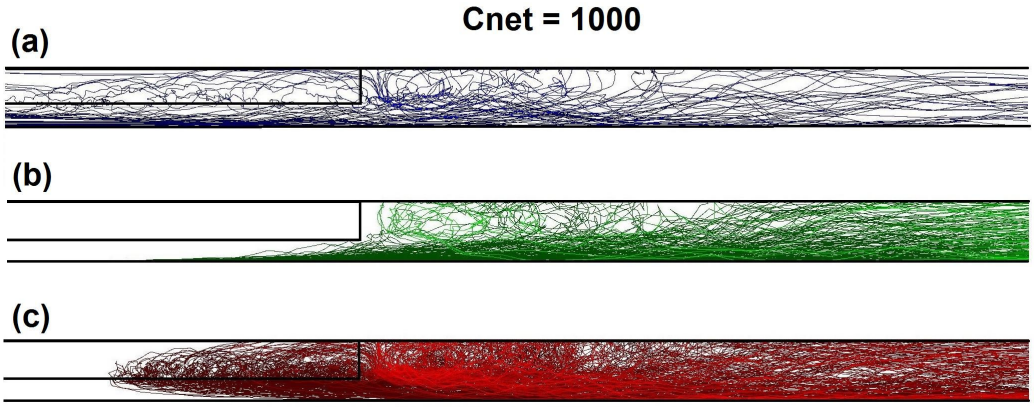

Figure 5.5: *Particle trajectories in the case* $C_{net} = 1000$. (a) *: particles transported by the upstream flow ;* (b)*: particles from the seabed ;* (c)*: effluent particles.*

contaminate the cage, whereas green particles, produced at the sandbed, are convected away from the cage. This is no longer the case when $C_{net} = 1000$ (Fig. 5.5). In this case the cage is nearly impermeable, as shown in Chapter 3, a strong flow exists below the cage and a large recirculation cell appears at the rear of the cage, like the one of Fig. 3.10 page 58. Under the effect of turbulent dispersion, even green particles are trapped within this cell and spin there for a few convective times. This effect can lead to a "self-contamination" of the cage, which has been studied in details in Ref. [70]. Even though such particles do not necessarily penetrate into the cage by crossing its rear end limit, the fact that they remain there for a long time creates favourable conditions for the self-contamination. Indeed, in case of flow reversal, these particles will be driven towards the interior of the cage and contaminate the fishes.

Note on the validity of the eddy lifetime model for large turbulent intensities. The eddy lifetime model used for turbulent dispersion, described in section 5.2.2, is known to be very approximate when turbulent intensity is large [41][42]. Indeed, in this case the model overestimates turbulent dispersion. Therefore, the results of Figs. 5.4 and 5.5 must be interpreted with care. Other methods, like LBM-LES[1], should provide more accurate results since they accurately describe the dynamics of unsteady vortices. These approaches are left as a perspective to this thesis.

5.2.4 Path lengths

In order to quantify the tortuosity[2] of particles' motion, we have chosen to plot the path length $L_p(t)$ of a trajectory $(x(t), y(t))$ versus $x(t)$. Indeed, in the case of a uniform motion at constant velocity U_∞ we have, obviously:

$$L_p(t) = x(t) - x_{inj}, \tag{5.13}$$

where x_{inj} is the abscissa of the injection point. In other words, by differentiating with respect to x, a regular trajectory is characterized by:

$$\frac{dL_p}{dx} = 1. \tag{5.14}$$

[1]Lattice Boltzmann Method - Large Eddy Simulation.

[2]Rigorously speaking, tortuosity is defined as the path length $L_p(t)$ between two points, divided by the distance between these points. It is equal to 1 for straight trajectories and much larger than 1 for very convoluted trajectories.

This last equation is more general than (5.13): it indicates *locally* that the trajectory is regular and horizontal. In contrast, when turbulent dispersion is present, the path length and $x(t)$ are linked in a more complex manner: the curve (L_p, x) is no longer single-valued, but it allows to unfold the trajectory in the 2D plane. Figure 5.6 shows these curves when $C_{net} = 1$ and 1000, for a single effluent test particle released at $x_{inj} = 15\,m$. In the former case we observe that the law (5.13) is satisfied with a great accuracy. In the latter case, Eq. (5.13) is no longer satisfied: the zigzags correspond to the capture of the particle in the recirculation cell behind the cage, and to its backward motion towards the cage. After two rotations in this cell, the particle is driven directly downstream in a regular manner and the law (5.14) is clearly satisfied. The final path length, obtained when the particle exits the flow domain, is observed to be equal to 25 m when $C_{net} = 1$ and to 38 m when $C_{net} = 1000$: this example shows how the lack of permeability of the cage directly affects the complexity of trajectories and the evacuation of effluents.

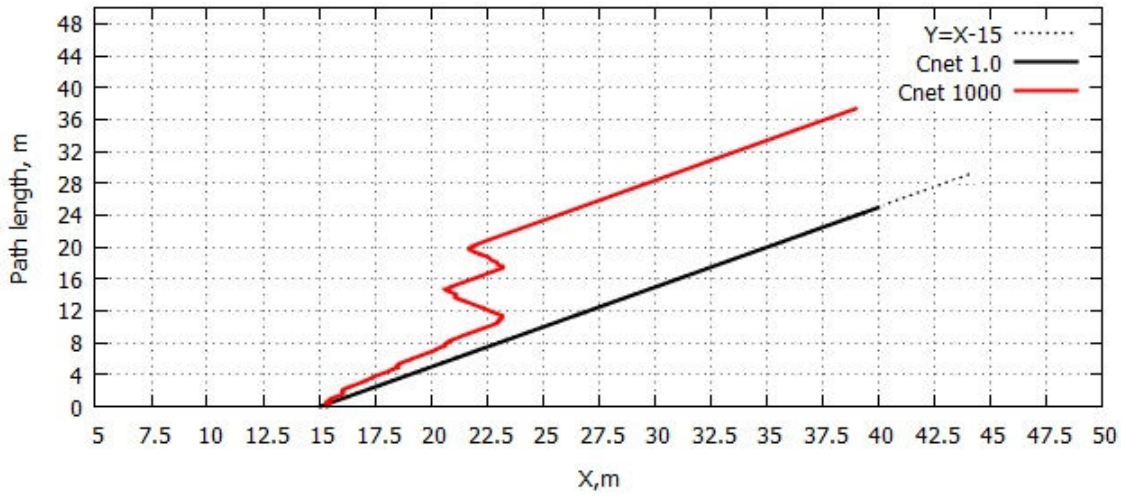

Figure 5.6: *Path length of a test effluent particle released at* $(x = 15, y = a)$*, versus the* x*-coordinate of the particle. The dashed line is Eq. (5.13). The rear of the cage is at* $x = x_b = 20\,m$*, and the outlet section is at* $x = 40\,m$*.*

The computations presented in this section suggest that effluents, but also particles eroded from the sandbed below the net, could be found to wander for a long time near the rear end of the cage. This is confirmed by in-situ measurements performed in the set of cages of Cherbourg, and presented in the next section.

5.3 Comparison with in-situ turbidity measurements

In May 2015, turbidity measurements were conducted near a set of cages, like the one discussed in Chapter 4, composed of 8 square nets distributed on a horizontal 2-by-4 grid, in Cherbourg's roadstead. Winds were light or nil during the survey, and the sea surface was very flat. By using a Niskin bottle, discrete samples were taken: 1) near the water surface ($\sim 1\,m$ water depth), 2) at mid depth, and 3) about $1\,m$ above the bottom (Fig. 5.7). Positioning at sea was performed by means of a DGPS device.

Because the roadstead is under the influence of a semi diurnal tide regime, which generates currents up to $1\,m.s^{-1}$ one meter above sea bottom, six successive surveys were conducted. The first two were performed respectively 2 hours and 1 hour before current reverse. The four last surveys were done respectively 1, 2, 3 and 4 hours after current reverse.

Six sample stations were regularly investigated. The first one was located $20\,m$ away from the western side of the structure. The other stations were regularly distributed on the eastern side (every $20\,m$), along a line running through the middle of the set of square fishnets (Figs. 5.7A and B). The turbidity of each water sample was measured using a Hach 2100AN turbidimeter (Hach, USA) and expressed in NTU (Nephelometric Turbidity Units).

In the area under consideration, the mean turbidity is about 10 NTU [63] [53]. When the tidal stream flows westward (Fig. 5.7 C and D), the area located upstream from the cages exhibits low turbidities, of the order of the background level. However, a slight increase in turbidity (23-27 NTU) is observed $20\,m$ before the foot cage. Downstream, turbidity is substantially higher ($>$ 40 NTU), whatever the depth and the current conditions under study. As the stream flows eastward (Fig. 5.7 E to H), the turbidity is very low upstream from the cage. In contrast, the bottom sample (i.e. near the foot cage), systematically shows higher turbidity levels (up to 54 NTU). In the downstream area, high turbidities appear evenly distributed close to the bottom ($1\,m$ above), and this is so whatever the conditions under study.

In the water column, very high turbidities ($>$ 100 NTU, that is 10 times the background level) were measured. These values were observed on the surface and at mid depth. No well-defined organization could be highlighted, as very strong turbidity values (134 NTU) can mingle with very low turbidity values ($<$ 10 NTU).

In summary, high turbidity levels were measured near the foot cage in the upstream area. In

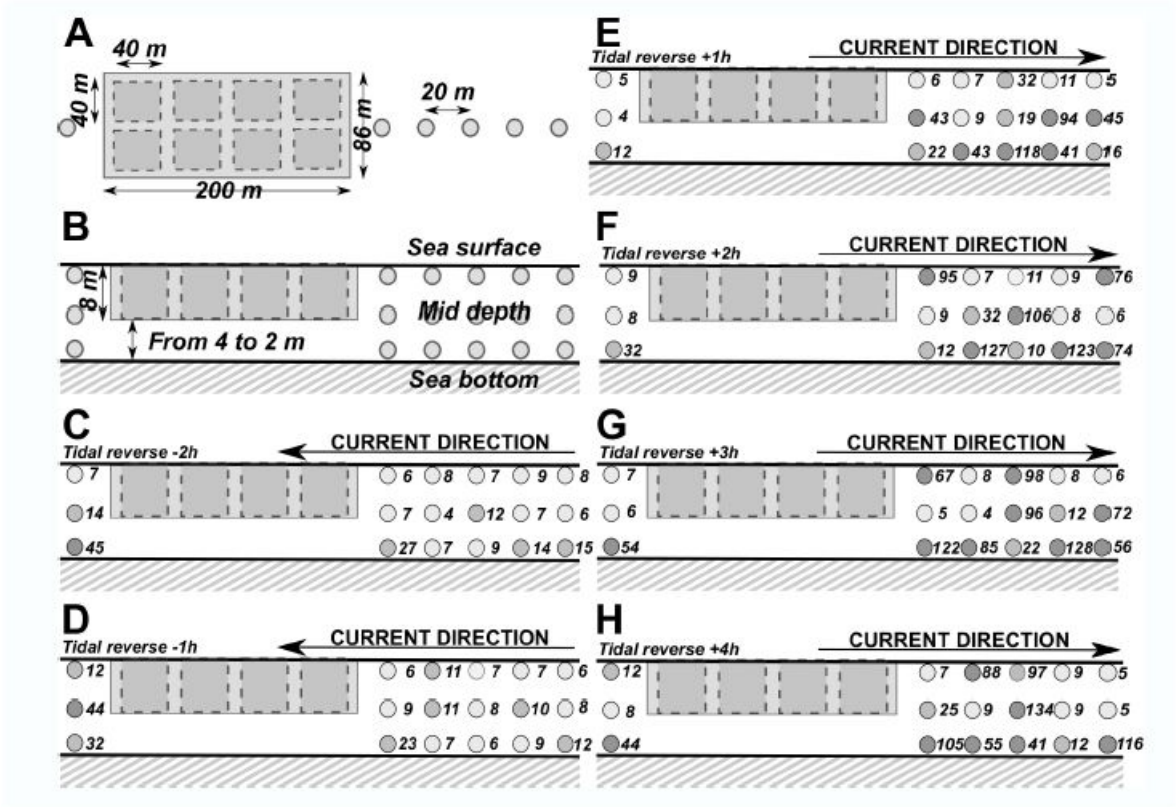

Figure 5.7: *Turbidity measurements in NTU units. (A): top view of water sample locations. (B): cross-sectional view of water samples. From (C) to (H): cross-sectional view corresponding to the various current times indicated on the figure.*

the downstream area, strong turbidities were observed from the rear of the cage to more than 100 m downstream, on average about 1 meter above the bottom, but strong heterogeneities along the water column were identified, showing a "bull's-eye effect".

These measurements are therefore in qualitative agreement with the numerical simulations presented in section 5.2. Indeed, in contrast with the measurements of October 2016 described in Chapter 4, the turbidity measurements of May 2015 were done at the rear of extremely dirty cages[3], which might correspond to large values of C_{net}. Strong turbulence intensities, as well as recirculation cells, might therefore explain the high turbidity levels recorded downstream of the cages.

[3]Unfortunately, no ADCP measurements could be done in the May 2015 campaign. Such measurements would have helped us to estimate an appropriate value for the effective drag coefficient C_{net} to be used in the models.

Chapter 6

Conclusion and discussion

The work presented in this thesis brought some information about hydrodynamic transport in the vicinity of an immersed structure in shallow water. The typical situation considered here concerns aquaculture cages, but we believe that the concepts and methods developed throughout the thesis can be applied to various situations. Three approaches have been carried out: a theoretical (analytical) study, which is known to be very efficient for flows at extremely large Reynolds numbers ; a numerical study, which accounts for key effects that are neglected in the analytical approach ; an experimental campaign which brought us important information for the understanding of the hydrodynamic environment of the cages.

This chapter summarizes the whole content of the thesis and accentuates its contributions. We also discuss through this part the limitations of our approaches as well as possible perspectives.

6.1 Recapitulation of the research

The complexity of transport phenomena considered here led us to develop an analytical model (Chapter 2), valid in the limit of very large Reynolds numbers. This theoretical approach, being based on strong simplifications, is not expected to predict currents with a high accuracy. However, it helped us understand the relevance of the various mechanisms in different parts of the domain. Also, it provided orders-of-magnitude for hydrodynamic quantities of interest like the mean velocity or turbulent intensity.

Because the thesis is devoted to the understanding of the flow in the water column, we chose to perform all calculations in the vertical plane, and in two-dimensions only. The cage was assumed to be a rectangular fixed and porous object. The various elementary obstacles that create the drag were assumed to cover the whole volume of the cage, to mimic the presence of numerous fishes swimming against the stream and remaining fixed with respect to the cage. A volume force with effective drag coefficient C_{net} was then included into the Navier-Stokes equation to account for this drag. Assuming that the concentration of elementary obstacles was uniform, the volume force took a very simple form. This approach is different from approaches based on the sole net solidity, which are appropriate for empty nets were the drag is only due to a surface distribution of elementary obstacles on the net boundary (the twines). The link between the total drag of the cage and the distribution of these objects, either volumic or surfacic, has been discussed in Chapter 2, page 24.

We then identified various zones where viscous effects and/or turbulence were non-negligible: (1) the mixing layer between fast flow below the cage and slow flow inside or behind the cage, (2) the bottom boundary layer. Outside these zones, we made use of the potential flow assumption which allowed us to derive a simple set of equations for velocity and pressure drop (Eqs. (2.32), (2.33) and (2.34) page 31). These results were in good agreement with numerical simulations (see for example Fig. 2.4). These solutions were then used as external flows to be matched with the flow inside the mixing layer (the bottom boundary layer was ignored). By revisiting the Prandtl equations inside the mixing layer we could show that, for strongly permeable cages (small C_{net}), the self-similar profile of Goertler was an acceptable approximation.

A *numerical study* (Chapter 3) was also developed, in parallel with the analytical one, to account for more complex effects and to study more impermeable cages (larger C_{net}'s). The same geometry was considered. Turbulence was modelled by means of the $k-\omega$ model (in place of the mixing-length model in the analytical study). Fine meshing was used near walls. In contrast with the analytical approach which is a priori valid for extremely large Reynolds numbers, the simulations could not be run with Re of a few million. They were run with $Re = U_\infty L_y/\nu = 6.10^5$ (that is $U_\infty = 0.5\,m.s^{-1}$ and $L_y = 1.2\,m$), instead of $Re = 6.10^6$ (corresponding to the real depth $L_y = 12\,m$). This *reduced scale* model allowed us to have y^+ of order unity to a few tens near walls.

Though the numerical model also is based on strong simplifications (rectangular 2D domain, rigid cage, absence of waves, no turbulence production inside the cage, etc.), it still brings out interesting hydrodynamic information. As expected, simulations agree with the theoretical model in the case of moderate C_{net}'s, typically from 1 to 5. However, the numerical model goes further with abundant qualitative results for larger C_{net}'s, corresponding to more impermeable cages, which can be thought of as "full" or "dirty". For C_{net} of a few tens, the formation of a recirculation cell was observed at the rear end of the cage. The size of this recirculation cell (or cell-extent) is very sensitive to the value of C_{net}. When C_{net} reaches a few hundred, an asymptotic flow structure appears and the cell-extent no longer depends on C_{net}. Numerical simulations also show how the relative flow rate Q_i passing through the cage depends on C_{net}. Q_i drops down to about 10% for $C_{net} > 500$, corresponding to nearly impermeable cages. An empirical power-law, valid for a wide range of C_{net}'s has been proposed (page 59).

In Chapter 4, *in-situ measurements* carried out during October 2016 were presented. The environmental conditions of these measurements were also recorded: temperature and rainfall, atmospheric pressure, tides. ADCP current meters deployed upstream and downstream of a cage (streamwise length: 160 m, width: 33 m, average depth: 8 m) enabled to measure velocity profiles showing that the flow is strengthen below the cage and reduced behind the cage. This effect was in quantitative agreement with the theory, provided a value $C_{net} = O(1)$ was chosen. This moderate value corresponds to rather clean cages, with a limited number of fishes, in agreement with visual observations of the cage in October 2016.

Another set of measurements was also used in this thesis. It concerns turbidity measurements recorded in May 2015 upstream and downstream of a cage. These results have been presented in Chapter 5, which is devoted to sediment transport and is briefly discussed in the next few lines.

The *motion of sediments* in this flow was investigated numerically (Chapter 5), by using a Lagrangian approach for particles, which were assumed to be passive (no effect on the flow) and isolated (no particle/particle interaction). This method allows to track clouds of suspended sediments as soon as the fluid velocity field is known. Here, the local mean velocity of the fluid was simply taken from the RANS simulations of Chapter 3. Particles were assumed to have a density of about $2700\, kg.m^{-3}$. By making use of the Hjulström-Sundborg diagram, we chose

diameters in the range $0.1\,mm$ to $10\,mm$. Turbulent dispersion was modelled by means of the eddy-lifetime model.

These two-phase simulations revealed that sediment dispersion is very sensitive to the permeability of the cage, as the complexity of particle trajectories depends on C_{net}. This effect has been highlighted by computing path lengths, which have been observed to drastically increase when C_{net} increases. It is due to the fact that weakly permeable cages create flow instabilities and turbulence. This can lift up particles at the rear of the cage. In addition, the large steady recirculation cell behind the cage has been observed to trap particles for some time and to delay their evacuation. This effect could cause a kind of "self-contamination" of the cage, as it can retain effluent particles produced by the cage itself.

Turbidity measurements, carried out in May 2015 upstream and downstream of a very dirty fishnet cage, have revealed high turbidity levels right behind the cage (Chapter 5, page 103). These measurements show that weakly permeable cages create a high turbulence intensity and increase particle dispersion and trapping by the rear circulation cell. Such observations agree, at least qualitatively, with our numerical simulations at large C_{net}.

6.2 Discussion and future works

We are aware of the fact that the various models presented here are based on very strong approximations, so that their interpretation must be done with care. Nevertheless, they provided interesting information and we believe that these models could be used in practice to estimate the hydrodynamic impact of cages.

2D approximation and rigid cage. The most limiting feature of our models is that they are two-dimensional, in a vertical (x, y) plane. They can be thought of as a cut through the mid-plane $z = 0$ of a cage. The width of cage being very extended (about 33 m), we assumed that side effects arising at the end of the flanks (i.e. at $z = \pm 16.5\,m$) have little influence on the main flow. This is obviously very approximate, since secondary flows necessarily exist along the z direction. This effect is particularly significant for very impermeable cages ($C_{net} \to \infty$). Indeed, in this case the flow acceleration below the cage and the pressure decay at the rear end is expected to create a transverse flow as well as three-dimensional vortex tubes with a complex

and unsteady structure. The effect of these flows on particle dispersion and transport is among the perspective of this thesis. Our research group has acquired a strong expertise in the use of the Lattice Boltzmann Method (LBM). This algorithm is particularly efficient for unsteady flows, and can now be used at very large Reynolds numbers when coupled to the Large Eddy Simulation method. It will be used in the near future to account for both the three-dimensional geometry and the unsteadiness of the flow. Deformable cages, whether 2D or 3D, should be also investigated next. Indeed, the dynamics of the net can affect the flow, so that rigid cages like the one considered here might overestimate the flow acceleration. Models of netted structures already exist in the literature, some of which have been listed in the introduction. Here also we believe that the LBM approach, coupled to a solid mechanics algorithm, could offer an interesting opportunity.

The bottom boundary layer below the cage is an important zone were several significant phenomena take place. First of all, our models clearly show that the piezometric pressure decays along this boundary layer, and that the external flow has an algebraic form (Eq. (2.29)). Therefore, any attempt to solve the Prandtl equations at the bottom should take this pressure gradient into account. If this boundary layer is laminar (moderate velocities and/or reduced scale), some solutions for the inner flow might exist, at least far from the inlet $x = x_a$. Indeed, for large $x - x_a$ Eq. (2.29) implies $u_s \sim (x - x_a)^m$ with $m = 1/2$, so that the Falkner-Skan solution might be used, leading to a wall shear stress $\tau_w \sim (x - x_a)^{1/4}$. Numerical simulations, with a moderate flow and under the hypotheses of laminar bottom boundary layer, could help verify this point. If the boundary layer is turbulent, which is probably the case in real cages, the classical law-of-the-wall must be adapted to the presence of the pressure gradient (see for example Spalart & Watmuff (1993) [75]).

A correct modelling of the bottom boundary layer is also necessary to predict the occurrence of erosion below the cage. Indeed, divers often noticed that currents were strong there, and that the bottom was clean below the nets. Also, the Hjulström-Sundborg diagram (Fig. 5.2 page 95) suggests that erosion might occur for the type of particles considered here. The detailed processes of erosion, saltation and resuspension, have not been modelled in this thesis. Instead, particles produced from the sand bed have been injected arbitrarily along a segment slightly above the bottom, and the sand bed has been assumed to remain flat and horizontal. The next

version of the code will include erosion, as well as the deformation of the sand bed.

Our simulations at large C_{net}'s show that some particles can be trapped by the large recirculation cell at the rear of the cage (like the cell BSC in Fig. 6.1 below). In fact, a more detailed analysis would show that only our lightest particles, injected just below the net, are likely to cross the "separatrix streamline" BS under the effect of turbulence, and remain trapped in the cell for some time. This behaviour is sketched in Fig. 6.1. The parameters determining whether the particle can be trapped or not are the turbulent intensity I (which creates dispersion and causes separatrix crossing), the particle response time τ_p (which measures particle's inertia) and the free-fall velocity V_T (which measures the relevance of gravity). To the best of our knowledge, no analytical criterion involving these parameters have been proposed so far, when the cause of separatrix crossing is a random walk model of turbulence. In the near future, we will study this problem with the asymptotic methods developed in Verjus & Angilella (2016) [82] and Angilella [5]. These should provide the required criterion, at least in the limit of weak turbulence intensity.

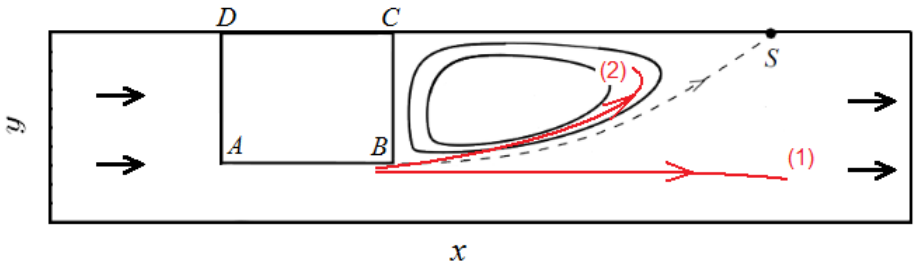

Figure 6.1: *Sketch of typical behaviours of particles behind a cage $ABCD$, near the separatrix streamline BS. (1): a particle is driven away from the recirculation cell BSC, under the combined effect of its inertia and gravity, in spite of turbulence. (2): a light particle crosses the separatrix under the effect of turbulence, in spite of its inertia and of gravity.*

Additional flow and turbidity measurements will be done in the near future, especially to study the transport of effluents. Indeed, waste models have been quickly developed (Cromey et al. (2002) [23], Stigebrendt et al. (2004) [76]) from earlier analyses (Gowen et al. (1989) [40], Hevia et al. (1996) [46], Pérez et al. [67]). However, these numerical tools have not been widely used so far, because they are cost effective and have been built for specific geographical areas (Riera et al. (2017) [72]). They are parameterized with experimental data to suit environments

and fish species from particular regions. To deal with this, we would like to link the results achieved in this thesis (analytic, numeric and field results) with more accurate data related to waste properties (e.g. species-specific food and faeces settling velocities, percentage of uneaten food) and environmental conditions (e.g. macro-algae biofouling, amount of fishes and their size, fishes' location regarding water depth, etc.). To obtain these data, a four-step analysis will be carried out. (i) First, sediment traps will be deployed underneath the cages and uneaten feed and pellets will be analysed in terms of quantity and settling properties. (ii) Then, passive integrated transponder (PIT) tags will be used to assess fishes movements as well as their location in the cage (number vs. depth). (iii) The size of fishes will then be taken into account and (iv) macro-algae biofouling will be quantified as a function of species and development. In addition, seaweeds fouling will be monitored to characterize (e.g. species successions) and quantify (e.g. biomasses, productivity) seaweeds communities, as well as their potential impacts on water recirculation and oxygen depletion inside and outside the cages.

As these parameters evolve in time, current measurements will be carried out (outside, below and inside the cages) to demonstrate the influence of each studied parameters on the drag coefficient and on the settling velocities of particles issued from the cages. These relationships could be later used by modellers wishing to improve their toolboxes and thus actively contribute to an healthy aquaculture development.

Chapter 7

Résumé étendu en français

7.1 Introduction

Les activités humaines en milieu côtier connaissent une expansion continue depuis plusieurs décennies, et cette tendance est appelée à se prolonger dans les années à venir. La *pression anthropique* est ainsi toujours plus importante, et l'impact environnemental d'activités telles que le génie côtier, le transport maritime, les énergies renouvelables ou encore les industries alimentaires, est non-négligeable.

L'aquaculture aussi a un impact sur l'environnement, et cette activité est aussi particulièrement sensible à la qualité de son environnement (voir par exemple Holmer & Kristensen (1994) [48] ; Doglioli et al. (2004) [25] ; Naylor et al. (2005) [64]). Les cages d'aquaculture sont en général installées dans des zones où les courants sont suffisants pour évacuer les effluents (faeces, restes de nourriture, etc.) qui sont en général produits en grande quantité. Le transport de ces matières doit alors être contrôlé non seulement pour limiter la pollution à l'aval des cages, mais aussi pour protéger les cages elles-mêmes. En effet, dans de nombreux cas le panache des effluents a une évolution complexe et difficile à prédire, car il dépend des conditions d'écoulement (lent, rapide ; laminaire, turbulent), de la force des vents, de la qualité de la cage (propre et perméable, encombrée et imperméable), et d'un grand nombre d'autres paramètres.

Un effort important est ainsi nécessaire pour améliorer notre compréhension fine de ces effets complexes. Pour cette raison, en plus des approches expérimentales classiques (mesures de turbidité, courantométrie, études biologiques, etc.), des techniques numériques ont été développées

ces dernières décennies pour mieux comprendre les phénomènes de transport au voisinage des cages d'aquaculture.

Cependant, la plupart des modèles numériques d'écoulements côtiers reposent sur les équations de Saint-Venant, qui fournissent le champ de vitesse horizontale moyennée sur la direction verticale. Cette approche est aussi utilisée dans le contexte de l'aquaculture (voir par exemple Venayagamoorthy (2011) [81]). Même si cette méthode a fait ses preuves pour les interactions à grande échelle entre le courant et la structure, avec un coût de calcul relativement réduit, elle ne donne aucune information sur les mouvements verticaux, l'instationnarité à courte échelle de temps, ou le transport vertical de sédiments et effluents[1]. Ces mécanismes sont cependant cruciaux pour comprendre l'influence des courants sur la structure, ainsi que l'effet de la structure sur les courants et le transport sédimentaire.

Le but de cette thèse est précisément de modéliser ces interactions en détail,* dans le plan vertical*, et de comparer ces résultats, au moins qualitativement, à des mesures de terrain réalisées le long de la colonne d'eau près des cages installées dans la rade de Cherbourg.

Pour atteindre ces objectifs, trois approches complémentaires ont été développées : un modèle analytique des écoulements près d'une structure immergée, un modèle numérique de ce même écoulement, et des mesures courantométriques de terrain. Ces trois approches sont présentées dans les chapitres 2, 3 et 4. Ces chapitres sont suivis d'un chapitre dédié au transport de sédiments (Ch. 5).

7.2 Etude analytique

Le modèle asymptotique développé ici porte sur un domaine bidimensionnel et rectangulaire, dans le plan vertical (Fig. 2.1 page 22). La cage est elle aussi rectangulaire, et est assimilée à un milieu poreux qui exerce sur le fluide une force de freinage proportionnelle au carré de sa vitesse (Eq. (2.4)). Cette force provient de nombreux obstacles à l'intérieur de la cage. Pour simplifier la formulation de cette force, nous avons supposé les obstacles hydrodynamiquement indépendants et uniformément distribués. Le mouvement du fluide sous ces hypothèses est alors décrit par

[1]Pour plus d'informations sur le transport de sédiments voir les Refs. [3][6][4][9][8].

les équations de Reynolds stationnaires (2.6) et (2.7), avec l'équation de continuité (2.8), page 26. La vitesse moyenne du fluide $(\bar{u}, \bar{v})$ est ainsi affectée par les contraintes de pression et de frottement moyennées et les contraintes turbulentes classiques, auxquelles se rajoute l'action de la cage quantifiée par son "coefficient de traînée effectif" C_{net} (Eq. (2.5) page 24). Ce coefficient rend compte non-seulement du coefficient de traînée individuel des obstacles, mais aussi de leur concentration.

Malgré les nombreuses simplifications de ce modèle, les équations de Reynolds restent extrêmement complexes, et leur résolution analytique a nécessité de distinguer deux zones, décrites ci-dessous, où le modèle peut être encore simplifié.

(i) Ecoulement potentiel et quasi-unidirectionnel à l'extérieur des couches limites : dans ces zones l'écoulement moyen est supposé irrotationnel (potentiel), et la turbulence est négligée. On a ainsi posé l'équation (2.17), et l'approximation (2.18). Les termes convectifs de l'équation de Reynolds (i.e. l'accélération du fluide) sont alors grandement simplifiés. Il en résulte que la pression piezométrique ne dépend que de x, et on suppose que le gradient de pression piezométrique est constant (hypothèse additionnelle suggérée par des simulations préliminaires). Le système peut être entièrement résolu et l'écoulement potentiel extérieur est ainsi déterminé dans la cage et sous la cage (Eqs. (2.26) et (2.26) page 30). La chute de pression piézométrique peut aussi être obtenue après quelques calculs. Les champs de vitesse et de pression peuvent alors être écrits en fonction de C_{net}, de la vitesse amont U_∞, et des dimensions de la cage. Les expressions de ces quantités à l'arrière de la cage ont aussi été déterminées (Eqs. (2.32), (2.33) et (2.34) page 31).

(ii) Ecoulement turbulent à l'intérieur de la zone de mélange : le déficit de vitesse dans la cage, et la survitesse sous la cage, créent une zone de mélange turbulente qui prend naissance à la base du filet. En supposant, hypothèse classique, que l'épaisseur de la zone de mélange est faible devant l'échelle des gradients longitudinaux (et la profondeur du filet), nous avons réduit les équations de Reynolds dans cette zone. En examinant l'ordre de grandeur de chaque terme de ces équations, au moyen d'une renormalisation appropriée (Eq. (2.44) page 33), nous avons montré que, si le coefficient de traînée effective C_{net} est modéré (Eq. (2.52)), le champ de vitesse dans la zone de mélange vérifiait l'équation de Prandtl usuelle (2.55). Dans cette zone de mélange, la turbulence est prise en compte via une viscosité turbulente. Enfin,

en raccordant la solution de cette équation (due à Goertler [39]) au champ de vitesse potentiel trouvé en (i), nous avons pu déterminer le profil de vitesse dans toute la colonne d'eau, dans la cage, sous la cage et dans son sillage.

Le modèle théorique ainsi développé donne de premiers ordres de grandeurs très précieux sur le déficit de vitesse dû à l'objet immergé (voir Fig. 2.4 page 39). Il est valide dans la limite des très grands nombres de Reynolds, et peut être utilisé dans le cas de nombres de Reynolds beaucoup plus grands que ceux que l'on peut atteindre avec des méthodes numériques. Il repose cependant sur un grand nombre de simplifications, en particulier une géométrie très simplifiée. Il ne prend pas en compte la couche limite au voisinage de la parois du bas, ni l'agitation de la surface libre.

7.3 Etude numérique

Afin de valider l'approche théorique nous avons effectué des simulations numériques avec le code Fluent. Celui-ci permet un traitement rigoureux des couches limites turbulentes. Nous avons choisi de l'utiliser avec le modèle de turbulence $k-\omega$ SST, conçu pour bien reproduire les phénomènes de décollement. La géométrie est 2D, identique à celle du modèle théorique, et avec les dimensions données par l'équation (3.6) page 48. Il s'agit de dimensions réduites d'un facteur 10 par rapport aux cages réelles, correspondant par exemple à une expérience en canal de laboratoire. Les conditions aux limites du modèle sont décrites en page 49.

Ces simulations correspondent à des nombres de Reynolds de l'ordre de $6.\,10^5$, et ont permis de balayer une large gamme de coefficients de traînée effectifs C_{net}. Pour C_{net} modéré, les résultats théoriques sont retrouvés avec une assez bonne précision (Fig. 3.3 et tableau page 51), les différences étant attribuées au fait que la couche limite du bas n'est pas prise en compte dans la théorie. Lorsque C_{net} devient grand (cages moins passantes car plus encombrées), l'étude numérique montre que la chute de pression n'est plus linéaire (Fig. 3.4 page 52), de sorte que notre théorie ne s'applique plus. Le modèle numérique donne alors des informations importantes concernant le frottement sur le fond dû à la présence de la cage (Fig. 3.6 page 54) et qui pourrait entraîner de l'érosion. L'intensité turbulente est aussi analysée numériquement (Fig. 3.8) pour des cages de perméabilité variable. Ces calculs montrent que la structure de l'écoulement change

drastiquement lorsque C_{net} atteint une certaine valeur, et qu'une cellule de recirculation se forme à l'aval de la cage (Fig. 3.9). Lorsque cette cellule atteint sa longueur définitive (Fig. 3.10), l'écoulement est presque entièrement dévié vers le dessous de la cage, qui peut alors être vue comme un obstacle imperméable. Cela affecte le transport et l'évacuation des effluents, ainsi que la production de particules par érosion sous la cage. La décroissance du débit à travers la cage en fonction de C_{net} correspond au modèle théorique lorsque C_{net} est petit, et suit une décroissance en loi de puissance lorsque C_{net} est grand (Fig. 3.11).

7.4 Mesures de vitesse in-situ

Nous avons effectué des mesures courantométriques au voisinage de cages d'aquaculture situées dans la rade de Cherbourg (Figs. 4.1 et 4.2). Deux ADCP ont été déployés durant environ deux semaines à l'amont et à l'aval d'une cage de 160 m de long et 33 m de large. Des profils de vitesse moyenne, sur 22 niveaux d'altitude, ont ainsi été obtenus sur une profondeur de 11 m. Les conditions météo, la pression atmosphérique, le vent, la température, la pluie et les conditions de marée ont été enregistrées durant la campagne de mesure.

Ces profils de vitesse montrent clairement que la cage ralentit notablement l'écoulement (Fig. 4.23 page 88), et crée un fort courant près du fond. Les profils obtenus sont comparables aux profils théoriques, avec un coefficient de traînée effectif C_{net} d'ordre unité. Cette valeur correspond à un obstacle peu imperméable, c'est-à-dire à une cage très passante, en accord avec le fait que les cages étaient peu remplies et peu affectées par le biofouling durant la campagne de mesures. D'autres champs de vitesse sont disponibles et seront analysés dans une prochaine étude.

7.5 Transport sédimentaire au voisinage des obstacles immergés

Les études ci-dessus montrent que les courants sont perturbés par la présence de la cage, et qu'une survitesse apparaît sous la cage. La structure de l'écoulement peut être grandement modifiée (turbulence, cellule de recirculation), et il est possible que des particules soient remises en suspension sous l'effet de la contrainte de frottement sur le fond. Tous ces effets peuvent affecter le transport de particules (effluents ou sédiments). Afin d'étudier ce point, nous avons réalisé

des simulations en calculant les trajectoires de particules injectées à trois endroits différents (Fig. 5.1 page 93) : des particules déjà en suspension dans l'écoulement amont, des particules produites au bas de la cage (effluents), des particules produites au niveau du lit sableux sous la cage (érosion et remise en suspension). Les diamètres des particules vont de 0,1 mm à 10 mm, et leur densité est de 2,7. L'équation du mouvement de chaque particule est résolue en tenant compte de la traînée et de la flottabilité, dans l'écoulement moyen issu des simulations numériques décrites ci-dessus. La turbulence, qui induit une forte dispersion des trajectoires particulaires, est prise en compte au moyen du modèle stochastique *eddy lifetime model*.

Les résultats de ces simulations montrent clairement que, lorsque C_{net} est assez grand, des particules issues du fond peuvent être transportées vers le haut, à l'arrière de la cage, par les fortes fluctuations turbulentes. En outre, les effluents produits à la base du filet peuvent se retrouver "piégés" dans la zone de recirculation durant un certain temps, au lieu d'être évacués au loin par le courant. Il semble ainsi que la turbidité pourrait être plus élevée à l'aval de la cage, depuis le fond jusqu'à la surface. Ces résultats sont rassemblés dans les figures 5.3, 5.4, 5.5 et 5.6.

Ces résultats ont été comparés à des mesures de turbidité que nous avons réalisées durant une autre campagne de terrain, à l'amont et à l'aval d'une cage peu perméable. Ces mesures ont été réalisées tous les 20 m derrière la cage, et sur trois profondeurs : près de la surface, à mi-profondeur, et près du fond (Fig. 5.7 page 104). Il apparaît clairement que la turbidité est plus élevée à l'aval qu'à l'amont, dans tous les cas de figure. Elle présente aussi de fortes valeurs à l'aval près de la surface. Ces tendances sont clairement en accord qualitatif avec les simulations numériques.

7.6 Conclusion - perspectives

Les trois études analytique, numérique et expérimentale présentées dans ce manuscrit montrent de façon complémentaire divers aspects de l'hydrodynamique de grands objets immergés. En dépit des hypothèses simplificatrices des modèles (écoulement 2D, absence d'agitation, fond plat, cage rectangulaire, etc.) des accords qualitatifs sont observés. Dans tous les cas un écoulement rapide est observé sous la cage, et une zone de mélange apparaît à l'aval de celle-ci. Cette zone de mélange est toujours turbulente. Lorsque la cage est peu passante la structure de l'écoulement

change notablement et une zone de recirculation apparaît dans le sillage. Dans le cas réel, donc tri-dimensionnel, la structure de l'écoulement est plus complexe et des courants transverses (dans la largeur de la cage) vont sans doute apparaître. Des simulations 3D permettront de mieux comprendre l'écoulement et l'effet de ces structures 3D sur le transport sédimentaire.

Les mesures courantométriques, réalisées par ADCP sur toute la colonne d'eau, ont confirmé l'accélération du fluide sous la cage. Elles ne donnent cependant aucune information sur les fluctuations turbulentes. Celles-ci seront réalisées dans un futur proche à l'aide d'un dispositif approprié. De nombreuses autres mesures environnementales sont proposées au chapitre 6 dans les perspectives de cette thèse.

En plus des effets tridimensionnels, les futurs modèles numériques tiendront compte de la déformation et de la dynamique de la cage. L'approche théorique sera elle aussi approfondie, car, même si elle nécessite une géométrie simplifiée, elle permet d'atteindre de très grands nombres de Reynolds. La capture des particules par la cellule de recirculation, et l'intensité turbulente à partir de laquelle la capture peut se produire, seront analysées par les méthodes développées dans les Réfs. [82] et [5].

Bibliography

[1] JV Aarsnes, H Rudi, and G Loland. Engineering for offshore fish farming, 1990.

[2] JV Aarsnes, H Rudi, G Loland, et al. Current forces on cage, net deflection. In *Engineering for offshore fish farming. Proceedings of a conference organised by the Institution of Civil Engineers, Glasgow, UK, 17-18 October 1990.*, pages 137–152. Thomas Telford, 1990.

[3] J.E. Abbott and J.R.D. Francis. Saltation and suspension trajectories of solid grains in a water stream. *Philosophical Transaction of the Royal Society*, 284:225–254, 1977.

[4] J.N. Aldridge. Hydrodynamic model predictions of tidal asymmetry and observed sediment transport paths in Morecambe Bay. *Estuarine, Coastal and Shelf Science*, 44:39–56, 1997.

[5] Jean-Régis Angilella. Noise induced capture of sedimenting particles. *Internal Report*, 2016.

[6] R. A. Bagnold. An approach to the sediment transport problem from general physics. *United State Geological Survey Professional Paper*, 422-1, 1966.

[7] Cheslav Balash, Bruce Colbourne, Neil Bose, and Wayne Raman-Nair. Aquaculture net drag force and added mass. *Aquacultural Engineering*, 41(1):14–21, 2009.

[8] N. Barbry. *Modélisation du transport sédimentaire en milieux côtiers et estuariens selon une approche diphasique.* Thèse de doctorat, Université de Caen, France, 2000.

[9] O. Barndorff-Nielsen and C. Christiansen. Erosion, deposition and grain size distributions of sands. *Proc. R. Soc. Lond.*, 417:335–352, 1988.

[10] Chun-Wei Bi, Yun-Peng Zhao, Guo-Hai Dong, Tiao-Jian Xu, and Fu-Kun Gui. Numerical simulation of interaction between flow and flexible nets. *Journal of Fluids ans structures*, 45:180–201, 2014.

[11] Chun-Wei Bi, Yun-Peng Zhao, Guo-Hai Dong, Tiao-Jian Xu, and Fu-Kun Gui. Numerical simulation of the interaction between flow and flexible nets. *Journal of Fluids and Structures*, 45:180–201, 2014.

[12] Chunwei Bi, Yunpeng Zhao, and Guohai Dong. Development of a coupled fluid-structure model with application to a fishing net in current. In *Hydrodynamics-Concepts and Experiments*. InTech, 2015.

[13] Richard A Braithwaite, Maria C Cadavid Carrascosa, and Lesley A McEvoy. Biofouling of salmon cage netting and the efficacy of a typical copper-based antifoulant. *Aquaculture*, 262(2):219–226, 2007.

[14] S. Candel. *Mécanique des Fluides*. Dunod, 1995.

[15] F Candelier and JR Angilella. Analytical investigation of the combined effect of fluid inertia and unsteadiness on low-re particle centrifugation. *Physical Review E*, 73(4):047301, 2006.

[16] F Candelier, JR Angilella, and M Souhar. On the effect of the boussinesq–basset force on the radial migration of a stokes particle in a vortex. *Physics of Fluids*, 16(5):1765–1776, 2004.

[17] Fabien Candelier, Jean-Regis Angilella, and Mohamed Souhar. On the effect of inertia and history forces on the slow motion of a spherical solid or gaseous inclusion in a solid-body rotation flow. *Journal of Fluid Mechanics*, 545:113–139, 2005.

[18] F. Caton, R.E. Britter, and S. Dalziel. Dispersion mechanisms in a street canyon. *Atmospheric Environment*, 37:693–702, 2003.

[19] B Celikkol, JC DeCew, A Drach, I Tsukrov, and MR Swift. Submersible offshore salmon cage utilizing copper alloy net materials. *Final Report, EcoSea Farming SA, Chile. University of New Hampshire, Durham, NH, USA*, 2010.

[20] P. Chassaing. *Turbulence en mécanique des fluides*. Ed. CEPADUES, 2000.

[21] Nian-Sheng Cheng. Simplified settling velocity formula for sediment particle. *Journal of hydraulic engineering*, 123(2):149–152, 1997.

[22] P. Cheng, S. Gao, and H. Bokuniewicz. Net sediment transport patterns over the Bohai Strait based on grain size trend analysis. *Estuarine, Coastal and Shelf Science*, 60:203–212, 2004.

[23] Chris J Cromey, Thomas D Nickell, and Kenneth D Black. Depomod—modelling the deposition and biological effects of waste solids from marine cage farms. *Aquaculture*, 214(1):211–239, 2002.

[24] J DeCew, I Tsukrov, A Risso, MR Swift, and B Celikkol. Modeling of dynamic behavior of a single-point moored submersible fish cage under currents. *Aquacultural Engineering*, 43(2):38–45, 2010.

[25] A.M Doglioli, M.G Magaldi, L Vezzulli, and S Tucci. Development of a numerical model to study the dispersion of wastes coming from a marine fish farm in the ligurian sea (western mediterranean). *Aquaculture*, 231(1–4):215 – 235, 2004.

[26] Cristian Escauriaza and Fotis Sotiropoulos. Lagrangian model of bed-load transport in turbulent junction flows. *Journal of Fluid Mechanics*, 666:36–76, 2011.

[27] Isla Fitridge, Tim Dempster, Jana Guenther, and Rocky de Nys. The impact and control of biofouling in marine aquaculture: a review. *Biofouling*, 28(7):649–669, 2012.

[28] Arne Fredheim. Current forces on net structure. *Doctoral thesis*, 2005.

[29] ARNE Fredheim and OM Faltinsen. Hydroelastic analysis of a fishing net in steady inflow conditions. In *3rd Int. Conf. Hydroelasticity in Marine Technol*, 2003.

[30] David W Fredriksson. *Open ocean fish cage and mooring system dynamics*. 2001.

[31] David W Fredriksson, Judson C DeCew, and Igor Tsukrov. Development of structural modeling techniques for evaluating hdpe plastic net pens used in marine aquaculture. *Ocean Engineering*, 34(16):2124–2137, 2007.

[32] Aleksandr L'vovich Fridman, PJG Carrothers, et al. *Calculations for fishing gear designs*. Fishing news books England, 1986.

[33] Lars C Gansel, Thomas A McClimans, and Dag Myrhaug. The effects of fish cages on ambient currents. In *ASME 2008 27th International Conference on Offshore Mechanics and Arctic Engineering*, pages 537–543. American Society of Mechanical Engineers, 2008.

[34] Lars C Gansel, Thomas A McClimans, and Dag Myrhaug. Average flow inside and around fish cages with and without fouling in a uniform flow. *Journal of Offshore Mechanics and Arctic Engineering*, 134(4):041201, 2012.

[35] Lars C Gansel, Thomas A McClimans, and Dag Myrhaug. Flow around the free bottom of fish cages in a uniform flow with and without fouling. *Journal of Offshore Mechanics and Arctic Engineering*, 134(1):011501, 2012.

[36] Lars C Gansel, Siri Rackebrandt, Frode Oppedal, and Thomas A McClimans. Flow fields inside stocked fish cages and the near environment. *Journal of Offshore Mechanics and Arctic Engineering*, 136(3):031201, 2014.

[37] Renée Gatignol. The faxén formulas for a rigid particle in an unsteady non-uniform stokes-flow. *Journal de Mécanique théorique et appliquée*, 2(2):143–160, 1983.

[38] WR Geyer, PS Hill, and GC Kineke. The transport, transformation and dispersal of sediment by buoyant coastal flows. *Continental Shelf Research*, 24(7):927–949, 2004.

[39] H. Goertler. Berechnung von aufgaben der freien turbulenz auf grund eines neuun nahegsansantzes. *ZAMM*, 22:244–254, 1942.

[40] RJ Gowen, NB Bradbury, and JR Brown. The use of simple models in assessing two of the interactions between fish farming and the marine environment. 1989.

[41] DI Graham. On the inertia effect in eddy interaction models. *International journal of multiphase flow*, 22(1):177–184, 1996.

[42] DI Graham and PW James. Turbulent dispersion of particles using eddy interaction models. *International Journal of Multiphase Flow*, 22(1):157–175, 1996.

[43] O.S. Hopperstad H. Moe, A. Fredheim. Structural analysis of aquaculture net cages in current. *Journal of fluids and structures*, 26(3):503–516, 2013.

[44] Astrid Harendza, Jan Visscher, Lars Gansel, and Bjornar Pettersen. Piv on inclined cylinder shaped fish cages in a current and the resulting flow field. In *ASME 2008 27th International Conference on Offshore Mechanics and Arctic Engineering*, pages 555–563. American Society of Mechanical Engineers, 2008.

[45] Charles E Helsley and Jang W Kim. Mixing downstream of a submerged fish cage: a numerical study. *IEEE Journal of Oceanic Engineering*, 30(1):12–19, 2005.

[46] M Hevia, H Rosenthal, and RJ Gowen. Modelling benthic deposition under fish cages. *Journal of Applied Ichthyology*, 12(2):71–74, 1996.

[47] Filip Hjulstrom. Studies of the morphological activity of rivers as illustrated by the river fyris, bulletin. *Geological Institute Upsalsa*, 25:221–527, 1935.

[48] Marianne Holmer and Erik Kristensen. Organic matter mineralization in an organic-rich sediment: Experimental stimulation of sulfate reduction by fish food pellets. {*FEMS*} *Microbiology Ecology*, 14(1):33 – 44, 1994.

[49] LY Huang, ZL Liang, WH Song, FF Zhao, and LX Zhu. Experimental study on effect of reducing current velocity by square net cage structure. *Journal of Fishery Sciences of China*, 14(5):860–863, 2007.

[50] John E Huguenin. The design, operations and economics of cage culture systems. *Aquacultural Engineering*, 16(3):167–203, 1997.

[51] John Edward Huguenin and Frank J Ansuini. A review of the technology and economics of marine fish cage systems. *Aquaculture*, 15(2):151–170, 1978.

[52] David Johansson, Jon-Erik Juell, Frode Oppedal, Jan-Erik Stiansen, and Kari Ruohonen. The influence of the pycnocline and cage resistance on current flow, oxygen flux and swimming behaviour of atlantic salmon (salmo salar l.) in production cages. *Aquaculture*, 265(1):271–287, 2007.

[53] M. Kempf, M. Merceron, G. Cadour, H. Jeanneret, Y. Mear, and P. Miramand. Environmental Impact of a Samlmonid farm on a well flushed marine site: II. Biosedimentology. *Journal of Applied Ichthyology*, 18:51–60, 2002.

[54] Pascal Klebert, Pål Lader, Lars Gansel, and Frode Oppedal. Hydrodynamic interactions on net panel and aquaculture fish cages: A review. *Ocean Engineering*, 58:260–274, 2013.

[55] Pascal Klebert, Pål Lader, Lars Gansel, and Frode Oppedal. Hydrodynamic interactions on net panel and aquaculture fish cages: A review. *Ocean Engineering*, 58:260–274, 2013.

[56] Pål F Lader, Birger Enerhaug, Arne Fredheim, and Jørgen Krokstad. Modelling of 3d net structures exposed to waves and current. In *3rd International Conference on Hydroelasticity in Marine Technology*, pages 19–26. Department of Engineering Science, The University of Oxford Oxford, UK, 2003.

[57] Pål Furset Lader and Birger Enerhaug. Experimental investigation of forces and geometry of a net cage in uniform flow. *Oceanic Engineering, IEEE Journal of*, 30(1):79–84, 2005.

[58] Yu-Cheng Li, Yun-Peng Zhao, Fu-Kun Gui, and Bin Teng. Numerical simulation of the hydrodynamic behaviour of submerged plane nets in current. *Ocean Engineering*, 33(17):2352–2368, 2006.

[59] Geir Loland. *Current forces on and flow through fish farms*. Division of Marine Hydrodynamics, the Norwegian Institute of Technology, 1991.

[60] Geir Løland. Current forces on, and water flow through and around, floating fish farms. *Aquaculture International*, 1(1):72–89, 1993.

[61] Jacques Magnaudet. The forces acting on bubbles and rigid particles. In *ASME Fluids Engineering Division Summer Meeting, FEDSM*, volume 97, pages 22–26, 1997.

[62] Martin R Maxey and James J Riley. Equation of motion for a small rigid sphere in a nonuniform flow. *The Physics of Fluids*, 26(4):883–889, 1983.

[63] M. Merceron, M. Kempf, D. Bentley, J.-D. Gaffet, J. Le Grand, and L. Lamort-Datin. Environmental impact of a salmonid farm on the environment on a well flushed marine site: I. Current and water quality. *Journal of Applied Ichthyology*, 18:40–50, 2002.

[64] Rosamond Naylor and Marshall Burke. Aquaculture and ocean resources: raising tigers of the sea. *Annual Review of Environment and Resources*, 30, 2005.

[65] Øystein Patursson, M Robinson Swift, Igor Tsukrov, Knud Simonsen, Kenneth Baldwin, David W Fredriksson, and Barbaros Celikkol. Development of a porous media model with application to flow through and around a net panel. *Ocean Engineering*, 37(2):314–324, 2010.

[66] TH Pearson, KD Black, et al. The environmental impacts of marine fish cage culture. *Environmental impacts of aquaculture*, pages 1–31, 2000.

[67] OM Pérez, TC Telfer, MCM Beveridge, and LG Ross. Geographical information systems (gis) as a simple tool to aid modelling of particulate waste distribution at marine fish cage sites. *Estuarine, Coastal and Shelf Science*, 54(4):761–768, 2002.

[68] Thundathil Velayudhan Ramakrishna Pillay. *Aquaculture and the Environment*. John Wiley & Sons, 2008.

[69] Emmanuel Poizot. Post-processing for ADCP signals recorded near fish cages in October 2016. *Internal Note, Intechmer*, 2016.

[70] Emmanuel Poizot, Romuald Verjus, Hai Yen N'Guyen, Jean-Régis Angilella, and Yann Méar. Self-contamination of aquaculture cages in shallow water. *Environmental Fluid Mechanics*, pages 1–13, 2016.

[71] Madison R Powell. Resistance of copper-nickel expanded metal to fouling and corrosion in mariculture operations. *The Progressive Fish-Culturist*, 38(1):58–59, 1976.

[72] Rodrigo Riera, Óscar Pérez, Chris Cromey, Myriam Rodríguez, Eva Ramos, Omar Álvarez, Julián Domínguez, Óscar Monterroso, Fernando Tuya, et al. Macaromod: A tool to model particulate waste dispersion and benthic impact from offshore sea-cage aquaculture in the macaronesian region. *Ecological Modelling*, 361(C):122–134, 2017.

[73] Francisca Samsing, David Solstorm, Frode Oppedal, Frida Solstorm, and Tim Dempster. Gone with the flow: current velocities mediate parasitic infestation of an aquatic host. *International journal for parasitology*, 45(8):559–565, 2015.

[74] J-S Shuen, L-D Chen, and GM Faeth. Evaluation of a stochastic model of particle dispersion in a turbulent round jet. *AIChE Journal*, 29(1):167–170, 1983.

[75] Philippe R Spalart and Jonathan H Watmuff. Experimental and numerical study of a turbulent boundary layer with pressure gradients. *Journal of Fluid Mechanics*, 249:337–371, 1993.

[76] Anders Stigebrandt, Jan Aure, Arne Ervik, and Pia Kupka Hansen. Regulating the local environmental impact of intensive marine fish farming: Iii. a model for estimation of the holding capacity in the modelling–ongrowing fish farm–monitoring system. *Aquaculture*, 234(1):239–261, 2004.

[77] Åke Sundborg. The river klaralven: a study of fluvial processes. *Geografiska Annaler*, 38(3):238–316, 1956.

[78] M Robinson Swift, David W Fredriksson, Alexander Unrein, Brett Fullerton, Oystein Patursson, and Kenneth Baldwin. Drag force acting on biofouled net panels. *Aquacultural engineering*, 35(3):292–299, 2006.

[79] Igor Tsukrov, Andrew Drach, Judson DeCew, M Robinson Swift, and Barbaros Celikkol. Characterization of geometry and normal drag coefficients of copper nets. *Ocean Engineering*, 38(17):1979–1988, 2011.

[80] Igor Tsukrov, Oleg Eroshkin, David Fredriksson, M Robinson Swift, and Barbaros Celikkol. Finite element modeling of net panels using a consistent net element. *Ocean Engineering*, 30(2):251–270, 2003.

[81] Subhas K Venayagamoorthy, Hyeyun Ku, Oliver B Fringer, Alice Chiu, Rosamond L Naylor, and Jeffrey R Koseff. Numerical modeling of aquaculture dissolved waste transport in a coastal embayment. *Environmental fluid mechanics*, 11(4):329–352, 2011.

[82] Romuald Verjus and Jean-Régis Angilella. Critical stokes number for the capture of inertial particles by recirculation cells in two-dimensional quasisteady flows. *Physical Review E*, 93(5):053116, 2016.

[83] Henk Kaarle Versteeg and Weeratunge Malalasekera. *An introduction to computational fluid dynamics: the finite volume method*. Pearson Education, 2007.

[84] B Vincent and D Marichal. Computation of the flow field in the codend. In *Fishing Technology and Fish Behaviour Working Group Meeting*, 1996.

[85] D.A Yoder, J.R. DeBonis, and N.J. Georgiadis. Modeling of turbulent free shear flows. *NASA/TM*, 2013.

[86] JM Zhan, XP Jia, YS Li, MG Sun, GX Guo, and YZ Hu. Analytical and experimental investigation of drag on nets of fish cages. *Aquacultural engineering*, 35(1):91–101, 2006.

[87] Yun-Peng Zhao, Chun-Wei Bi, Guo-Hai Dong, Fu-Kun Gui, Yong Cui, and Tiao-Jian Xu. Numerical simulation of the flow field inside and around gravity cages. *Aquacultural engineering*, 52:1–13, 2013.

[88] Yun-Peng Zhao, Chun-Wei Bi, Guo-Hai Donga, Fu-Kun Gui, Yong Cui, Chang-Tao Gua, and Tiao-Jian Xu. Numerical simulation of the flow around fishing plane nets using the porous media model. *Journal of Fluids ans structures*, 62:25–37, 2013.

Modélisation des écoulements et du transport de sédiments au voisinage de structures immergées : application aux cages d'aquaculture.

Thi Hai Yen Nguyen

Résumé. Les travaux présentés dans ce manuscrit portent sur les courants et le transport de matière solide en suspension, au voisinage de grandes structures immergées en eau peu profonde. Nous avons focalisé notre étude sur le cas de cages d'aquaculture installées dans la rade de Cherbourg. Situées dans une zone de fort courant, elles impactent leur environnement en modifiant l'écoulement et la turbidité locale. En dépit de nombreuses études déjà disponibles sur l'impact hydrodynamique de tels obstacles, de nombreuses questions se posent encore concernant l'écoulement sous la cage, la production de turbulence, l'érosion du sol et la remise en suspension de sédiments, ainsi que le devenir des déchets produits par la cage. Nous avons choisi de développer trois approches complémentaires pour apporter des éléments de réponse à ces questions. La thèse débute par une étude purement théorique de l'hydrodynamique au voisinage d'un obstacle immergé, assimilé à un milieu poreux, et dans une géométrie simplifiée. Ce modèle bi-dimensionnel, dans le plan vertical, donne de premiers ordres de grandeurs concernant la chute de pression motrice le long du courant, l'accélération du fluide sous la cage, la production de turbulence. Cette étude est suivie d'une analyse numérique de ce même modèle, dans laquelle certaines approximations seront levées. En particulier, le modèle numérique permet de considérer des cages plus imperméables que celles analysées par le modèle théorique. Il est cependant limité en nombre de Reynolds, et a été appliqué avec des échelles réduites. Ce modèle numérique a permis d'analyser le lien direct entre le coefficient de traînée effectif de la cage et diverses quantités-clés : le débit à travers la cage, la chute de pression le long du courant, la production de turbulence et l'apparition d'une zone de recirculation à l'arrière de l'obstacle. Ce dernier effet, visible seulement pour des cages très imperméables, a un impact notable sur le transport de sédiments et d'effluents : lorsque l'arrière de la cage devient une zone morte (zone de recirculation), l'essentiel du débit passe au dessous, ce qui crée de fortes survitesses et produit de la turbulence. Celle-ci peut alors entraîner des particules indésirables dans la zone morte, ce qui augmente notablement la complexité de leurs trajectoires et retarde leur évacuation. Enfin, ces études théoriques ont été complétées par des mesures vélocimétriques et turbidimétriques à l'amont et à l'aval d'une grande cage installée dans la rade de Cherbourg. Celles-ci confirment la présence d'une survitesse en provenance du dessous de la cage, comparable à celle prédite par le modèle théorique. Dans le cas d'une cage très peu perméable, la persistence d'une forte turbidité a été mesurée à l'aval de celle-ci, en accord qualitatif avec les simulations numériques.

Abstract. This manuscript presents investigations of current and sediment transport in the vicinity of large immersed structures in shallow water flows. It focuses on aquaculture cages installed in the roadstead of Cherbourg. Being located in a high stream zone, these obstacles have a non-negligible effect on currents as well as turbidity. In spite of numerous references on this topic, many questions still arise concerning the environmental impact of such objects. Quantitative information are still needed about the flow below the cage, turbulence production, erosion of the sand bed, sediments resuspension, and evacuation of effluents. To deal with these open questions, we have chosen to develop three complementary approaches. The thesis starts with an analytical study of the flow in a simplified two-dimensional model containing a large rectangular porous structure. Only the motion in the vertical mid-plane of the obstacle is considered. This preliminary model provides estimations of various dynamic quantities, like the velocity increase below the cage, the decay of piezometric pressure along the stream, and turbulence production. Then follows a numerical analysis of the very same flow, based on less stringent approximations. Because of the high cost of computations, simulations have been done at a reduced scale. Nevertheless, they confirm most of the findings of the analytical approach for very permeable cages, and provide crucial information also about weakly permeable cages which were out of reach of the analytical model. In particular, the formation of a recirculation cell behind such cages, together with turbulence production, have been studied with the numerical model. This effect has been observed to affect sediment and effluent transport: when the flow at the rear of the cage takes the form of a cell with closed streamlines, the cage can be thought of as closed and most of the flow passes below. This creates large velocity gradients and produces turbulence which significantly increases the dispersion of sediments and effluents. These particles are then likely to be captured for some time in the cell, instead of being evacuated away. In addition to these theoretical approaches, in-situ current and turbidity measurements have been performed upstream and downstream of a large cage immersed in the roadstead of Cherbourg. They confirm the existence of a fast stream emerging from below the cage. Vertical streamwise velocity profiles have been shown to agree with theoretical ones, in the case of a very permeable cage. Also, large turbidity levels have been recorded at the rear of a weakly permeable cage, in qualitative agreement with simulations.